Controlling non-equilibrium dynamics in lattice gas models

Ruslan Ilyich Mukhamadiarov

Dissertation submitted to the Faculty of the

Virginia Polytechnic Institute and State University

in partial fulfillment of the requirements for the degree of

Doctor of Philosophy

in

Physics

Uwe C. Täuber, Chair

Michel Pleimling

Edwin Barnes

Shengfeng Cheng

February 24, 2021

Blacksburg, Virginia

Keywords: Non-equilibrium systems, Lattice gases, Scale-invariant dynamics, Control

Controlling non-equilibrium dynamics in lattice gas models

Ruslan Ilyich Mukhamadiarov

(ABSTRACT)

In recent years a new interesting research avenue has emerged in non-equilibrium statistical physics, namely studies of collective responses in spatially inhomogeneous systems. Whereas substantial progress has been made in understanding the origins and the often universal nature of cooperative behavior in systems far from equilibrium, it is still unclear whether it is possible to control their global collective stochastic dynamics through local manipulations. Therefore, a comprehensive characterization of spatially inhomogeneous non-equilibrium systems is required.

In the first system, we explore a variant of the Katz–Lebowitz–Spohn (KLS) driven lattice gas in two dimensions, where the lattice is split into two regions that are coupled to heat baths with distinct temperatures $T > T_c$ and T_c respectively, where T_c indicates the critical temperature for phase ordering. The geometry was arranged such that the temperature boundaries are oriented perpendicular or parallel to the external particle drive and resulting net current. For perpendicular orientation of the temperature boundaries, in the hotter region, the system behaves like the (totally) asymmetric exclusion processes (TASEP), and experiences particle blockage in front of the interface to the critical region. This blockage is induced by extended particle clusters, growing logarithmically with system size, in the critical region. We observe the density profiles in both high- and low-temperature subsystems to be similar to the well-characterized coexistence and maximal-current phases in (T)ASEP models with open boundary conditions, which are respectively governed by hyperbolic and trigonometric tangent functions. Yet if the lower temperature is set to T_c, we detect marked

fluctuation corrections to the mean-field density profiles, e.g., the corresponding critical KLS power-law density decay near the interfaces into the cooler region.

For parallel orientation of the temperature boundaries, we have explored the changes in the dynamical behavior of the hybrid KLS model that are induced by our choice of the hopping rates across the temperature boundaries. If these hopping rates at the interfaces satisfy particle-hole symmetry, the current difference across them generates a vector flow diagram akin to an infinite flat vortex sheet. We have studied the finite-size scaling of the particle density fluctuations in both temperature regions, and observed that it is controlled by the respective temperature values. If the colder subsystem is maintained at the KLS critical temperature, while the hotter subsystem's temperature is set much higher, the interface current greatly suppresses particle exchange between the two regions. As a result of the ensuing effective subsystem decoupling, strong fluctuations persist in the critical region, whence the particle density fluctuations scale with the KLS critical exponents. However, if both temperatures are set well above the critical temperature, the particle density fluctuations scale according to the totally asymmetric exclusion process. We have also measured the entropy production rate in both subsystems; it displays intriguing algebraic decay in the critical region, while it saturates quickly at a small but non-zero level in the hotter region.

The second system is a lattice gas that simulates the spread of COVID-19 epidemics using the paradigmatic stochastic Susceptible-Infectious-Recovered (SIR) model. In our effort to control the spread of the infection of a lattice, we robustly find that the intensity and spatial spread on the epidemic recurrence wave can be limited to a manageable extent provided release of these restrictions is delayed sufficiently (for a duration of at least thrice the time until the peak of the unmitigated outbreak).

Controlling non-equilibrium dynamics in lattice gas models

Ruslan Ilyich Mukhamadiarov

(GENERAL AUDIENCE ABSTRACT)

In recent years a new interesting research avenue has emerged in far-from-equilibrium statistical physics, namely studies of collective behavior in spatially non-uniform systems. Whereas substantial progress has been made in understanding the origins and the often universal nature of cooperative behavior in systems far from equilibrium, it is still unclear whether it is possible to control their global collective and randomly determined dynamics through local manipulations. Therefore, a comprehensive characterization of spatially non-uniform systems out of equilibrium is required.

In the first system, we explore a variant of the two-dimensional lattice gas with completely biased diffusion in one direction and attractive particle interactions. By lattice gas we mean a lattice filled with particles that can hop on nearest-neighbor empty sites. The system we are considering is a lattice that is split into two regions, which in turn are maintained at distinct temperatures $T > T_c$ and T_c, respectively, with T_c indicating the critical temperature for the second-order phase transition. The geometry of the lattice was arranged such that the temperature boundaries are oriented perpendicular or parallel to the external particle drive that is responsible for a completely biased diffusion. When the temperature boundaries are oriented perpendicular to the drive, in the hotter region with temperature $T > T_c$, the system evolves as if there are no attractive interactions between the particles, and experiences particle blockage in front of the temperature boundary from the hotter region held at $T > T_c$ to the critical region held at T_c. This accumulation of particles at the temperature boundary is induced by elongated collections of particle, i.e., particle clusters

in the critical region. We observe the particle density profiles ($\rho(x)$ vs x plots) in both high-and low-temperature subsystems to be similar to the density profiles found for other well-characterized (T)ASEP models with open boundary conditions, which are in the co-existence and maximal-current phases, and which are respectively governed by hyperbolic and trigonometric tangent functions. Yet if the lower temperature is set to T_c, we detect marked corrections to the hyperbolic and trigonometric tangent-like density profiles due to fluctuations, e.g., we observe the algebraic power-law decay of the density near the interfaces into the cooler region with the critical KLS exponent.

For a parallel orientation of the temperature boundaries, we have explored the changes in the particle dynamics of the two-temperature KLS model that are induced by our choice of the particle hopping rates across the temperature boundaries. If these particle hopping rates at the temperature interfaces satisfy particle-hole symmetry (i.e. remain unchanged when particles are replaced with holes and vice versa), the particle current difference across them generates a current vector flow diagram akin to an infinite flat vortex sheet. We have studied how the particle density fluctuations in both temperature regions scale with the system size, and observed that the scaling is controlled by the respective temperature values. If the colder subsystem is maintained at the KLS critical temperature $T_{cold} = T_c$, while the hotter subsystem's temperature is set much higher $T_{hot} \gg T_c$, the particle currents at the interface greatly suppresses particle exchange between the two temperature regions. As a result of the ensuing effective subsystem separation from each other, strong fluctuations persist in the critical region, whence the particle density fluctuations scale with the KLS critical exponents. However, if both temperatures are set well above the critical temperature, the particle density fluctuations scale with different scaling exponents, that fall into the totally asymmetric exclusion process (TASEP) universality class. We have also measured the rate of the entropy production in both subsystems; it displays intriguing algebraic decay in the critical region, while it reaches quickly a small but non-zero value in the hotter region.

The second system is a lattice filled with particles of different types that hop around the lattice and are subjected to different sorts of reactions. That process simulates the spread of the COVID-19 epidemic using the paradigmatic random-process-based Susceptible-Infectious-Recovered (SIR) model. In our effort to control the spread of the infection of a lattice, we robustly find that the intensity and spatial spread of the epidemic second wave can be limited to a manageable extent provided release of these restrictions is delayed sufficiently (for a duration of at least thrice the time until the peak of the unmitigated outbreak).

Dedication

To my Mother and Father.

Acknowledgments

I would like to thank my advisor Professor Uwe Täuber for all his time that he spent on me. Professor Uwe Täuber's impact on my development as a researcher is immense and what I am today is largely because of his guidance. I greatly valued my time as his student and I hope we will continue to collaborate in the future.

I would also like to thank Professor Michel Pleimling for his outstanding critique during our joint research group meetings which helped me to shape the results of my main PhD project.

I also want to thank Professor Edwin Barnes for finding time in his schedule to talk to me and answer all sorts of questions that a young researcher could have.

Finally, I would like to thank Professor Shengfeng Cheng who in addition of being an excellent teacher, was serving on my PhD committee and helping me to progress in my PhD program.

Contents

List of Figures

List of Tables

Chapter 1

Introduction

Physical systems with a large number of degrees of freedom can be characterized by a set of macroscopic variables that in turn can in principle be obtained from the microscopic system parameters. If the system is in its equilibrium stationary state, well-known straightforward procedures can be employed to relate these two sets of variables. The equilibrium condition implies that the system has to be isolated or coupled to some heat or particle reservoir, as that would ensure that the average values of the macroscopic parameters that describe the physical system would stay unchanged in the long-time limit. However, if the system is driven away from its equilibrium stationary state by a perturbation that modifies one or several of the macroscopic variables, then in a process of relaxation to a new equilibrium or stationary state the system will be essentially out of equilibrium. Moreover, in some situations physical systems can be genuinely out of equilibrium, for instance, if they are coupled to external reservoirs that act as sources or sinks, i.e. if net fluxes of energy or matter are present in the system.

While non-equilibrium systems are quite ubiquitous and are regularly encountered in physics, chemistry, biology, engineering, etc., to this day there is still no general prescription of how to obtain the macroscopic variables that would characterize the dynamical behavior of various non-equilibrium systems. Not only is there no direct way to relate the microscopic Hamiltonian of the system to the stationary probability distribution for non-equilibrium systems, but that also will not be sufficient; the presence of non-zero fluxes in non-equilibrium systems

renders inapplicable the thermodynamic ensemble description which is based solely on the stationary probability distribution for distinct configurations. Instead, to completely characterize the steady state of the non-equilibrium system the knowledge of both the stationary probability distribution and the probability currents is required [1–3].

In the classical realm, the stationary probabilities and probability currents of a non-equilibrium system can be obtained from the master equation using the theory of stochastic processes. However, in contrast to equilibrium systems where detailed balance imposes a strong constraint on possible values of the transitions rates that enter the master equation, detailed balance does not hold in non-equilibrium systems and therefore the transition rates between different configurations of systems out of equilibrium are generally unconstrained and could have any functional form. Therefore, for non-equilibrium systems one has to know all generally time- and history-dependent transition rates to set up and solve the master equation. In addition to that, the problem of solving the master equation becomes insurmountable as the number of degrees of freedom in the system increases. This is why there are only a very few instances in the literature when the fully microscopic equations of motion for stochastic dynamical systems have been solved exactly, e.g., for diffusion [4], elementary [5] and more complex chemical reactions [6, 7], a closed Ising chain [8], the asymmetric exclusion process [9, 10], etc [11]. The outlined difficulties illustrate why the microscopic description through the master equation might not be suitable for certain non-equilibrium systems.

A phenomenological approach of characterizing both equilibrium and non-equilibrium systems has been developed over the years: it is based on searching for an intermediate mesoscopic description through the identification of local 'coarse-grained' quantities that capture the major features of the system's dynamics [12–14], e.g., a local particle density if one would think about hydrodynamics [15], a local magnetization if one would consider magnetic systems [16], the local velocity for studying a depinning transition [17], etc. The key

to success of a mesoscopic description comes down to the fact that the local coarse-grained variables capture well statistical fluctuations that are common and crucially important for non-equilibrium systems. While in equilibrium statistical mechanics the fluctuations are typically utilized for calculating the response functions via the fluctuation-dissipation theorem, in non-equilibrium systems the spatial and temporal fluctuations may determine the full course of the dynamics. Figuring out when fluctuations play a crucial role in the time evolution of systems far from equilibrium and when they can be safely ignored is a central object of study of non-equilibrium physics.

As it appears, fluctuations may play a substantial role in the scaling limit, a limit when the system's correlation length diverges, giving rise to strongly collective behavior. Remarkably, in the scaling limit microscopically different systems can display *universality*, a phenomenon when the system's dynamics is determined not by its microscopic details such as the type of interparticle interactions, but by the system's basic symmetries, dimension, range of inter-particle interactions, and conservation laws [18–20]. Whereas some non-equilibrium systems can be brought to the scaling limit by varying relevant control parameters, certain non-equilibrium systems that display generic scale invariance can remain in the scaling limit for all values of control parameters [21]. The fact that universal behavior can be observed in wide variety of non-equilibrium systems prompted their categorization into different universality classes.

Assuming it is possible to separate a system's fast and slow degrees of freedom, one can write down a Langevin-type coarse-grained equation of motion upon identifying the coarse-grained order parameter and other conserved quantities that are coupled to that order parameter [12, 22, 23]. Analyzing the resulting Langevin equation using either field-theoretical techniques, mode-coupling theory, or scaling analysis, it is possible to infer the scaling form of the order parameter, correlation functions, and other quantities that play an important role in

characterizing the dynamics of the system [13, 24]. Then, one can see that the scale-free behavior of these quantities is described by a set of scaling exponents that enter the obtained scaling form. If two microscopically distinct systems share the same set of scaling exponents, then it is said that they both fall into the same universality class.

Even with all theoretical tools currently available, the analytical treatment of certain non-equilibrium systems can be very challenging, just as it is challenging to set up a controllable environment for experiments. This is why computer simulations are abundantly used to numerically study the dynamics of non-equilibrium systems, e.g., chemical reactions in a gel, epidemic spreading, driven fluids, growing crystalline surfaces, etc. [25–28]. Not only can computer simulations provide valuable insight on the physics of a non-equilibrium system that could be crucial in constructing a meaningful theory, but they could also test the existing hypotheses by probing power-law scaling from the computer experiments and comparing the results with the scaling exponents that have been predicted analytically. Moreover, with computer simulations at hand it is easy to change a system's relevant parameters and probe the entire parameter space, exploring all existing types of strong collective behavior that a particular non-equilibrium system can display. Phase transitions or crossovers between different types of collective behavior may occur upon variation of the relevant parameters that could drive the system away from one scale-invariant regime to another, i.e., from one renormalization group fixed point to another [24, 29–32]. The search for effective mechanisms that would permit switching between different types of universal behaviors in non-equilibrium systems is currently an active area of research.

Whereas substantial progress has been made in understanding the origins and the universal nature of cooperative behavior in systems far from equilibrium, it is still unclear whether it is possible to control their global collective stochastic dynamics through local manipulation of a finite spatial patch or through finite-time global perturbations. This study focuses on

exploring the possibility of controlling the dynamics of non-equilibrium systems through various changes in the system's control parameters. In Chapter 2 and Chapter 3 we report the results of our careful investigation of a two-temperature version of the Katz-Lebowitz-Spohn (KLS) driven lattice gas, where we locally vary the temperature control parameter by splitting the lattice into two temperature regions, orienting the temperature boundaries either perpendicular (Chapter 2) or parallel (Chapter 3) to the drive. In Chapter 4, we explore how changing the relevant parameters globally for a finite period of time affects the course of the dynamics of a particular reaction-diffusion system modeled on a lattice. Specifically, we have simulated the COVID-19 infection spread on a lattice using the Suspectible-Infection-Recovered (SIR) stochastic model and we have analyzed the effects of control measures that temporarily drive the system below its epidemic threshold.

1.1 Driven lattice gases

The first non-equilibrium model that we focus our attention on is a modified version of the Katz-Lebowitz-Spohn (KLS) driven lattice gas. The following two chapters cover our studies of the two-temperature KLS model for two different choices of the geometry: Chapter 2 considers the case when the lattice is split into two sectors that are maintained at different temperatures with the temperature boundaries being oriented perpendicular to the drive, while in Chapter 3 we report our findings for the case when the temperature boundaries are placed parallel to the drive. Chapter 2 is based on the work [33] published in Physical Review E. Chapter 3 is based on the work [34], published in Journal of Statistical Mechanics: Theory and Experiment.

A lattice gas can be defined as a d-dimensional regular lattice that is populated with particles, which are allowed to hop from cell to cell on a lattice in a random manner. This deceptively

simple Markov process can display rich dynamical behavior as the set of dynamical rules that define the model is modified, e.g. when one adds restrictions on the occupation number, or specifies the type of interparticle interactions, the range of interactions, etc. The simplest realization of a lattice gas with unbiased particle hops can model the Brownian motion of gas molecules. However, if the particle hops on a lattice become biased due to some external drive, which could be a gradient of chemical potential or some externally applied field, and if the system's boundary conditions allow the system to sustain a net current, then such a system will be called a driven lattice gas. A paradigmatic example of a driven lattice gas is the (Totally) Asymmetric Exclusion Process (T)ASEP [35, 36]. In the (T)ASEP, each lattice site is allowed to host only a single particle at any time, i.e., site exclusion is implemented. Biased particle motion along the drive in combination with either periodic or open boundary conditions sets up a non-vanishing particle current in the lattice gas, which drives the system to certain non-equilibrium steady states. As it appears, the (T)ASEP can mimic the dynamics of many driven systems in biology, sociology, and engineering [37]. Moreover, the one-dimensional (T)ASEP chain is an interesting model from a purely theoretical standpoint, as it is one of the very few non-equilibrium systems for which the microscopic master equation has been solved exactly [9, 10, 38, 39].

In this work we study a modified version of the Ising-type driven lattice gas, called the Katz-Lebowitz-Spohn (KLS) model, that was conjectured to describe the dynamics of fast ionic conductors [27, 40, 41]. Similarly to the (T)ASEP, the KLS model consists of a d-dimensional lattice filled with particles that are being driven by some external field, but, in addition to site exclusion, the KLS particles experience attractive interactions that are prescribed by the Ising Hamiltonian, and the whole lattice is coupled to a temperature bath. As in the Ising model, the KLS system experiences a continuous phase transition at the KLS critical temperature. Remarkably, when the KLS temperature is maintained exactly at the

critical value, the KLS dynamics is governed by a set of scaling exponents that belong to the *critical KLS* universality class. At the same time, when the KLS temperature is set above the critical temperature, i.e., when the KLS system is in its disordered phase, its dynamics is governed by a different set of scaling exponents that belong to the (T)ASEP universality class [33, 42, 43].

This last observation motivated us to investigate the possibility of controlling the scale-invariant behavior in the KLS driven lattice gas by changing the temperature as a control parameter: by locally varying the temperature of the lattice, we can in principle set up a competition between two different types of scale-invariant dynamics, namely, between the *critical KLS* and *(T)ASEP* universal behaviors. The simplest geometry choice with which we approach the outlined problem is to split the entire lattice into two sectors that are maintained at different temperatures, with the temperature boundaries being oriented either perpendicular or parallel to the external drive. Then the lattice region where the temperature is maintained at the critical value will be called the *critical* subsystem, and the region with temperature above the critical value will be referred to as the *hotter* subsystem.

In Chapter 2, we show that when the temperature boundaries in the two-temperature KLS driven lattice gas are oriented perpendicular to the drive, the system becomes highly inhomogeneous shortly after the beginning of the simulation. The initial scale-invariant behavior in the hotter temperature region is washed out by phase separation that occurs when two particle density shock waves move towards each other and meet in the center of the hotter subsystem; in the critical subsystem long extended density gradients form that eventually destroy dynamical scaling (with critical KLS exponents). We show in this chapter that such dramatic changes are triggered by a difference in the drive-induced net particle current in the hotter and critical (cooler) subsystems that leads to an accumulation of particles at one of the temperature boundaries. We observe that the density profile shapes in both high-and

low-temperature subsystems are similar to the density profiles observed for the coexistence and maximal-current phases in the one-dimensional (T)ASEP with open boundary conditions. Remarkably, if the cooler subsystem's temperature is set to the critical temperature, the excess density at the temperature boundaries decays as a power law with an exponent that belongs to the critical KLS universality class. This indicates that the critical KLS scale-invariant behavior still persists in the critical subsystem even after it has been coupled to the hotter temperature region.

In Chapter 3, we explore another variant of the two-temperature KLS driven lattice gas where the lattice is again split into two sectors, but in such a way that the temperature boundaries are oriented parallel to the external particle drive. For this choice of geometry, it is necessary to define the rules for particle hops across the temperature boundaries without breaking the system's fundamental symmetries. After we introduce the hopping rates across the temperature interfaces that respect particle-hole symmetry, which is a fundamental symmetry of the KLS model, we run computer simulations and explore the changes in the KLS dynamical behavior that are induced by the coupling of the two subsystems with different temperatures. As in the previous case with perpendicular temperature boundaries, the net particle currents in the hotter and cooler subsystems assume different values; however, instead of a blockage-induced density phase separation, this current difference produces a vector flow diagram akin to a vortex sheet.

In Chapter 3 we demonstrate how this particle current discontinuity at the temperature interfaces affects the scale-invariant behavior of each subsystem. Specifically, we probe the finite-size scaling of the particle density fluctuations and calculate the entropy production rate per volume in both subsystems. These calculations demonstrate that critical KLS fluctuations persist in the two-temperature KLS when the cooler subsystem is maintained exactly at the critical temperature with the hotter temperature being well above the critical

temperature. We have also considered another possible choice of the hopping rates across the temperature interfaces that explicitly breaks particle-hole symmetry. In that situation these hopping rates across the temperature boundaries induce a net particle flux across the subsystems' boundaries that displays a power-law behavior, until ultimately the particle exclusion constraints generate a clogging transition to an inert state.

1.2   Infection spread on a lattice

The global spread of the novel coronavirus, known as SARS-CoV-2, that has started at the beginning of 2020 has caused a major health and economic crisis nearly in every part of the world. While some countries took the matter extremely seriously and halted the infection spread at its early stages, other governments overlooked the gravity of the danger and precipitated countless tragedies that could have been otherwise avoided. Since the coronavirus is a disease that is transmitted upon contact, reducing the number of contacts would be a necessary and sufficient measure to limit the spread of the disease before an effective vaccine is ready. In Chapter 4 we show how the infection spread can be modeled on a regular lattice using the stochastic Susceptible-Infected-Recovered (SIR) model, and how nonpharmaceutical measures such as social distancing could be implemented in this simple model. Chapter 4 is based on Ref. [44], published in Scientific Reports.

In the SIR compartmental model the individuals that constitute the population can be in three different states: *S - Susceptible, I - Infected,* and *R - Recovered* [45, 46]. The disease spread is modeled by two reactions: the infection reaction $S + I \rightarrow I + I$ that occurs with the infection rate r, and the recovery reaction $I \rightarrow R$ that happens with the recovery rate a (inverse recovery period). For this model the basic reproduction number is proportional to the ratio of the infection to the recovery reaction rates $R_0 \propto r/a$.

In principle, a set of deterministic mean-field rate equations can encode two SIR reactions and predict how the total number of individuals in each state evolves with time. However, they do not account for the spatial and temporal fluctuations that drive the continuous phase transition when the system is near the epidemic threshold [24, 47, 48]. Indeed, emerging spatial correlations could significantly modify the route of the disease spread and lead to substantially different estimates. For example, in reaction-diffusion models the system can hit an absorbing state when the fluctuations of some observable reach the value of its mean [24, 29, 49]. Similarly, there could be real-world situations when fluctuations could completely halt the spread of the disease near its onset, if the infectious population will hit zero at any time in the early stage of the disease spread. At the same time, fluctuations can keep the epidemics active by continually rewiring the infection links [47].

As is shown in Chapter 4, after simulating the unmitigated spread of COVID-19 with a stochastic SIR model on a regular two-dimensional lattice, we observe that the infection fronts traverse the entire system and reach every healthy individual eventually when the system is above the epidemic threshold, i.e., the infection spread results in a complete extinction of the susceptible population because of the lattice topology. In contrast, the mean-field rate equations can never predict a complete extinction of all susceptibles since such an outcome is prohibited by their mathematical construction. As a result, the rate equations could substantially underestimate the severity of the health crisis [50, 51]. The outlined arguments compel us to choose a stochastic representation of the SIR model over of the mean-field rate equations. While we have modeled the COVID-19 spread on various spatial architectures, in this work we present the results for a regular two-dimensional lattice.

Since we are ultimately interested in quelling the infection spread, our goal would be to push our stochastic system below its epidemic threshold by varying the relevant control parameters. We achieve that by switching on repulsive Ising interactions for all particles, which

mimics the social-distancing mitigation strategy. With the antiferromagnetic interactions on, particles will avoid having other particles as their neighbors, and as a result the number of contacts and infection reactions will drop and with it the effective reproduction number. In our work we switch on the repulsive interactions between particles after the population of infectious individuals exceeds some prescribed fraction of the total population. After that, we maintain social distancing in our system for some period of time before switching the interparticle interactions off again. As one would expect, if social distancing lasts only for a short period of time (1-2 recovery periods), a strong second wave will inevitably come and nearly all the healthy population will become infected as in the unmitigated case. However, if social distancing is maintained for quite a long period of time (more than 10 recovery periods), the major fraction of the infection centers will die out and, as a result, the infection spread will be significantly reduced and localized.

Chapter 2

Transverse Temperature Interfaces in the KLS Driven Lattice Gas

The following chapter was adapted with minor modifications, with permission from Physical Review E, from our publication:

*R. I. Mukhamadiarov, Priyanka, and Uwe C. Täuber. Transverse temperature interfaces in the Katz-Lebowitz-Spohn driven lattice gas. Physical Review E **100**, 062122 (2019).*

My main scientific contributions to this publication were developing the simulation code for the two-temperature Katz-Lebowitz-Spohn driven lattice gas, and performing an extensive analysis of the data that I obtained from running simulations. Also, I wrote the first draft of the manuscript and made all figures.

2.1   Introduction

The absence of a unified theoretical framework for non-equilibrium systems has instigated the development of a variety of simple models that capture certain decisive features of non-equilibrium processes. Driven lattice gases represent a class of paradigmatic interacting particle systems that has attracted considerable attention over the past decades [27, 42, 52, 53]. These driven lattice gas models are characterized by non-trivial stationary states that

display generic scale invariance [21, 24, 54, 55], implying that their dynamics is governed (asymptotically) by power laws and genuine non-equilibrium scaling exponents. Prototypical examples are the asymmetric and totally asymmetric exclusion processes (T)ASEP with hard-core particles and (fully) biased hopping transport [10, 35, 36, 56, 57]. Adding attractive nearest-neighbor Ising interactions as in the Katz–Lebowitz–Spohn (KLS) model moreover induces a continuous phase transition at a critical temperature T_c separating disordered configurations from a low-temperature regime showing phase segregation in the form of ordered particle (or hole) stripes oriented parallel to the drive [27, 40, 41, 53].

The (T)ASEP model and KLS system in the disordered high-temperature phase are governed by identical scaling exponents [42, 58]. However, the KLS dynamical scaling properties change when the temperature approaches the critical value T_c: In this critical region, the dynamics is impeded significantly by the diverging correlation length of the order parameter fluctuations, i.e., critical slowing-down. Consequently, the asymptotic non-equilibrium scaling exponents assume critical values that are distinct from those that capture generic dynamical scale invariance at elevated temperatures.

Both in its high-temperature phase and at the non-equilibrium critical point, the KLS model thus displays dynamic scale invariance. Hence it is interesting to ask if a spatially inhomogeneous system with different regions held at different temperatures $T_h > T_c$ and $T_l = T_c$, respectively, remains scale-invariant. Moreover, one may ask how its properties compare to those of the standard homogeneous KLS system at uniform temperature. To our knowledge, the effect of combining two KLS driven lattice gases held at distinct temperatures has not yet been explored in the literature. In this present work, we set one part of the system at high temperature $T_h > T_c$, whereas the other part is (usually) held at the critical point T_c, with the temperature boundaries oriented transverse to the drive.

The effects of similar temperature heterogeneities were earlier explored in detailed studies

of an Ising ring (without external drive) [59] and two-dimensional square lattice [60]. Other two-temperature lattice gas models were introduced by associating different temperatures T_x, T_y with different hop directions x, y [61], or by coupling the $i+j =$ even / odd sublattices to different temperature reservoirs [62]. The key difference between the KLS driven lattice gas and previously studied models resides in the way detailed balance is violated. In the two-temperature non-driven Ising models, the second thermal reservoir induces a net heat flux that forces the system out of equilibrium. In contrast, the externally imposed hopping bias or drive in the KLS system generates a global net particle current, and consequently a quite distinct non-equilibrium steady state. Moreover, the drive induces a strong anisotropy that causes correlations to scale differently in directions parallel and transverse to the drive, with associated distinct correlation lengths $\xi_\parallel \sim \xi_\perp^{1+\Delta}$ with an anisotropy exponent Δ, which in turn leads to spatially anisotropic scaling laws.

Our two-temperature generalization of the driven KLS lattice gas can be considered as two subsystems on a two-dimensional torus coupled to each other through particle exchange across the two interfaces. Other interacting KLS subsystems have been investigated, such as a multi-layered KLS model with particle-hole exchange between layers first excluding Ising interactions between layers [63], and subsequently accounting for exchange energetics [64]. In the latter case, the presence of inter-layer interactions produces intriguing spatial patterns termed "fingers" or "icicles". Multiple-species KLS variants in two dimensions were, e.g., analyzed in Refs. [65, 66], where a set of microscopic dynamical rules for two distinct particle species A and B were imposed that resulted in ordering perpendicular to the drive. For a more comprehensive list of KLS model variations we refer to the overview [53].

In the stationary state, the two-temperature KLS model displays phase separation into low- and high-density regions in the hotter region, with the separating domain wall located in the middle of the hot subsystem and oriented perpendicular to the drive. The high-density

phase is formed at the hot-into-critical temperature interface; it is caused by a blockage of particle flow into the critical subsystem, which is impeded by the emerging extended critical clusters. This in turn generates an algebraic density decay inside the critical region near the boundaries to the hotter subsystem. The density profiles of the two subsystems in the two-temperature KLS resemble the standard hyperbolic and trigonometric tangent functions that are characteristic signatures of the coexistence and maximal-current phases in (T)ASEP systems with open boundaries. This similarity allows us to analyze the stationary-state properties of the two-temperature KLS model explicitly. Employing numerical simulations and mean-field calculations for the open TASEP coupled to particle reservoirs, we find that the uniform steady-state current is set by the impeded transport in the low-temperature region. Moreover, we detect enhanced spatial fluctuations and marked deviations from the mean-field predictions in the stationary density profile inside both the hotter and cooler regions that are likely induced by emergent long-range correlations emerging from the critical subsystem.

The outline of this Chapter is as follows: In the following Sec. 2.2, we present the microscopic dynamical rules defining the KLS and (T)ASEP models, and describe their continuous coarse-grained description in terms of non-linear Langevin equations. We also introduce their scaling properties in the stationary state as well as in the physical aging scaling regime. In Sec. 2.3, we introduce our two-temperature KLS model with the temperature interfaces oriented perpendicular to the drive, and explain our Monte Carlo simulation algorithm. We then provide our numerical data and characterize the transient kinetics as well as the stationary current and density profiles in detail in Secs. 2.4 and 2.5.

2.2   Driven Lattice Gases

2.2.1   KLS Model Description

The Katz–Lebowitz–Spohn (KLS) model comprises a collection of N (classical) binary variables, either spin up / down $s_i = \pm 1$ or particle occupation numbers $n_i = \frac{1}{2}(s_i + 1) = 1, 0$, on a d-dimensional lattice with $L_\parallel \times L_\perp^{d-1}$ sites, subject to nearest-neighbor attractive Ising interactions and periodic boundary conditions. A spin or particle may exchange its position with any of its nearest neighbors with a fixed rate depending on the temperature and a uniform external drive field $E \geq 0$ that is oriented along the longitudinal ($\parallel$) direction [40, 41]. Spin exchange processes hence are biased along the direction of the applied field, and in conjunction with the periodic boundaries drive the system towards a genuine non-equilibrium stationary state. For such a steady state to be maintained in the presence of the external driving field, the system needs to be coupled to a thermal reservoir at fixed temperature T that absorbs heat flow produced by the current. Similarly to the Ising model, nearest-neighbor ferromagnetic interactions spur competition in the system between two processes: local ordering or domain wall annihilation, and domain wall formation accompanied with entropy production. As a result, the KLS driven lattice gas experiences a continuous phase separation transition in $d \geq 2$ dimensions when the conserved total magnetization of the system is set to vanish, $\sum_{i=1}^{N} s_i = 0$, or the particle density $\rho = \sum_{i=1}^{N} n_i / N = \frac{1}{2}$. In contrast to the equilibrium Ising model, the drive in the KLS system forces ordered domains to align into stripe-like clusters that are oriented along the $\parallel$ direction. It also raises the critical temperature, e.g., $T_c^{\mathrm{KLS}}(E \to \infty) \approx 1.41\, T_c^{\mathrm{eq}}$ in two dimensions [27]; and as discussed below, drastically alters the associated critical exponents.

The dynamics of the KLS model in $d = 2$ dimensions can be described in the lattice gas language by the following set of microscopic rules: Consider a half-filled driven lattice gas

that is defined on a torus with $L_\parallel \times L_\perp$ sites, with each site containing at most one particle, restricting the occupation number $n_i = n(x, y) = 0$ (empty site) or 1 (filled site). This constraint on the particle occupation number may be interpreted to reflect mutual hard-core repulsion. In addition, the driven KLS lattice gas is governed by nearest-neighbor attractive Ising interactions with uniform exchange coupling $\mathcal{J} > 0$,

$$H = -\mathcal{J} \sum_{i \neq j}^{N} s_i\, s_j = -4\mathcal{J} \sum_{i \neq j}^{N} \left(n_i - \tfrac{1}{2}\right) \left(n_j - \tfrac{1}{2}\right) \ . \tag{2.1}$$

The drive and temperature enter the model dynamics through the Markovian transition rates

$$R(\mathcal{C} \to \mathcal{C}') \propto \exp\left(-\beta \left[H(\mathcal{C}') - H(\mathcal{C}) - lE\right]\right) \ , \tag{2.2}$$

where $\beta = 1/k_\mathrm{B}T$, $\mathcal{C}$ and $\mathcal{C}'$ denote two distinct system configurations $\{s_i\}$ or $\{n_i\}$, $E > 0$ is the applied drive strength, and $l = +1, 0, -1$ respectively indicates hops along, transverse to, and against the external bias. For $E = 0$, detailed balance is restored and one recovers the Kawasaki exchange dynamics on the Ising lattice. As $E \to \infty$, particle motion or spin exchanges in the $\parallel$ direction cannot proceed against the drive, effectively restricting the transition options to $l = 1, 0$ (totally biased case). In the limit $T \to \infty$ ($\beta \to 0$), the nearest-neighbor Ising interactions become ineffective, and the KLS model reduces to the asymmetric exclusion process (ASEP) for finite driving field E, or the totally asymmetric exclusion process (TASEP) when $E \to \infty$.

2.2.2 (T)ASEP Model Description

The (totally) asymmetric exclusion process (T)ASEP represents one of the paradigmatic models of non-equilibrium dynamics, as the underlying conservation law and the hard-core

repulsion between particles induce spatially anisotropic generic scale invariance with non-trivial (i.e., non-diffusive) scaling exponents. Remarkably, exact solutions are available for the (T)ASEP in one dimension [9, 10, 38, 67].

(T)ASEP dynamics consists of (fully) biased particle diffusion on a lattice subject to site exclusion and periodic boundary conditions; the term "exclusion" again refers to the occupation number restriction $n_i = 0$ or 1. Provided the target lattice site is empty, the transition probabilities are set to $p_\parallel > q_\parallel$ and $p_\perp = q_\perp$ for hops along, against, and transverse to the drive direction, respectively. The hopping rate difference $\propto p_\parallel - q_\parallel$ in the $\parallel$ direction produces a non-zero probability current parallel to the drive that in combination with the periodic boundary conditions forces the system out of equilibrium. Henceforth we set both the lattice spacing and the microscopic hopping time step duration to unity. For a system with uniform density one then obtains the mean particle current $\langle J_\parallel \rangle = (p_\parallel - q_\parallel)\, \rho(1-\rho)$. In this non-equilibrium steady state, the microstates in the periodic (T)ASEP occur with equal probability [68] that is just given by the inverse of the total number of possible states for the N particles to be distributed on a lattice with $V = L_\parallel L_\perp^{d-1}$ sites, $P(V, N) = N!(V - N)!/V!$.

A much richer phenomenology emerges in the one-dimensional TASEP ($q_\parallel = 0$) with open boundary conditions where particles are injected into the system from a reservoir on one end with injection probability $\alpha \in [0, 1]$, and removed on the opposite boundary with ejection probability $\beta \in [0, 1]$. The non-equilibrium steady states in TASEP systems with such open boundaries depend on the values of those injection / ejection rates and can be classified into four distinct phases [38, 52, 69–71]:

- When $\beta < \min(\alpha, \frac{1}{2})$, the system is in the *high-density phase* with bulk density $\rho = 1 - \beta$ and average current $\langle J \rangle = \beta(1 - \beta)$.

- For $\alpha < \min(\beta, \frac{1}{2})$, the system resides in the *low-density phase* with bulk density $\rho = \alpha$

and average current $\langle J \rangle = \alpha(1 - \alpha)$.

- When $\alpha = \beta < \frac{1}{2}$, the system is in the *coexistence phase*. The particle density in this "mixed-state" region is inhomogeneous and in the stationary state follows a shock profile interpolating between the low- and high-density values α and $1-\alpha$. A mean-field calculation predicts a hyperbolic tangent density profile

$$\rho(x) = \tfrac{1}{2}\left(1 + k \tanh\left[k(x - x_0)\right]\right), \tag{2.3}$$

where the inverse length scale $k = 1 - 2\alpha = \sqrt{1 - \langle J \rangle / J_c}$ defines both the shock height and width; here $J_c = p_\parallel / 4$ denotes the critical current.

- When both $\alpha, \beta \geq \frac{1}{2}$, the system is in the *maximal current phase*. In this region the mean steady-state current $\langle J \rangle$ exceeds the critical current J_c. The mean-field calculation now yields a trigonometric tangent density profile

$$\rho(x) = \tfrac{1}{2}\left(1 - q \tan\left[q(x - x_0)\right]\right), \tag{2.4}$$

with $q = \sqrt{\langle J \rangle / J_c - 1}$.

In the high- or low-density phase, the density profile decays exponentially with finite characteristic length k^{-1}. However, for the maximal-current state, the characteristic length q^{-1} diverges as $J \to J_c$.

Another one-dimensional model variation relevant to this work is a TASEP lattice gas with slow bonds, or inhomogeneous TASEP [72]. In that case, particles hop across normal bonds with rate 1, but across slow bonds with the reduced rate $r < 1$. Remarkably, just introducing a single slow bond with $r < 1$ in the TASEP results in particle blockage at the position of this defect, and forces the steady-state current to decrease. The density of the particles before

and after the slow bond $\rho_\pm$ depends on the maximum stationary current $\langle J(r)\rangle$ that the system can sustain: $\rho_\pm = \frac{1}{2}\left(1 \pm \sqrt{1 - \langle J(r)\rangle/J_c}\right)$. An explicit expression for the maximal stationary current $\langle J(r)\rangle$ has been obtained by means of a series expansion for $r \lesssim 1$ in Ref. [73]; a general result for arbitrary values of r remains yet to be found.

2.2.3   Coarse-Grained Langevin Representation

For the driven KLS lattice gas no exact solution has been found to date. Yet one may formulate a coarse-grained mesoscopic continuous description, which subsequently allows for a thorough analysis by means of the dynamic renormalization group and determination of the associated scaling exponents. The starting point is the continuity equation for the conserved order parameter field

$$\frac{\partial s(\vec{x}, t)}{\partial t} = -\vec{\nabla} \cdot \vec{J}(\vec{x}, t), \tag{2.5}$$

where $s(\vec{x}, t) = 2[\rho(\vec{x}, t) - \langle \rho \rangle]$ represents the local magnetization density or density deviation from its mean $\langle \rho \rangle = \frac{1}{2}$. The conserved current density comprises three contributions, namely a relaxational term with Onsager coefficient D, a non-linear component proportional to the drive $\vec{\mathcal{E}}\rho(1-\rho) = \frac{1}{2}Dg(1-s^2)\hat{e}_\parallel$ that also incorporates the exclusion constraint, and Gaussian white noise $\vec{\eta}$ that introduces stochasticity in the system [42, 74, 75]:

$$\vec{J}(\vec{x}, t) = -D\vec{\nabla}\frac{\delta\mathcal{H}[s]}{\delta s(\vec{x}, t)} + \frac{\vec{\mathcal{E}}}{4}\left[1 - s(\vec{x}, t)^2\right] + \vec{\eta}(\vec{x}, t), \tag{2.6}$$

Since we are interested in the behavior near the continuum phase transition, we here employ the standard Landau–Ginzburg–Wilson Hamiltonian for a scalar order parameter [76]

$$\mathcal{H}[s] = \int d^d x \left(\frac{1}{2}\left[\vec{\nabla}s(\vec{x})\right]^2 + \frac{\tau}{2}s(\vec{x})^2 + \frac{u}{4!}s(\vec{x})^4\right), \tag{2.7}$$

where $\tau \propto |T - T_c|$ denotes the distance from the critical point, and $u > 0$ is the non-linear coupling driving the phase transition.

Taking the functional derivative of the Hamiltonian (2.7) and substituting Eq. (2.6) back into the continuity equation yields a Langevin equation that models the KLS dynamics. Near the critical point, fluctuations only need to be taken into account in the "soft" $(d-1)$-dimensional transverse ("$\perp$") spatial sector, since below T_c ordered stripes form only in alignment with the ("$\parallel$") drive direction. The critical KLS Langevin equation hence becomes (after straightforward rescaling):

$$\frac{\partial s(\vec{x},t)}{\partial t} = D\Big[c\nabla_\parallel^2 s(\vec{x},t) + \left(\tau - \nabla_\perp^2\right)\nabla_\perp^2 s(\vec{x},t) + \frac{u}{6}\nabla_\perp^2 s(\vec{x},t)^3 \\ + \frac{g}{2}\nabla_\parallel s(\vec{x},t)^2\Big] + \sigma(\vec{x},t), \tag{2.8}$$

where Dc and $D\tau$ now represent longitudinal and transverse diffusion coefficients, respectively, and $\sigma = -\vec{\nabla}\cdot\vec{\eta}$ constitutes conserved Gaussian white noise with zero mean $\langle\sigma\rangle = 0$ and correlations $\langle\sigma(\vec{x},t)\sigma(\vec{x}',t')\rangle = -2D\nabla_\perp^2\delta(\vec{x}-\vec{x}')\delta(t-t')$.

In a fully analagous manner, one may construct a coarse-grained mesoscopic description for the (T)ASEP; indeed, we merely need to omit the terms in Eq. (2.8) for the KLS model that pertain to critical fluctuations near T_c, and arrive at (again, after straightforward rescaling)

$$\frac{\partial s(\vec{x},t)}{\partial t} = D\left[\left(c\nabla_\parallel^2 + \nabla_\perp^2\right)s(\vec{x},t) + \frac{g}{2}\nabla_\parallel s(\vec{x},t)^2\right] + \sigma(\vec{x},t), \tag{2.9}$$

with conserved Gaussian white noise $\langle\sigma\rangle = 0$ and $\langle\sigma(\vec{x},t)\sigma(\vec{x}',t')\rangle = -2D\left(\tilde{c}\nabla_\parallel^2 + \nabla_\perp^2\right)\delta(\vec{x}-\vec{x}')\delta(t-t')$, where the ratio $w = \tilde{c}/c$ indicates the deviation from thermal equilibrium, since for $w = 1$ Einstein's relation and detailed balance are satisfied.

2.2.4   Stationary Scaling Exponents

Upon approaching the phase transition, the static and dynamical correlations described by Eq. (2.8) become strongly anisotropic, with longitudinal and transverse wave vectors scaling as $|q_\parallel| \sim |\vec{q}_\perp|^{1+\Delta}$. The dynamical correlation function consequently obeys the following scaling form in the steady state [58]:

$$C\left(x_\parallel, \vec{x}_\perp, t\right) \sim t^{-\zeta} \hat{C}\left(\tau |\vec{x}_\perp|^{1/\nu}, x_\parallel/|\vec{x}_\perp|^{1+\Delta}, t/|\vec{x}_\perp|^z\right), \qquad (2.10)$$

with the correlation length exponent ν, anisotropy exponent Δ, dynamic critical exponent z, and $\zeta = (d + \Delta - 2 + \eta)/z$. In addition, the non-linear coupling ratio u/g^2 turns out to be irrelevant in the renormalization group sense, and hence flows to zero under repeated scale transformations. For the determination of the associated critical KLS scaling exponents, one may thus set $u \to 0$, although of course this non-linearity drives the phase separation. Therefore, since the remaining non-linear term $\propto g$ in the KLS Langevin equation that originates from the drive and particle exclusion only affects the longitudinal spatial sector, one has $\eta = 0$, $\nu = 1/2$, and $z = 4$, as in the corresponding Gaussian model. Moreover, the single remaining independent critical anisotropy exponent is fixed by Galilean invariance, as an emerging symmetry on the continuous coarse-grained level, to be $\Delta = (8 - d)/3$, which is larger than its mean-field value $\Delta = 1$ in dimensions below the upper critical dimension $d_c = 5$. Consequently $\zeta = (d + \Delta - 2)/4 = (d + 1)/6$, equal to the order parameter growth exponent $\beta = z\nu\zeta/2 = \zeta$. These values of the scaling exponents for the critical KLS system were originally determined through careful field-theoretical analysis in Refs. [74, 75]; in Table 2.1 we list them for the two-dimensional case that we consider in this work. The detailed procedure for how the scaling exponents and the general scaling form can be obtained from the analysis of the Langevin equation is, e.g., presented in Ref. [24].

	Δ	z	ν	η	ζ
Critical KLS	2	4	1/2	0	1/2
(T)ASEP	0	2	–	0	1

Table 2.1: Scaling exponents for the critical KLS and (T)ASEP models in two dimensions (omitting the logarithmic corrections for the (T)ASEP).

For simpler non-critical driven diffusive systems such as the (T)ASEP, i.e., also the high-temperature phase of the KLS model, that are still governed by generic scale invariance, Eq. (2.10) reduces to

$$C\left(x_{\parallel}, \vec{x}_{\perp}, t\right) \sim t^{-\zeta} \hat{C}\left(x_{\parallel}/|\vec{x}_{\perp}|^{1+\Delta}, t/|\vec{x}_{\perp}|^{z}\right), \qquad (2.11)$$

where here $\zeta = (d + \Delta + z - 2 + \eta)/z = (d + \Delta)/2$, since of course again $\eta = 0$ and $z = 2$ as in the corresponding Gaussian approximation. The upper critical dimension is now $d_c = 2$, and the exact generic scaling exponents become $\Delta = (2 - d)/3$ and $\zeta = (d + 1)/3$ in dimensions $d \leq 2$. We note that in one dimension, Eq. (2.9) becomes identical to the noisy Burgers equation, and via the identification $s = -\nabla h$ also to the Kardar–Parisi–Zhang equation [77, 78] for the height fluctuation field h. At $d_c = 2$, one obtains logarithmic corrections to the mean-field scaling exponents $\Delta = 0$ and $\zeta = 1$ (which are not explicitly listed in Table 2.1).

2.2.5 Physical Aging Scaling

Following a rapid quench from an initial configuration that is quite distinct from the asymptotic stationary state, a system is said to be in a physical aging scaling regime if the following three properties hold: slow (i.e., non-exponential) relaxation, broken time translation invariance, and dynamical scaling [79]. In the KLS model all three signatures of physical aging scaling are observed when the system is quenched to the critical point from a completely dis-

ordered state [43]. In contrast, all distinct (T)ASEP microstates are equiprobable, whence the (T)ASEP physical aging scaling window is best accessed when the initial and final states differ drastically, e.g., when the simulation is initiated with an alternating "checker board" particle distribution [80]. In the non-equilibrium relaxation regime, the two-time auto-correlation functions for both the (T)ASEP and KLS (at T_c) driven lattice gases then follow a simple aging scaling form:

$$C(\vec{x} = 0; t, t_w) = t_w^{-\zeta} \, \hat{C}(t/t_w), \tag{2.12}$$

where t_w denotes the "waiting" time [43, 80]. The dependence of the correlation function on both t_w and t, not just on time difference $\tau = t - t_w$, signifies the breaking of the time-translation invariance.

Investigating physical aging phenomenona has proven especially useful for systems with conserved order parameter fields, since their aging scaling exponents can be related to the corresponding asymptotic steady state exponents [81]. Therefore, studying physical aging scaling serves as an independent way to obtain the non-equilibrium critical exponents. This becomes exceptionally useful for systems that display exceedingly slow relaxation towards their stationary states, which is in fact the case for the critical KLS model.

Measuring the auto-correlation function in Eq. (2.12) in our simulations, we have confirmed that the KLS driven lattice gas is governed by the (T)ASEP scaling exponents in the disordered phase. Remarkably, we observe the scaling of $C(t, t_w)$ with (T)ASEP aging scaling exponents already at $T = 1.0 > T_c^{KLS}(E, L \rightarrow \infty) \approx 0.8$. The fact that the KLS driven lattice gas relaxes akin to a fully disordered system with (T)ASEP non-equilibrium scaling exponents already at temperatures not far above T_c gave us the motivation to look for the dynamics of spatially inhomogeneous KLS systems with two interfaces governed by local

temperature gradients.

2.3 Two-Temperature KLS Model With Transverse Temperature Interface

2.3.1 Model Description

The two-temperature KLS model is a composite of two driven KLS lattice gases held at different temperatures on a ring torus, depicted schematically in Fig. 2.1(a). The two lattices are coupled by allowing particle exchange across the two interfaces. Alternatively, the model can be cast on a $L_\parallel \times L_\perp$ rectangular square lattice with periodic boundary conditions, where the extensions of the two subsystems in the "$\parallel$" direction along the drive are set by the parameter a as shown in Fig. 2.1(b). In the first subsystem with $x \in [0, aL_\parallel)$ with aspect ratio $0 < a < 1$, the temperature is taken to be $T_h > T_c$; whereas the second subsystem in the range $x \in [aL_\parallel, L_\parallel)$ is set, if not otherwise stated, at the critical temperature $T_l = T_c$. We shall henceforth refer to the two KLS subsystems according to their temperature: The region at $T_h > T_c$ temperature will be called "*hot*" or alternatively the "*TASEP-like*" subsystem, and we will name the region held at T_c the "*critical*" subsystem. We will also refer to the single-temperature system as the "*standard*" KLS model.

In our simulations, we fix the total density to $\rho = \frac{1}{2}$ in the two-temperature driven KLS lattice gas, in order to avoid triggering kinetic waves in the TASEP-like subsystem, and to be able to access the continuous non-equilibrium phase transition in the critical KLS subsystem. We also choose the drive strength to be (formally) $E = \infty$ to reduce the crossover time necessary to approach the non-equilibrium steady state. This $E \to \infty$ limit forbids all hops against the drive, regardless of any particle's nearest-neighbor configuration, and hence corresponds

(a)

(b)
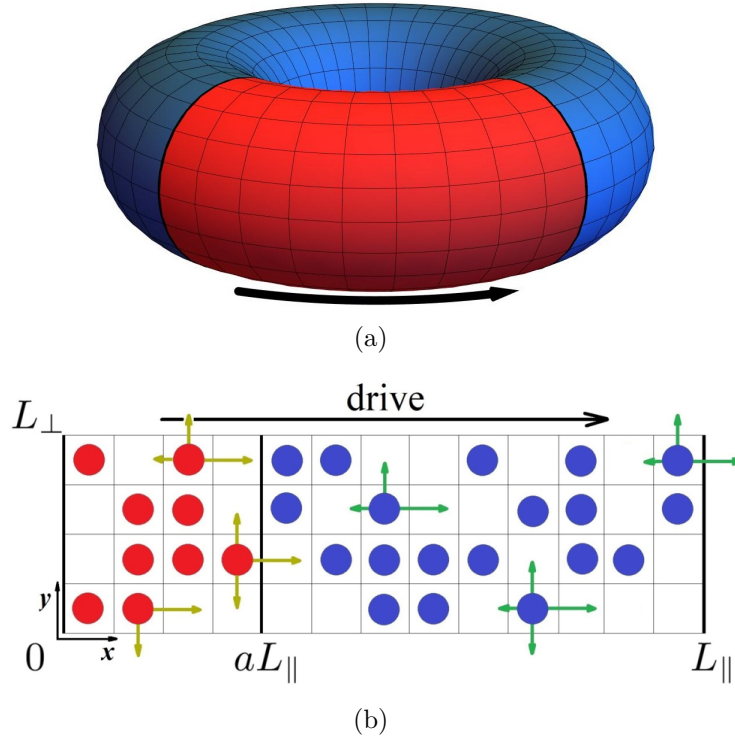
Figure 2.1: (a) The two-temperature driven KLS lattice gas on a ring torus. The red sector of the torus is coupled to a reservoir at temperature $T_h > T_c$, while the blue sector is coupled to a reservoir at the critical temperature $T_l = T_c$. The black arrow indicates the direction of the drive. (b) The two-temperature driven KLS lattice gas on a two-dimensional square lattice with periodic boundary conditions. The $[0, aL_{\parallel})$ region of the lattice (with red-colored particles) is maintained at $T_h > T_c$, while the rest of the lattice is held at $T_l = T_c$. The colored arrows indicate possible hopping processes, with rates given by Eq. (2.2).

to the completely biased nearest-neighbor hopping in the longitudinal direction. Note that consequently the temperatures in either heat bath only affect particle movements transverse to the drive. While the particular choice of the drive strength affects the values of the critical temperature, net stationary particle current, and overall time scale, it does not qualitatively change the KLS non-equilibrium steady state provided the drive strength satisfies $\beta E \gg 1$ [27].

2.3.2   Monte Carlo Simulations

We simulate the dynamics of the two-temperature driven KLS lattice gas on a two-dimensional torus or square lattice with periodic boundary conditions, see Fig. 2.1, using the standard Metropolis algorithm with conserved Kawasaki exchange dynamics. If not otherwise stated, the simulations are initiated with a random distribution of N particles over the entire $L_\parallel \times L_\perp$ lattice, and proceed with random sequential updates. Performing $L_\parallel \times L_\perp$ updates per single Monte Carlo step (MCS), we allow every particle to be selected once on average for the update. If a chosen lattice site is occupied, we proceed with randomly selecting the hop direction from the four possible nearest-neighbor target sites with probability $1/4$. The proposed hop is then performed to an empty lattice site with a probability that depends on the drive orientation and strength, as well as on the nearest-neighbor configurations of both departure and arrival sites. The acceptance probability for the proposed move is set by

$$P(\mathcal{C} \to \mathcal{C}') = \min\left\{1, \exp\left(-\beta[H(\mathcal{C}') - H(\mathcal{C}) - lE]\right)\right\}, \tag{2.13}$$

where $H(\mathcal{C})$ and $H(\mathcal{C}')$ are the energy of the initial and final configurations, respectively, computed from Eq. (2.1).

We use a different expression for the acceptance probability for the hops across the temperature boundaries:

$$P(\mathcal{C} \to \mathcal{C}')\big|_{\beta_1 \to \beta_2} = \min\left\{1, \exp\left(-\beta_2 H(\mathcal{C}') + \beta_1[H(\mathcal{C}) + lE]\right)\right\}, \tag{2.14}$$

where β_1 and β_2 denote the inverse temperatures pertinent to the particle's initial and final position. In the $E \to \infty$ limit, simply all hops along the drive will be accepted, while all hops against the drive are strictly prohibited; the Ising Hamiltonian consequently only

(a) $3,000$ MCS
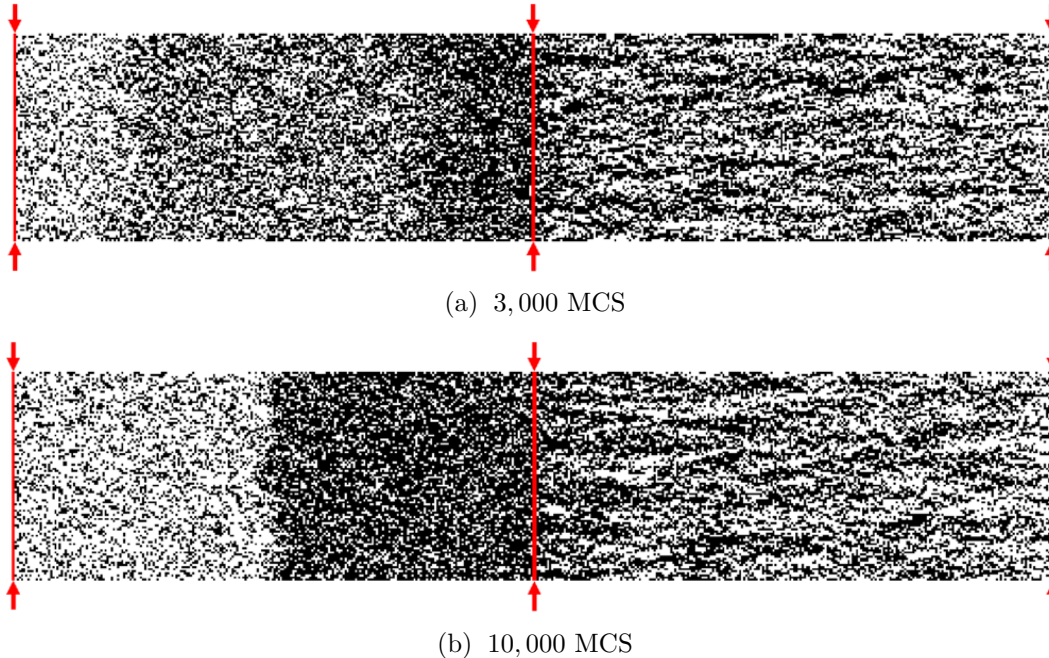
(b) $10,000$ MCS

Figure 2.2: Simulation snapshots of the two-temperature KLS driven lattice gas with $L_\parallel = 500$ and $L_\perp = 100$ after (a) $3,000$ Monte Carlo steps (MCS) and (b) $10,000$ MCS. The thin verticle red line indicates one of the temperature interfaces; the other interface is located at $x = 0$ and $x = L_\parallel$. The left part of the lattice in the figure is coupled to the temperature bath at $T_h = 2.0$, and the right part to the $T_l = 0.8 \approx T_c$ reservoir.

affects hops transverse to the drive direction. Since the temperature interfaces in this work are oriented perpendicular to the drive, our particular choice (2.14) to handle the hops across the subsystem boundaries in fact would not matter. We will henceforth measure the temperature T that solely controls the probability of particle motion transverse to the drive in units of $\mathcal{J}/k_{\mathrm{B}}$.

2.4   Transient regime

In order to access the physical aging scaling regime in the hot or TASEP-like subsystem (held at temperature $T_h > T_c$), we start from highly correlated initial conditions and fill the whole lattice with particles in an alternating manner, i.e., a checker-board pattern. Shortly

after the beginning of the simulation, we observe the formation of two density shock waves in the hot subsystem, as seen in the simulation snapshot in Fig. 2.2(a): The low-density shock wave nucleates at the boundary (at $x = 0$ and $x = L_\parallel$) that particles cross to enter the hot subsystem from the cooler side where $T_l = T_c$; the high-density shock wave emerges at the interface (located at $x = aL_\parallel$) where particles leave the TASEP-like subsystem. These high- and low-density shocks traverse the hot region, moving toward each other with the same constant velocity; its value is consistent with the one determined for the one-dimensional TASEP with open boundaries in the coexistence phase [82]:

$$v = \frac{\langle J_{\parallel,st} \rangle - \langle J_{\parallel,st}(T_h) \rangle}{\rho_\pm - \rho} \, , \tag{2.15}$$

where $\langle J_{\parallel,st}(T_h) \rangle$ is the mean drive-induced steady-state particle current in the *standard* KLS model at temperature T_h, whereas $\langle J_{\parallel,st} \rangle$ represents the mean drive-induced steady-state particle current in the *two-temperature* KLS system; $\rho_\pm$ denote the average high and low densities on either side in the hot subsystem, and $\rho = \frac{1}{2}$ is the total density in the lattice.

Once the two density shock waves have met in the middle of the hot subsystem, a stationary domain wall forms that completely separates the subsystem into low- and high-density phases, as shown in the late-time snapshot, Fig. 2.2(b). Recording the density profile for the two-temperature KLS model enables us to follow the temporal evolution of the system, and allows us to obtain the kink's height and width as shown in Fig. 2.3. We will discuss the intriguing steady-state shape of the density profile in the following section 2.5.

Meanwhile, the critical subsystem (at temperature $T_l = 0.8 \approx T_c$) develops long correlated clusters that are oriented along the drive. In contrast to the standard KLS model, the stripe-like clusters in the critical region of the two-temperature KLS system become more dense at the boundary where particles enter the critical domain, and less dense at the boundary
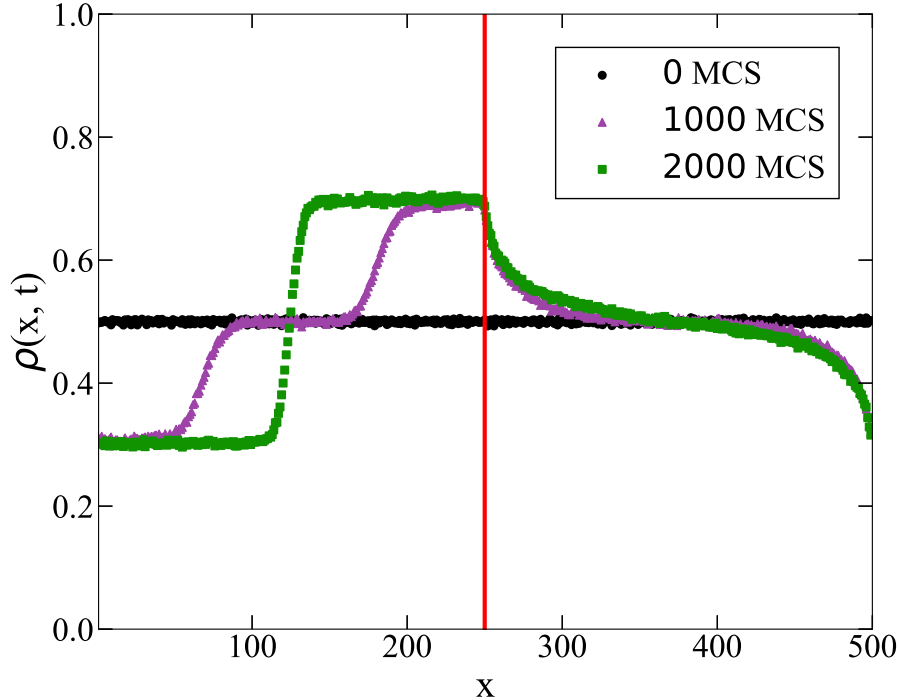
Figure 2.3: Density profiles of the two-temperature KLS driven lattice gas with dimensions $L_\parallel = 500$, $L_\perp = 250$ at different simulation times. The subsystem length ratio is 1:1 ($a = 0.5$); one temperature interface is indicated by the vertical red line, while the other one is located at $x = 0$ and $x = L_\parallel$. The hot subsystem is held at $T_h = 2.0$ and the critical subsystem at $T_l = 0.8 \approx T_c$. The data are averaged over 100 independent realizations.

where particles leave this region. The extended correlated particle clusters continue to alter their shape even after the two density shock waves have met one another in the hot region, eventually forming funnel-like structures that traverse the entire critical subsystem. The process of the long density tails spreading into the critical subsystem happens on a much longer time scale, which we have not been able to reliably estimate; perhaps this kinetics is governed by a power law.

The emergence of these spatial inhomogeneities in the two-temperature KLS driven lattice gas prevents us from accessing the physical aging scaling regime in the parts of the lattice
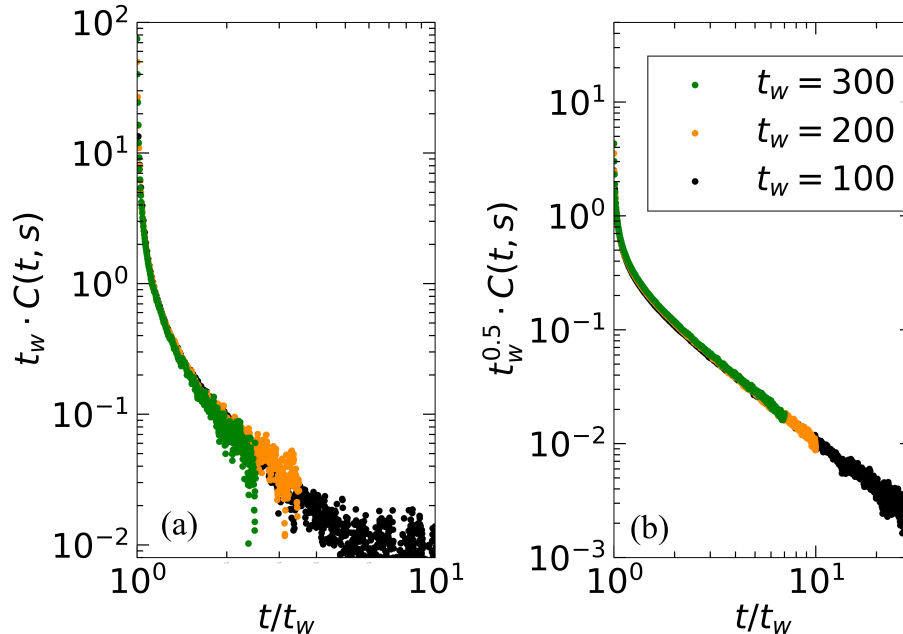
Figure 2.4: Aging scaling plots of the two-time density auto-correlation function in the two-temperature KLS driven lattice gas with dimensions $L_\parallel = 1000$, $L_\perp = 64$. The data are collected following a quench from a random initial state to the high-temperature state ($T_h = 5.0$) in the left graph, and to the critical point ($T_l = 0.8 \approx T_c$) in the right plot, in the central columns of the hot and critical subsystems, respectively. The points in each curve represent averages over $1,000,000$ independent realizations.

with non-uniform density. However, the density waves nucleate at the temperature interface boundaries and the approximate time it takes for them to reach the center of the hot subsystem is $\Delta t \approx a L_\parallel / 2v$, since $a L_\parallel$ is the length of the hot subsystem along the drive direction. Until that moment, the central parts of the two subsystems do not experience any mutual coupling, and are effectively independent. One would hence expect the initial non-equilibrium relaxation dynamics in the TASEP-like subsystem to be governed by the TASEP aging scaling exponents, and the critical subsystem correspondingly characterized by the critical KLS aging exponents. To verify this assertion, we have probed the aging scaling exponent ζ separately in the middle columns of both the hot and critical subsystems. Applying the simple aging scaling form (2.12), we demonstrate in Fig. 2.4 that the obtained
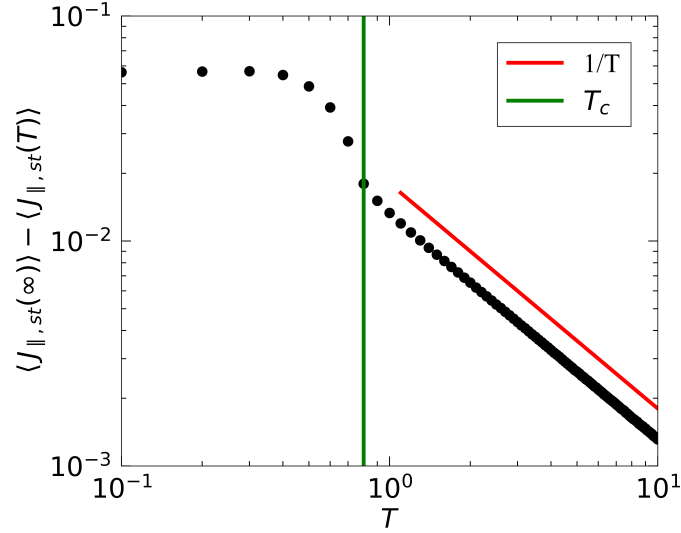
(a)
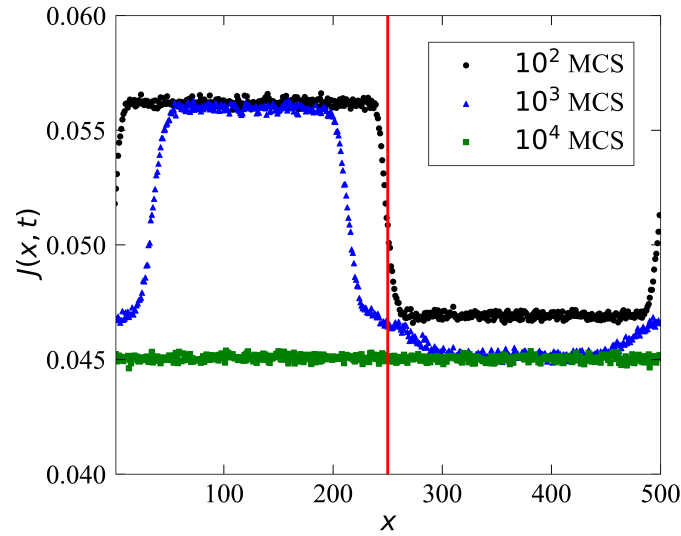
(b)

Figure 2.5: (a) The drive-induced current at different temperatures in the standard (uniform) KLS driven lattice gas with dimensions $L_\parallel = 1000$, $L_\perp = 64$. The data are collected after $20,000$ MCS when the system is in the steady state for $T > T_c$, but still in a very slowly evolving transient state for $T \leq T_c$. The data are averaged over 1000 MCS and over 100 independent realizations. (b) Transient current profiles of the two-temperature KLS driven lattice gas with dimensions $L_\parallel = 500$, $L_\perp = 250$ at different times. The subsystem ratio is 1:1 ($a = 0.5$) and one of the temperature interfaces is indicated by the red line. The hot subsystem is held at $T_h = 2.0$ and the critical subsystem at $T_l = 0.8 \approx T_c$. The data are averaged over $10,000$ independent realizations.

aging scaling exponents from the central part of the hot and critical subsystems are indeed identical to the predicted and reported values for the two-dimensional (T)ASEP ($\zeta = 1$) and standard KLS ($\zeta = 1/2$) models, respectively [43, 80].

Once the two density shock waves meet at the center of the TASEP-like subsystem, the initial aging scaling terminates, and the subsystem becomes completely segregated into the high- and low-density regions, with the single domain wall centered in the middle of the hot subsystem. This phase separation in the high-temperature region can be explained by considering the mean drive-induced particle current in the two-temperature KLS system. However, before examining this inhomogeneous two-temperature modification of the KLS model, it is useful to first analyze how the mean steady-state particle current depends on the temperature in the original standard KLS driven lattice gas. To our knowledge, only Katz et al. have studied this temperature dependence of the mean steady-state particle current in their original paper [41]. They showed that the mean steady-state current $\langle J_{\parallel,st}(T) \rangle$ assumes the value $p_{\parallel}\rho(1-\rho)$ in the infinite-temperature limit, and drops drastically in the ordered phase due to the stripe-like phase separation of the system, with a cusp discontinuity at the critical temperature T_c. Seeking to uncover the functional dependence of $\langle J_{\parallel,st}(T) \rangle$ on T, we found that the mean steady-state current in the standard KLS model decays linearly with inverse temperature $\langle J_{\parallel,st}(\infty) \rangle - \langle J_{\parallel,st}(T) \rangle \sim T^{-1}$ in the disordered phase $(T > T_c)$, as shown in Fig. 2.5(a). This inverse temperature power law clearly originates from the decrease of the effective Ising attractive interactions with T.

Since the two-temperature KLS driven lattice gas must of course reduce to the standard KLS model for $a = 0$ or 1, one would expect the mean steady-state particle current $\langle J_{\parallel,st} \rangle$ in the two-temperature KLS system at temperatures T_h and $T_l < T_h$ to be bounded between the standard KLS values of the mean steady-state current $\langle J_{\parallel,st}(T_h) \rangle$ and $\langle J_{\parallel,st}(T_l) \rangle$. We have confirmed this expectation with our simulations, and show in Fig. 2.5(b) that initially the

hot and critical subsystems have distinct local current values. But once the two-temperature KLS driven lattice gas has reached its steady state, the particle current $\langle J_{\parallel,st} \rangle$ becomes uniform across the system and takes values in the range $[\langle J_{\parallel,st}(T_l) \rangle, \langle J_{\parallel,st}(T_h) \rangle]$. One may draw an analogy between the two-temperature KLS driven lattice gas and the TASEP with a slow bond to illustrate how the drop in the current causes a particle blockage in the two-temperature KLS model. In the TASEP with a slow bond, the defect bond plays the role of a bottleneck that impedes the transport in the entire chain. Similarly, in the two-temperature KLS driven lattice gas the entire critical subsystem serves as the bottleneck for the particles emanating from the hot region. Once these particles enter the critical subsystem, they become stuck inside the large correlated clusters. This causes the clogging at the hot-to-critical temperature interface, and eventually induces the density phase separation in the hot subsystem.

Indeed, we observe the phase separation inside the hot subsystem even when the temperature T_l of the cooler subsystem is above the critical temperature, $T_h > T_l > T_c$: When both subsystems are in the disordered phase, the subsystem with the lower temperature will play the role of the bottleneck region since according to Fig. 2.5(a) it sustains a lower stationary mean particle current.

2.5   Steady-State Properties

2.5.1   Steady-State Particle Current

Once the density profile ceases altering its shape and the drive-induced particle current becomes uniform across the whole lattice and does not change with time anymore, the two-temperature KLS driven lattice gas has reached its non-equilibrium stationary state. The
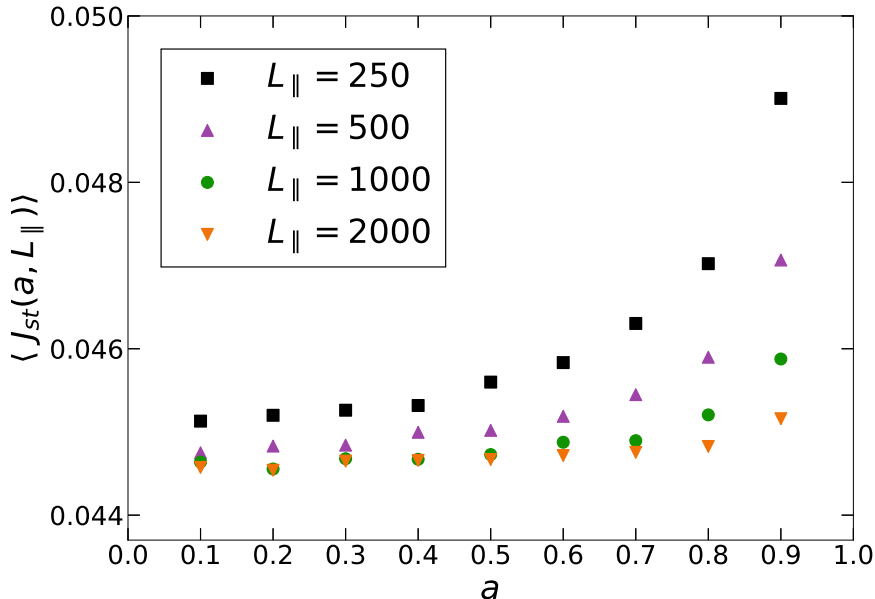
Figure 2.6: The steady-state current for different subsystem ratios and overall system sizes. The aspect ratio parameter a indicates the position of the hot-to-critical subsystems' interface. The hot subsystem was held at $T_h = 2.0$, while the critical subsystem was maintained at $T_l = 0.8 \approx T_c$. The lattice width $L_\perp = 64$ was used for the simulations, and the data were averaged over $5,000$ MCS and over 10 independent realizations.

mean steady-state particle current $\langle J_{\parallel,st} \rangle$ in the two-temperature KLS driven lattice gas depends non-trivially on all system parameters: the system's geometry determined by $L_\parallel$, $L_\perp$ and the aspect ratio a, as well as both temperatures $T_h > T_l$. As we have mentioned in the preceding section, these temperatures of the hot and cooler subsystems T_l, T_h set the upper and lower boundaries for $\langle J_{\parallel,st} \rangle$ that are approached when the parameter a either takes the value 1 or 0 (rendering the system uniform).

We observe the two-temperature KLS model to display intriguing and subtle finite-size features. For example, in Fig. 2.6 we show how the mean steady-state particle current $\langle J_{\parallel,st} \rangle$ varies with the aspect ratio a for different total lattice lengths $L_\parallel$. As in the TASEP with a slow bond, $\langle J_{\parallel,st} \rangle$ drops significantly even when even just a small fraction $1 - a \ll 1$ of the lattice is maintained at the critical temperature, or in fact at any T_l with $T_c < T_l < T_h$; i.e., the lattice sites that are coupled to the lower-temperature bath dominantly affect the result-
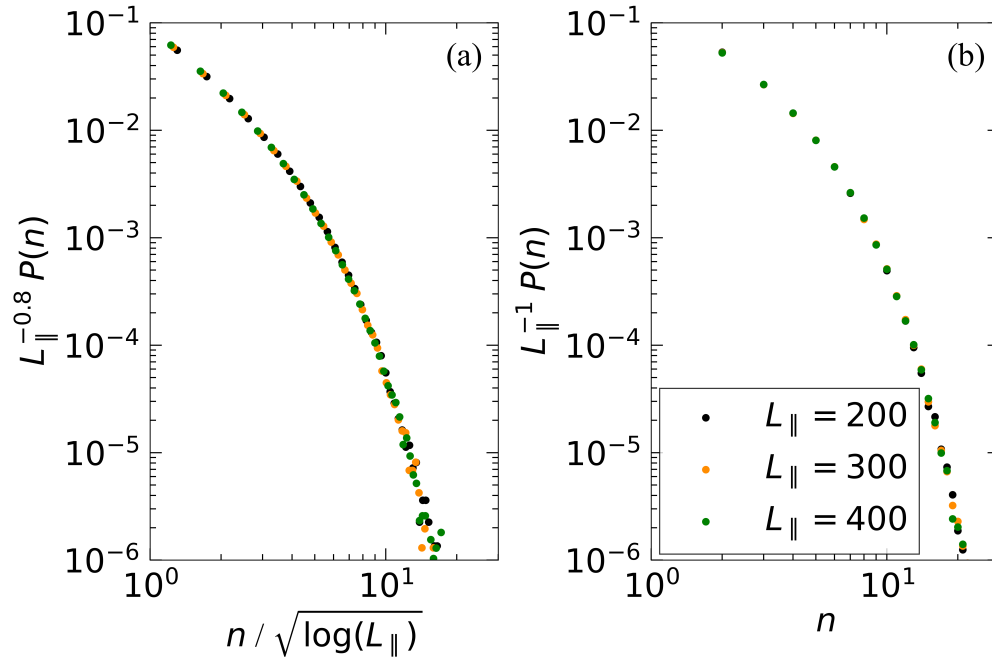
Figure 2.7: Double-logarithmic plots of the probability distribution $P(n)$ of the cluster sizes n in the cooler subsystem held at (a) $T_l = 0.8 \approx T_c$, and (b) $T_l = 2.0 > T_c$, while the hot region is maintained at (a) $T_h = 2.0$, and (b) $T_h = 5.0$, respectively. The lattice width $L_\perp = 32$ was used for the simulations. The data for each curve were collected in the steady state after $L_\parallel^2$ MCS and were averaged over $1,000$ independent realizations.

ing mean stationary current values. For the same subsystem ratio a but different $L_\parallel$, the mean steady-state particle current is lower in systems with a greater number of effectively slow lattice sites controlled by the heat bath set to temperature T_l; hence $\langle J_{\parallel,st} \rangle$ becomes reduced for larger $L_\parallel$.

In contrast to the TASEP with a slow bond, the "defect" region in the two-temperature KLS driven lattice gas emerges in the critical subsystem owing to the Ising attractive interactions that instigate the formation of the long horizontal clusters. To gain better insight into the steady-state particle current dependence on the system size $L_\parallel$, we have analyzed single-row wide clusters in the critical subsystem. We apply the same rules to define a cluster that Katz et al. used in their original work [41] to study the standard KLS clusters size histogram: A

single-row wide particle cluster is assigned a length n if it has empty sites at its ends, and no empty sites inside the cluster. Thus, according to this definition, a single separate particle is considered to be a cluster of size $n = 1$, and a completely occupied row corresponds to a cluster of size $n = L_\parallel$.

After reaching the steady state in our simulation, we have collected all clusters in the critical subsystem, which is held at T_c, into n-sized bins, and subsequently constructed their histogram. Thereby arriving at an estimate for the probability distribution of the cluster size $P(n)$, we have found the following scaling with system size $L_\parallel$:

$$P(n) = L_\parallel^\alpha \, \mathcal{F} \left(n/\xi_\parallel(L_\parallel) \right), \tag{2.16}$$

where we obtain $\alpha \approx 0.8$ from the optimal data collapse, and the characteristic correlation length or typical cluster size $\xi_\parallel(L_\parallel) \sim \sqrt{\log L_\parallel}$ grows logarithmically with system size $L_\parallel$, as shown in Fig. 2.7(a). Yet if T_l in the cooler subsystem is set above the critical temperature, $T_h > T_l > T_c$, the finite-size scaling exponent in Eq. (2.16) changes its value to $\alpha \approx 1$, while the correlation length $\xi_\parallel$ becomes constant and of $\mathcal{O}(1)$, see Fig. 2.7(b). When the cooler subsystem resides in the KLS disordered phase, long-range spatial correlations disappear, and particles move essentially freely and unimpeded through the lower-temperature region.

From these observations we conclude that the overall decrease of the mean steady-state particle current in the two-temperature KLS model with $L_\parallel$ occurs because the characteristic cluster size in the critical subsystem increases logarithmically with the system length $L_\parallel \sim L_\perp^{1+\Delta} = L_\perp^3$ and hence also with its width $L_\perp$. Moreover, the formation of these correlated critical clusters markedly affects the dynamics of the phase interface fluctuations in the hot subsystem, as we will discuss in the final subsection 2.5.3 below.

2.5.2   Steady-State Density Profile

For the two-temperature KLS model, the shape of the density profile in Fig. 2.3 resembles a hyperbolic tanh-function in the hot region and a trigonometric tan-function in the low-temperature subsystem. Remarkably, hyperbolic tangent- and tangent-shaped density profiles have been observed in the one-dimensional TASEP with open boundaries in the coexistence and the maximal-current phases, respectively [38, 52, 67, 69–71]. This striking similarity calls for a quantitative comparison of the two-temperature KLS steady-state density profiles with the known mean-field solutions for the one-dimensional TASEP with open boundaries, as given by Eqs. (2.3) and (2.4). In the following, we discuss the unique properties of the density profiles in both regions of the two-temperature KLS system. In particular, we wish to ascertain whether the mean-field description for the TASEP with open boundaries may be adapted to characterize the two-temperature KLS density profiles for two separate cases, namely either when the cooler subsystem is maintained at the critical temperature $(T_l = T_c)$, or when it is held at a temperature just above the critical one.

Critical Subsystem

We first carefully examine the critical subsystem, which is maintained at $T_l = 0.8 \approx T_c$. We have found that the density field $\rho(x)$ does not follow the mean-field tangent solution given by Eq. (2.4) as proposed for the maximal current phase in the TASEP with open boundary conditions. Instead, the excess density $\rho(x) - \langle \rho \rangle$ with $\langle \rho \rangle = \frac{1}{2}$, near the boundaries of the critical subsystem displays a power law decay away from the interface with exponent 1/3, as shown in Fig. 2.8. This decay exponent is indeed characteristic of the critical KLS universality class, as we demonstrate with the general KLS scaling form (2.10) of the correlation
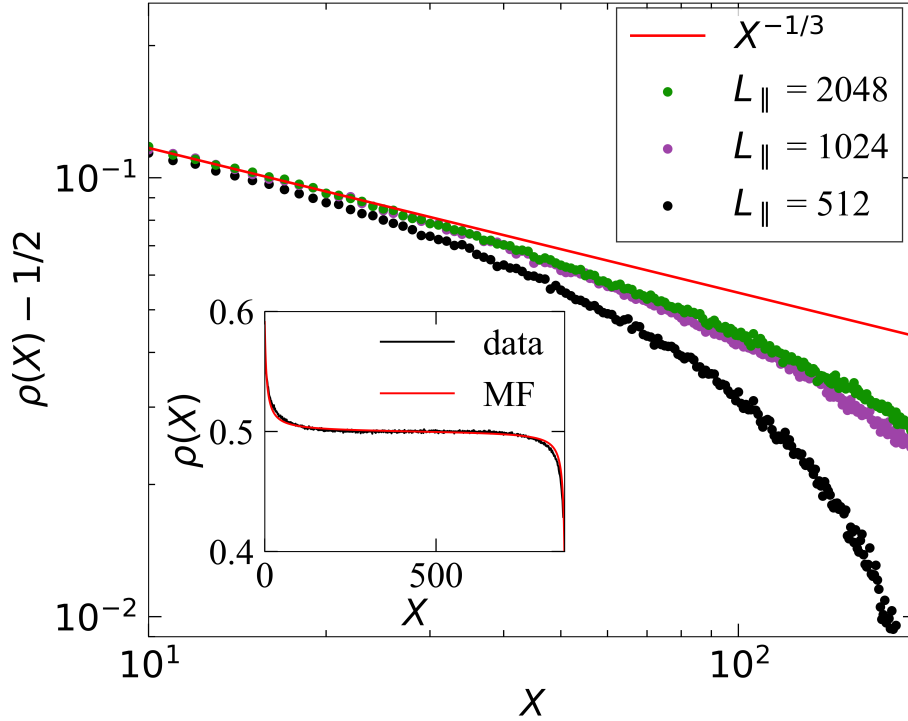
Figure 2.8: Decay of the density $\rho(x)$ in the critical subsystem, where x is the distance from the hot-to-critical temperature interface. The hot subsystem is held at $T_h = 2.0$; the hot and critical subsystem size ratio is chosen to be 1:8. Different curves correspond to the different system lengths $L_\parallel$, but with identical width $L_\perp = 64$. The data points in each curve reflect averages over $10,000$ independent realizations. The inset compares the tan-like part of the density profile with the mean-field result when both subsystems are maintained at temperatures above the critical one, namely at $T_h = 10.0$ and $T_l = 5.0$, respectively. The system length is $L_\parallel = 1,000$, the system width $L_\perp = 64$, and the hot and critical subsystem size ratio is chosen to be 1:8. The data shown in the inset were averaged over $10,000$ independent realizations.

function at the critical point $(\tau = 0)$ and $x_\perp = 0$,

$$C(t, x_\parallel) = t^{-\zeta}\, \widetilde{C}(t/x_\parallel) \sim x_\parallel^{-\zeta\, z/(1+\Delta)} \tag{2.17}$$

at $t = 0$. Upon identifying $x = x_\parallel$, which now indicates the distance measured parallel to the drive direction from the hot-to-critical temperature interface (i.e., from the red line to

the right in Fig. 2.3), we thus find for the excess density

$$\left|\rho(x) - \tfrac{1}{2}\right| \sim x^{-\zeta z/[2(1+\Delta)]} = x^{-1/3} \tag{2.18}$$

in two dimensions, with $\Delta = 2$ and $z = 4$ representing the critical KLS anisotropy and dynamical exponents, and $\zeta = \Delta/4 = 1/2$; see Table 2.1. From the graphs pertaining to different $L_\parallel$ in the main plot on Fig. 2.8, we infer that the deviations from this power law are due to the finite size of the system, and posit that the excess density will follow the $x^{-1/3}$ algebraic decay in the thermodynamic limit.

Our simulation data in the inset of Fig. 2.8 indicate that the density profile in the cooler subsystem follows the mean-field solution when the temperature $T_l > T_c$ in that region is raised above the critical value. Thus we may directly adapt Eq. (2.4) for the one-dimensional TASEP in the maximal current phase to the two-temperature KLS model, setting $x_0 = (1 + a)L_\parallel/2$. In contrast to the TASEP formula the inverse characteristic length now is $q = \sqrt{\langle J_{\parallel,st}\rangle/J_{\max} - 1}$, with the mean steady-state current $\langle J_{\parallel,st}\rangle$ in the two-temperature KLS model, and where $J_{\max}$ is the cooler subsystem maximal current that is equal to the mean steady-state current $\langle J_{\parallel,st}(T_l)\rangle$ in the standard KSL model at temperature T_l.

Hot Subsystem

Our simulations show that the mean-field solution (2.3) for the one-dimensional TASEP with open boundaries in the coexistence phase can be readily adapted to the two-temperature KLS driven lattice gas to describe the density profile of the hot subsystem, with $x_0 = aL_\parallel/2$. Here the inverse characteristic length is $k = \sqrt{1 - \langle J_{\parallel,st}\rangle/J_{\max}}$, with the mean steady-state current $\langle J_{\parallel,st}\rangle$ in the two-temperature KLS model, and $J_{\max}$ denoting the hot subsystem maximal current, i.e., the mean steady-state current $\langle J_{\parallel,st}(T_h)\rangle$ in the standard KLS model

at temperature T_h. This mean-field expression works exceptionally well far away from the phase interface, and if $T_h > T_l > T_c$. Having obtained the density profiles and the mean steady-state particle currents from our simulations for systems at different temperatures T_h, we show in Fig. 2.9 that the asymptotic high and low densities at the boundaries of the hot subsystem are completely determined by the value of the inverse characteristic length k,

$$\langle \rho_\pm \rangle = \tfrac{1}{2}(1 \pm k) = \tfrac{1}{2} \left[1 \pm \left(1 - \langle J_{\|,st} \rangle / J_{\max} \right)^{1/2} \right]. \tag{2.19}$$

However, small but clearly noticeable deviations from this expression are observed, when both subsystems are maintained at temperatures close to T_c, $2.0 > T_h, T_l \gtrapprox T_c \approx 0.8$ (on the left side of the figure), signifying the influence of critical fluctuations across the entire system that are not captured by the mean-field approximation. Indeed, instead of the exponent $1/2$ in Eq. (2.19), our best data fit gives the value 0.48, yet with error bars that are still compatible with the mean-field exponent 0.5. We also observe that the prefactor in front of the brackets in Eq. (2.19) is always smaller than $\frac{1}{2}$ in systems with $T_l \approx T_c$; i.e., the actual height of the kink in the hot subsystem is reduced as compared to the mean-field prediction.

Close to the phase interface, the domain wall width differs significantly from the mean-field prediction. This discrepancy clearly arises from the presence of non-trivial phase interface fluctuations that are not accounted for by the mean-field approximation. Examining a series of successive simulation snapshots, we have confirmed that the phase interface shape in the hot subsystem is in fact changing with time. The following subsection is devoted to a more detailed exploration of the interface fluctuations at the boundary between the high- and low-density phases within the high-temperature region.
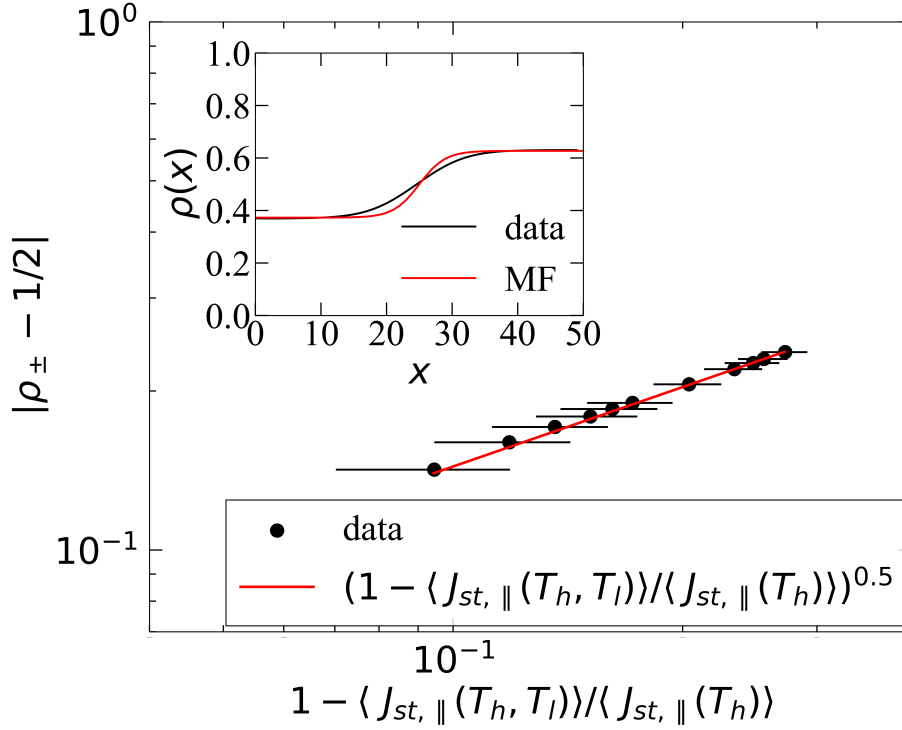
Figure 2.9:   Double-logarithmic plot of the hot subsystem's low and high densities $\rho_\pm$ as a function of the mean steady-state particle current and the maximal current for different temperatures of the hot subsystem. The cooler subsystem is held at the critical temperature, $T_l = 0.8 \approx T_c$. The system size is $L_\parallel = 1,000$ and $L_\perp = 64$ and the hot-to-critical subsystem ratio is 1:8. All data points were averaged over $10,000$ independent realizations. The inset compares the tanh-like part of the density profile with the mean-field result when both subsystems are maintained at temperatures above the critical one, namely at $T_h = 5.0$ and $T_l = 2.0$, respectively; here the hot-to-critical subsystem ratio was set to 1:19 ($a = 0.05$). The data in the inset were averaged over $10,000$ MCS and over $1,000$ independent realizations.

2.5.3   Phase Interface Fluctuations

Certain features of the two-temperature KLS driven lattice gas make studying the phase interface fluctuations within the hot subsystem with conventional means problematic. First, instead of two well-separated phases of particles and holes, the hot subsystem is comprised of high- and low-density phases, which renders the task of tracing the phase interface ambiguous and rather arduous. Moreover, we cannot determine the exact time when the phase interface is fully formed. At the time instant when the two density shock waves meet at the middle
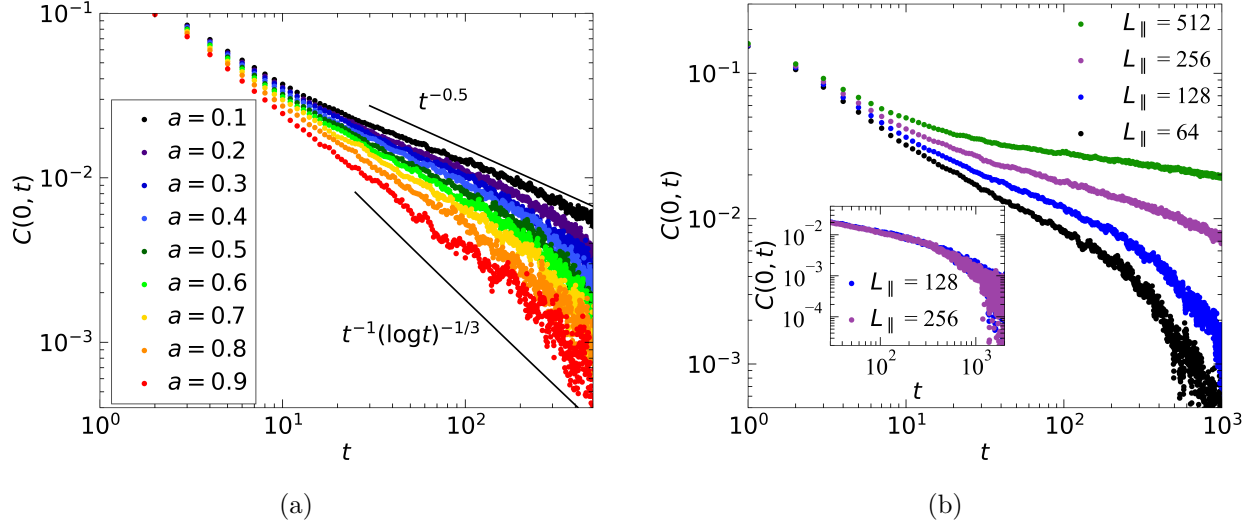
Figure 2.10: Double-logarithmic plots of the steady-state auto-correlation function decay with time at the phase interface within the hot subsystem of the two-temperature KLS driven lattice gas: (a) for different aspect ratios a at fixed lattice dimensions $L_\parallel = 64$ and $L_\perp = 32$; (b) for different total system lengths $L_\parallel$ at fixed width $L_\perp = 32$ and hot-to-critical subsystem ratio 1:1 ($a = 0.5$). The inset compares two systems with different $L_\parallel$ and aspect ratios a, but with the same mean steady-state particle current $\langle J_{\parallel,st} \rangle$. All data shown pertain to $T_h = 2.0$ and $T_l = 0.8 \approx T_c$. In all graphs, each data point was averaged over $50,000$ realizations.

of the hot subsystem, the particles at the center of the region are still uniformly distributed; only a few hundred Monte Carlo steps later the interface becomes fully established.

To circumvent the outlined obstacles, we have decided to monitor the temporal decay of the steady-state auto-correlation function from the time instant t_{ss} when the mean total particle current in the system does not change anymore,

$$C(\vec{x} = 0; t - t_{ss}) = \frac{1}{L_\perp} \sum_{j=1}^{L_\perp} \left[\langle n_{x^*,j}(t) n_{x^*,j}(t_{ss}) \rangle - \langle n_{x^*,j}(t) \rangle \langle n_{x^*,j}(t_{ss}) \rangle \right], \qquad (2.20)$$

where n represents the occupancy of the site, and $x^* = aL_\parallel/2$ is the location of the column in the center of the hot subsystem around which the phase interface forms. This steady-state density auto-correlation function reflects the dynamics of interface fluctuations: Comparing

successively taken snapshots of the center column indicates how fast the phase interface shape varies with time.

Asymptotically, both the (T)ASEP and KLS auto-correlations decay algebraically $C(0, t) \sim t^{-\zeta}$ as $t \rightarrow \infty$, where in two dimensions $\zeta = 1$ for the (T)ASEP, and $\zeta = 1/2$ for the critical KLS model, see Table 2.1. More precisely, the TASEP auto-correlations display logarithmic corrections to the mean-field power law at the upper critical dimension $d_c = 2$, $C(0, 0, t) \sim [t(\log t)^{1/3}]^{-1}$ [83]. Hence we expect the following range for any effective, i.e., potentially still size- and time-dependent auto-correlation decay exponent: $1/2 \leq \hat{\zeta} < 1$. When both temperatures of our inhomogeneous KLS system are set far above the critical temperature, it indeed behaves like a two-dimensional (T)ASEP, with the auto-correlation function (2.20) decaying essentially linearly with time irrespective of the aspect ratio.

Yet if we set $T_l = 0.8 \approx T_c$, we have found after extensive analysis of our Monte Carlo simulation data that the effective scaling exponent $\hat{\zeta}$ which can be extracted from the density auto-correlations indeed appears to take any value in the allowed range, depending on the simulation domain's aspect ratio a and total system length $L_\parallel$, as demonstrated in Fig. 2.10(a), with the critical KLS value $\hat{\zeta} \rightarrow 1/2$ as $a \rightarrow 0$, whereas the two-dimensional (T)ASEP scaling is approached for $a \rightarrow 1$. Interestingly, our simulation data appear to correctly capture the subtle logarithmic corrections in this limit. Furthermore we observe that upon increasing the system length $L_\parallel$, the auto-correlation decay slows down, presumably owing to increasing influence of the critical fluctuations in the cooler subsystem. In the thermodynamic limit, perhaps the universal critical KLS decay exponent $\zeta = 1/2$ might be reached, but likely only after a prohibitively long crossover period.

Upon varying the system parameters, we have discovered that the effective auto-correlation decay exponent $\hat{\zeta}$ appears to be controlled by the mean steady-state particle current $\langle J_{\parallel, st} \rangle$ in the system. To demonstrate that, we plot the auto-correlation function in Fig. 2.10(b) for

a few systems with different lengths $L_\parallel$, keeping the hot-to-critical subsystem ratio constant. As we showed in Fig. 2.6, $\langle J_{\parallel,st} \rangle$ decreases with the system's length if the other parameters remain unchanged; in addition, as the mean steady-state current in the system decreases, so does the auto-correlation decay slope. However, as depicted in the inset of Fig. 2.10(b), two different system geometries that share the same value of the mean steady-state current yield overlapping auto-correlation curves.

2.6   Conclusion

As we have elucidated above, the intriguing stationary-state as well as transient kinetics of non-equilibrium systems displaying generic scale invariance may become even more complex upon combining different models subject to distinct microscopic dynamical rules. In this work, we have shown that a spatially inhomogeneous KLS driven lattice gas with temperature interfaces generated perpendicular to the non-equilibrium drive and net particle current produces spatial patterns similar to those observed in TASEP systems with open boundaries. When part of the lattice is maintained at the critical temperature for phase ordering, while the other subsystem is held at a temperature above T_c, a transport blockage is triggered at the interfaces where particles try to leave the hot subsystem and enter the critical region. As a result, the hot subsystem experiences phase separation, which destroys generic scale invariance in that region. Near the temperature interface, the critical region displays algebraic density decay. The strong critical correlations across the entire system moreover induce marked corrections to the detailed shape of the density profile and in the high-temperature region as well as on the dynamics of the interface fluctuations, which appear to be controlled solely by the value of the stationary-state current.

Chapter 3

Parallel Temperature Interfaces in the KLS Driven Lattice Gas

The following chapter was adapted with minor modifications, with permission from Journal of Statistical Mechanics: Theory and Experiment, from our publication:

*R. I. Mukhamadiarov, Priyanka, and Uwe C. Täuber. Parallel temperature interfaces in the Katz-Lebowitz-Spohn driven lattice gas. Journal of Statistical Mechanics: Theory and Experiment **2020**, 113207 (2020). © SISSA Medialab Srl. Reproduced with permission. All rights reserved*

My main scientific contributions to this publication were developing the simulation code for the two-temperature Katz-Lebowitz-Spohn driven lattice gas, and performing an extensive analysis of the data that I obtained from running simulations. I also wrote the first draft of the manuscript and made all figures.

3.1   Introduction

In recent years a new interesting research avenue has emerged in non-equilibrium statistical physics, namely studies of collective responses in spatially inhomogeneous systems. Whereas substantial progress has been made in understanding the origins and the often universal

nature of cooperative behavior in systems far from equilibrium, it is still unclear whether it is possible to control their global collective stochastic dynamics through local manipulation of a finite spatial patch. Therefore, a comprehensive characterization of spatially inhomogeneous non-equilibrium systems is required. To address this intriguing set of issues, we have chosen the Katz–Lebowitz–Spohn (KLS) driven lattice gas [27, 40–42, 53, 84], a non-equilibrium model where particles perform biased diffusion with site exclusion on a lattice, and in addition experience attractive short-range Ising interactions.

Interestingly, the KLS model falls into two distinct universality classes and hence displays very different scaling behavior depending on whether the temperature of the system that mediates the effectiveness of the ferromagnetic interactions is set above, or exactly at its critical value T_c; and yet other dynamics in the low-temperature, ordered phase. The presence of these diverse types of collective motion in the same system renders the KLS driven lattice gas an excellent candidate for investigating the feasibility of controlling, through local perturbations, the universal behavior of non-equilibrium systems. We approach this problem by introducing a hybrid variant of the KLS model, where two separate sectors of the lattice are maintained at the critical and a higher temperature, respectively, and we investigate the resulting competition between the two distinct scale-invariant dynamics by analyzing the temporal evolution of this two-temperature KLS model. We probe the properties of the resulting temperature interfaces, and their influence on the bulk scaling features of each subsystem.

To our knowledge no attempts have been taken to investigate the possibility of manipulating a non-equilibrium system's scale-invariant dynamics by means of local perturbations of some external control parameter, i.e., by introducing spatial inhomogeneities. In fact, only a few earlier studies have explored the possibility of exerting control on dynamical properties of non-equilibrium systems by globally varying the relevant control parameters [85–88]. On the

other hand, several investigations of hybrid two-temperature Ising models can be found in the literature [59, 60, 89]. Some of these considered the situation when the coupling of the two temperature reservoirs to different parts of the lattice breaks detailed balance, driving the system away from thermal equilibrium [61, 62, 90]; in contrast, setting up spatially inhomogeneous couplings in the Hamiltonian preserves detailed balance and hence fundamentally maintains equilibrium.

In our previous work, we studied a competition between the critical KLS and the (totally) asymmetric exclusion process (T)ASEP scale-invariant dynamics [42, 75, 80] by considering a variation of the KLS driven lattice gas where the entire domain was split into two regions, each coupled to different temperature reservoirs, and with the temperature boundaries oriented perpendicular to the external particle drive [33]. We demonstrated that the cooler region serves as an effective transport bottleneck, impeding particle motion along the drive, and remarkably triggering a phase separation in the hotter subsystem. We also showed that when both temperatures exceed the critical temperature, the resulting density profile is well-described by the mean-field expressions derived for a (T)ASEP with open boundaries [9, 38, 69, 70]. Yet if the temperature of the colder subsystem is maintained exactly at the critical value, one observes enhanced fluctuations, governed by the critical KLS scale-invariant dynamics.

Interestingly, the physics of the alternative geometrical arrangement for a two-temperature KLS model variant, namely where the temperature boundaries are oriented parallel to the external particle drive, appears to be very different. Indeed, in this Chapter we demonstrate that if the rates across the temperature boundaries are chosen to preserve the Ising Z_2 or particle-hole symmetry, the system remains (statistically) homogeneous, in the sense that no (mean) density gradients or sharp kinks arise. However, the particle current still differs in the hotter and cooler subsystems; this transport inhomogeneity alters particle motion at the

subsystem boundaries, producing a flow vector diagram that is reminiscent of a vortex sheet that spans the entire interface, after the net average particle current value is subtracted at every lattice point. In a quest of searching for the signatures of persisting scale-invariant dynamics, we calculate the particle density fluctuations in both subsystems, and find that the fluctuation curves scale with the KLS critical exponents when $T_{\text{hot}} \gg T_c$ and $T_{\text{cold}} = T_c$; but in contrast they scale with the (T)ASEP scaling exponents when both $T_{\text{hot}}, T_{\text{cold}} \gg T_c$.

A system's entropy production rate too is sensitive to cooperative fluctuations during stationarity as well as transients, and has been widely used to characterize non-equilibrium features through quantifying the associated probability fluxes [91]. The external field in the KLS model that sets up a non-vanishing particle current necessarily induces entropy production. Calculating the entropy production rate per volume in our two subsystems separately, we observe a power-law decay in the critical subsystem that is governed by a decay exponent compatible with the corresponding value recorded for the single-temperature KLS at T_c. Indeed, we argue that asymptotically this temporal scaling is identical to that of the density autocorrelation function. Hence we conclude that critical fluctuations dominate the two-temperature KLS dynamics, if the subsystem temperatures are set to $T_{\text{hot}} \gg T_c$ and $T_{\text{cold}} = T_c$.

A yet completely different scenario emerges when the hopping rates across the temperature interfaces explicitly violate particle-hole symmetry. In that perhaps more artificial situation, the system experiences a net particle flux from one subsystem to the other, which eventually leads to density phase separation that ultimately terminates in a dynamically frozen state as the particles become clogged near the subsystem boundaries.

The outline of this Chapter is as follows: In Sec. 3.2 we introduce the two-temperature modification of the KLS model with the parallel temperature interfaces oriented along the drive direction. In Sec. 3.3 we present our results for the case when the hopping rates across

the temperature boundaries are chosen to be Z_2 particle-hole symmetric. In Sec. 3.4, we describe the consequences of choosing the hopping rates across the temperature boundaries such that particle-hole symmetry is manifestly broken. We conclude this Chapter with a summary and brief discussions in Sec. 3.5.

3.2   Two-temperature KLS model

The two-temperature KLS model variant that we study in this Chapter consists of an $L_\parallel \times L_\perp$ rectangular square lattice with periodic boundary conditions, where the hotter and the cooler parts of the lattice are separated by two horizontal temperature interfaces that are oriented parallel to the drive: one placed at zero (or $L_\perp$) and the other at $aL_\perp$, with aspect ratio $a \in (0;1)$, as displayed in Fig. 3.1. In this schematic representation of the two-temperature KLS model, the lower part of the lattice $y \in [0, aL_\perp)$ is maintained at the critical temperature $T_{\mathrm{cold}} = T_c$, whereas the temperature in the upper part $y \in [aL_\perp, L_\perp)$ is set at $T_{\mathrm{hot}} > T_c$. In this Chapter the subsystem size ratio is chosen to be $1 : 1$, which corresponds to $a = 0.5$. We shall refer to the KLS region at $T_{\mathrm{cold}} = T_c$ as the "*critical*" subsystem, and to the region at $T_{\mathrm{hot}} > T_c$ as the "*hot*" or alternatively the "*TASEP-like*" subsystem. We will also refer to the single-temperature KLS driven lattice gas as the "*standard*" KLS model.

We employ the standard Metropolis algorithm with conserved Kawasaki exchange dynamics to simulate the evolution of the two-temperature driven KLS lattice gas on a square lattice with periodic boundary conditions. The simulation is initiated with $N = \frac{1}{2}L_\parallel L_\perp$ particles being randomly distributed over the lattice, and proceeds with random sequential Monte Carlo updates. In our simulations we set the total particle density to $\rho = \frac{1}{2}$ to access the KLS critical point in the critical subsystem, and to avoid triggering kinetic density waves in the hot subsystem. Also, to speed up the simulation time that it takes for the system to

(a)

(b)
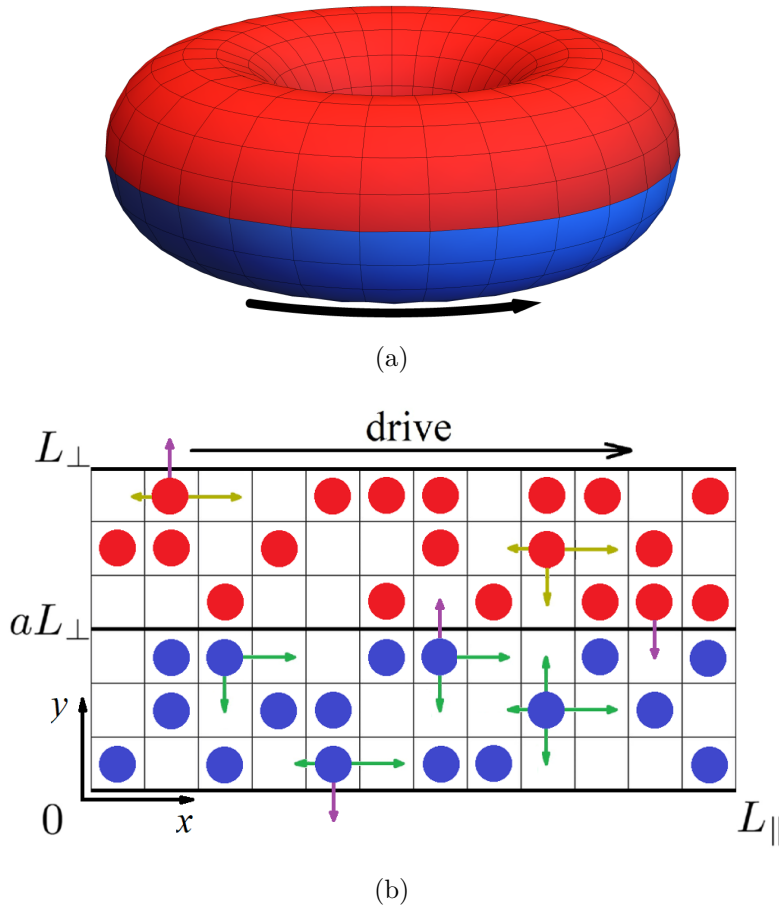
Figure 3.1: (a) The two-temperature driven KLS lattice gas on a ring torus. The red sector of the torus is coupled to a reservoir at temperature $T_{\text{hot}} > T_c$, while the blue sector is coupled to a reservoir at the critical temperature $T_{\text{cold}} = T_c$. The black arrow indicates the direction of the external particle drive. (b) The two-temperature driven KLS lattice gas on an equivalent two-dimensional square lattice with periodic boundary conditions. The $[0, aL_\perp)$ region of the lattice (with blue-colored particles) is maintained at $T_{\text{cold}} = T_c$, while the complement of the lattice is held at $T_{\text{hot}} > T_c$. The colored arrows indicate possible hopping processes, with Metropolis rates given by Eq. 2.2 for hops that happen within the subsystems, and by Eq. 3.1 [or Eq. 3.7] for hops across the temperature interfaces.

reach its non-equilibrium steady state, we choose the particle drive strength to be (formally) $E = \infty$. A more detailed description of the algorithm can be found in the previous chapter [33].

Eq. 2.2 prescribes the hopping rates in the bulk of each subsystem. However, one has

to decide how to handle particle hops across the temperature interfaces. We impose the constraints that this choice should preserve (i) detailed balance in order to not trigger net particle currents between the subsystems, and (ii) the fundamental KLS particle-hole or Ising Z_2 symmetry; therefore it must account for the nearest-neighbor ferromagnetic interactions, too. As we demonstrate in Sec. 3.5, violating the detailed-balance condition by breaking the particle-hole or Ising Z_2 symmetry produces a net particle flux across both temperature boundaries. Thus, it is paramount for our study to choose a proper mathematical form for the interface hopping rates that couple the two distinct temperature regions. Considering the two aforementioned properties, we propose the following particle-hole symmetric rate prescription for hops across the temperature interfaces:

$$W(\mathcal{C} \to \mathcal{C}'; T_1 \to T_2) \propto \exp\left[-\left(\frac{H^p(\mathcal{C}')}{T_2} + \frac{H^h(\mathcal{C}')}{T_1}\right) + \left(\frac{H^p(\mathcal{C})}{T_1} + \frac{H^h(\mathcal{C})}{T_2}\right)\right], \qquad (3.1)$$

where T_1 is the temperature of the subsystem that the particle tries to leave, and T_2 is the temperature of the subsystem that the particle attempts to enter. Here the energy function $H(\mathcal{C})$ from Eq. 2.1 is split into two parts, $H(\mathcal{C}) = H^p(\mathcal{C}) + H^h(\mathcal{C})$, with $H^p(\mathcal{C}, \{n_i = 1\}) = -2J \sum_{\langle i,j \rangle}^{N} \left(n_j - \frac{1}{2}\right)$ representing the part of the energy sum over the occupied (particle) sites' (i) nearest neighbors j, while $H^h(\mathcal{C}, \{n_i = 0\}) = 2J \sum_{\langle i,j \rangle}^{N} \left(n_j - \frac{1}{2}\right)$ is the complementary contribution to the Hamiltonian that extends over the holes' neighbors.

It is straightforward to ascertain that the interface hopping rates (Eq. 3.1) preserve particle-hole (Ising Z_2) symmetry, i.e., upon replacing all particles with holes and vice versa in the configurations of interest, the transition rates from the resulting new configurations $\mathcal{C}$ to $\mathcal{C}'$ will be equal to the original ones: $\sum_{\mathcal{C}} W(\mathcal{C} \to \mathcal{C}'; T_1 \to T_2) = \sum_{\mathcal{C}} W(\mathcal{C} \to \mathcal{C}'; T_2 \to T_1)$. As we show in the following section, this equality ensures that our choice of the hopping rates across the temperature boundaries does not give rise to a net particle current between the two subsystems, which in turn would cause density gradients in the transverse direction.
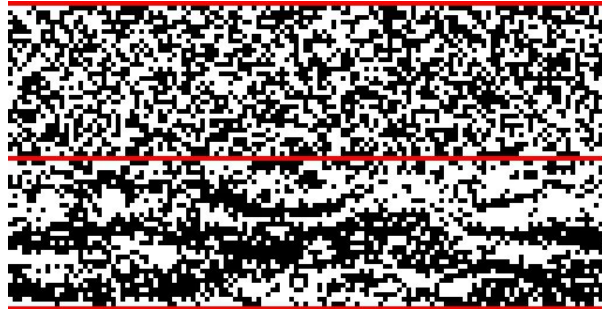
Figure 3.2: Simulation snapshot of the two-temperature KLS driven lattice gas with the temperature boundaries aligned parallel to the drive in its steady state. The system size is $L_\parallel = 128$ and $L_\perp = 64$, with subsystem ratio $1 : 1$ ($a = 0.5$). The red lines at $y = L_\perp/2$ and $y = 0 = L_\perp$ indicate the positions of the temperature interfaces. On this snapshot, the upper part of the lattice is coupled to the $T = 10.0$ temperature reservoir, and the bottom part to the $T = T_c^{128x32} = 0.782$ reservoir.

In Sec. 3.5, we briefly discuss the consequences of selecting interface hopping rates that explicitly violate particle-hole symmetry.

We remark that coupling the lattice to two temperature reservoirs in this manner differs from a situation when the two sectors of the lattice are maintained at the same temperature, but have different interaction strengths J in Eq. 2.1. In the former situation hops across the temperature interface violate detailed balance, while it remains intact in the latter scenario, which represents a spatially inhomogeneous Ising model.

3.3   Simulation results

Running the simulations for the two-temperature KLS model with the particle-hole symmetric hopping rates across the temperature boundaries (Eq. 3.1), we have found that the system remains homogeneous; the average particle density remains $\frac{1}{2}$ along each slice in the transverse direction, and no net particle flux is present perpendicular to the drive. As depicted in the stationary-state snapshot Fig. 3.2, elongated clusters form in the critical subsystem

along the direction of the drive, while the hotter region remains disordered at all times. On first glance the two subsystems seem to evolve as if they are not coupled at all. However, when we checked the initial aging scaling in the two subsystems separately, we found that scaling in each subsystem persists only for a short period of time. After quenching both subsystems from the random initial state to their different assigned temperatures, we measured the two-time autocorrelation function $C(\vec{x} = 0; t, t_w) = \langle n(0, t)n(0, t_w)\rangle - \rho^2$, where $t_w < t$ is often termed waiting time. Using the simple aging scaling form $C(\vec{x} = 0; t, t_w) = t_w^{-\zeta}\hat{C}(t/t_w)$, we looked whether the two-time autocorrelation function in the critical and hot subsystem scaled with the KLS critical exponents and with the (T)ASEP aging scaling exponents, respectively [33, 43, 80]. As over time the dynamical coupling between the subsystems becomes manifest, the simple aging scaling of the two-time autocorrelation function breaks down in both regions, indicating that the mutual interaction between the subsystems alters the scale-invariant dynamics in both temperature regions, similarly to what we observed in the previous chapter in the two-temperature KLS driven lattice gas with transverse temperature boundaries [33].

3.3.1   Current profile

To understand how the subsystems' coupling modifies the dynamics in each temperature region, we first analyzed the current profile of the transverse current in the y direction. Our simulations yield that the transverse particle current remains zero in the bulk of both subsystems, but exhibits spikes at the hot subsystem boundaries, c.f. Fig. 3.3. These perpendicular current peaks originate from the fact that on average the hopping rates in the hot subsystem $\langle W(T_{\text{hot}})\rangle$, Eq. 2.2, exceed the mean hopping rate value across the temperature boundaries $\langle W(T_{\text{hot}} \to T_{\text{cold}})\rangle$, Eq. 3.1. Consequently, particles are likely to be screened from the hot region's boundaries as they approach it. As the difference between the hot subsystem's bulk
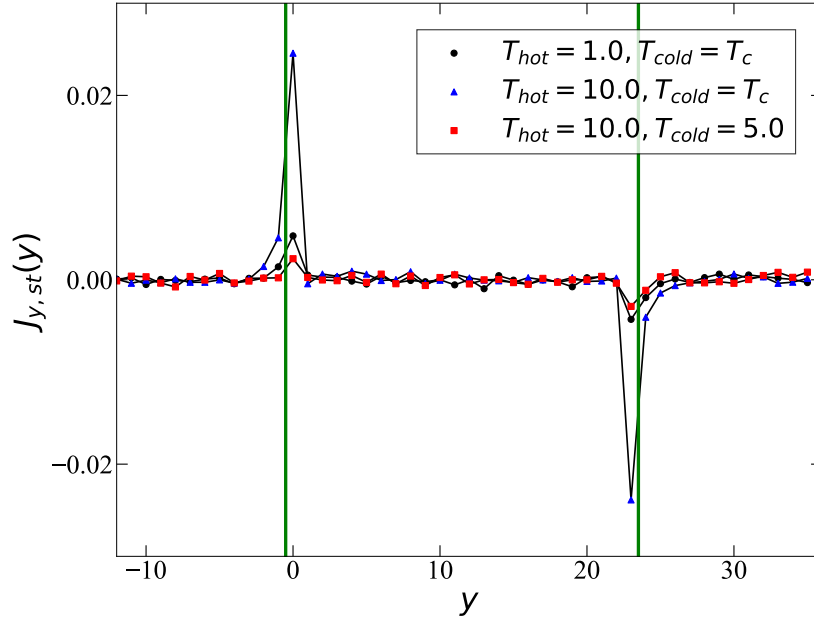
Figure 3.3: The current profile of the two-temperature KLS driven lattice gas with dimensions $L_\parallel = 54$, $L_\perp = 48$ and $1 : 1$ subsystem size ratio for different temperatures of the critical and hot subsystems; the value of the KLS critical temperature for the $54x24$ system is $T_c^{54x24} = 0.773$. The hot subsystem is located in the middle of the graph; the temperature boundaries are indicated by green lines. The data were averaged over $10,000$ independent realizations.

hopping rates and the hopping rates across the temperature interfaces increases, the current peaks at the temperature boundaries become larger and broader, reaching their maximum value for $T_{\text{hot}} = \infty$ and $T_{\text{cold}} = T_c$. (We do not consider temperatures $T < T_c$ in this work).

We have performed a more detailed analysis of the non-trivial structure of the local particle transport in the two-temperature KLS driven lattice gas by studying the current vector field in the hybrid lattice. To render boundary effects more apparent, we subtracted the average net current value from each lattice point and thus obtained the coarse-grained current vector plot shown in Fig. 3.4, where each arrow represents the sum of four current vectors from the adjacent four lattice sites. The resulting current vector patterns for the two-temperature KLS model with parallel temperature interfaces resemble two vortex sheets

(a)   (b)
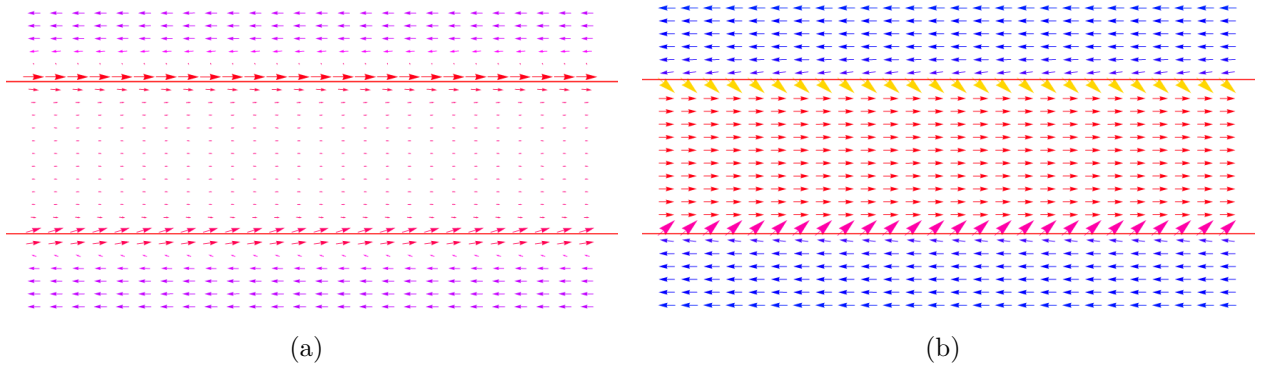
Figure 3.4: The coarse-grained current vector plot for the two-temperature KLS model in the steady state after the average current due to the external particle drive has been subtracted. The temperatures of the subsystems here were chosen as follows: (a) $T_{\text{hot}} = 1.0$, $T_{\text{cold}} = T_c^{54x24} = 0.773$; (b) $T_{\text{hot}} = 10.0$, $T_{\text{cold}} = T_c^{54x24} = 0.773$. The hot temperature region is located in the middle of the plot, with the red lines indicating the positions of the temperature boundaries. The system size is $L_{\parallel} = 54$, $L_{\perp} = 48$, with $1 : 1$ subsystem size ratio. The data were averaged over $10,000$ Monte Carlo steps and $1,000$ independent realizations.

located at the subsystem boundaries that span the entire system. Such vortex sheets are known to appear in fluid-mechanical systems that display velocity discontinuities [92]. In our two-temperature KLS model, this intriguing boundary feature emerges from the parallel particle current difference in both subsystems: The particle current along the drive in the critical subsystem is lower than in the hot region, since the formation of stripe-like clusters in the critical subsystem impedes transport [33]. The strength of these vortex sheets is sensitively controlled by the temperature gradient between the two regions. As is shown in Fig. 3.4(b), when the temperature of the hot subsystem is increased, the strength of the vortex sheet grows accordingly, reaching its maximum for $T_{\text{hot}} \to \infty$ and $T_{\text{cold}} = T_c$, and vanishing when $T_{\text{hot}} = T_{\text{cold}}$, or when both temperatures satisfy $T_{\text{hot}}, T_{\text{cold}} \gg T_c$.

3.3.2   Density fluctuations

Looking for signatures of the scale-invariant dynamics in the two-temperature KLS model, we found that the particle density fluctuations in each subsystem exhibit intriguing non-trivial scaling behavior. While the total number of particles in the entire system of course stays constant, and the average density in each subsystem remains one-half, the hotter and cooler regions may exchange particles, whence the total number of particles in each subsystem fluctuates. We used the following expression to define the integrated particle density fluctuations (per volume) in the entire critical subsystem:

$$
(\Delta\rho(t))^2 = \left\langle \left(\frac{1}{L_\parallel \cdot aL_\perp} \sum_{i,j}^{L_\parallel, aL_\perp} n_{ij}(t) \right)^2 \right\rangle - \left\langle \frac{1}{L_\parallel \cdot aL_\perp} \sum_{i,j}^{L_\parallel, aL_\perp} n_{ij}(t) \right\rangle^2,
\tag{3.2}
$$

where $L_\parallel \cdot aL_\perp$ is the size of the critical subsystem, and the averaging is performed over different, independent simulation runs. To obtain the particle density fluctuations in the hot subsystem, one needs to simply replace $aL_\perp$ everywhere in Eq. 3.2 with $(1-a)L_\perp$.

As is demonstrated in Fig. 3.5, the particle density fluctuations in the critical subsystem follow the scaling form

$$
\left(\Delta\rho(t, L_\parallel, L_\perp) \right)^2 \sim t^{-b} \hat{\varrho} \left(t/L_\parallel^{z_\parallel}, L_\parallel/L_\perp^{1+\Delta} \right),
\tag{3.3}
$$

where z is the dynamical critical exponent and b denotes another scaling exponent, which stems from the density correlations. Finite-size scaling renders Eq. 2.10 into [24]

$$
C\left(\tau, x_\parallel, x_\perp, t, L_\parallel, L_\perp \right) = t^{-\zeta} \; \hat{C} \left(\tau |L_\perp|^{1/\nu}, \frac{x_\parallel}{L_\parallel}, \frac{x_\perp}{L_\perp}, \frac{L_\parallel}{L_\perp^{1+\Delta}}, \frac{t}{L_\parallel^{z_\parallel}} \right),
\tag{3.4}
$$

with $\zeta = (d + \Delta - 2 + \eta)/z = \Delta/z$ in $d = 2$ dimensions. The normalized particle density

(a)

(b)
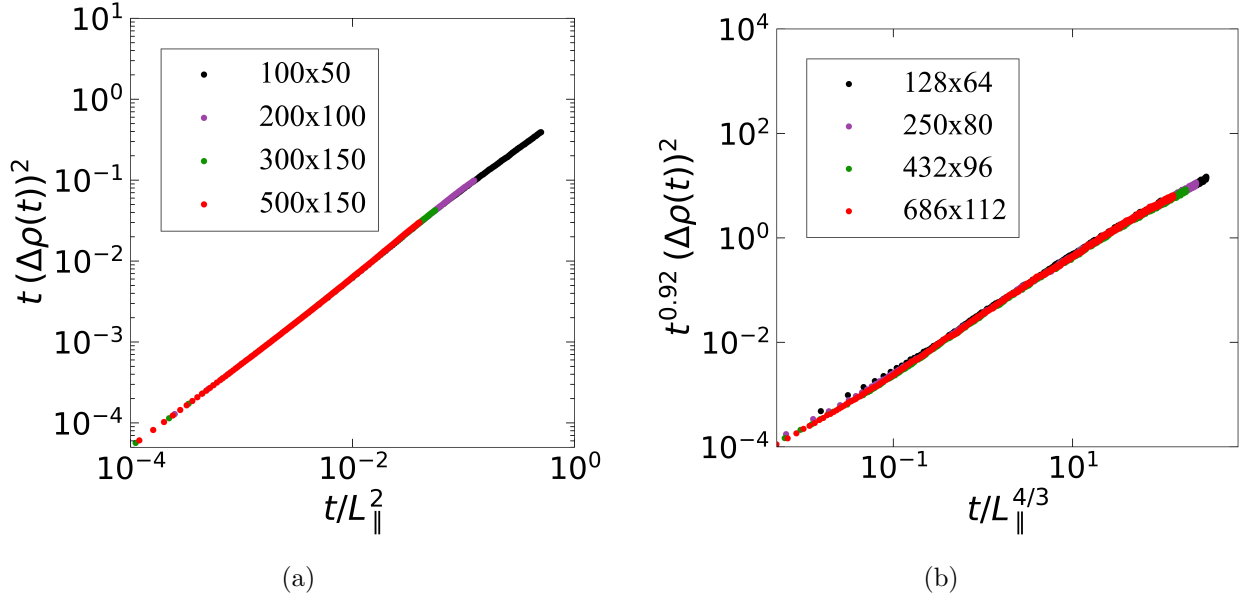
Figure 3.5: Finite-size scaling for the particle density fluctuations in the critical subsystem of the two-temperature KLS driven lattice gas with parallel temperature interfaces. The subsystem temperatures are: (a) $T_{\text{hot}} = 5.0$, $T_{\text{cold}} = 2.0$; (b) $T_{\text{hot}} = 5.0$, $T_{\text{cold}} = T_c$, with $T_c^{128x32} = 0.782$, $T_c^{250x40} = 0.788$, and $T_c^{432x48} = 0.794$. The data were averaged over $2,500$ independent realizations.

fluctuations 3.2 follow directly from the spatial integral of the correlation function; hence we expect in d dimensions

$$\left(\Delta\rho(t, L_{\|})\right)^2 \sim \int C\left(\tau, x_{\|}, x_{\perp}, t, L_{\|}, L_{\perp}\right) dx_{\|} d^{d-1}x_{\perp}/(L_{\perp}^{d-1}L_{\|})^2 \tag{3.5}$$

$$\sim t^{-(2d+2\Delta-2+\eta)/z}\hat{\varrho}(t/L_{\|}^{z\|}, L_{\|}/L_{\perp}^{1+\Delta}) \ ,$$

and thus obtain $b = 2(d - 1 + \Delta + \eta/2)/z = 2(1 + \Delta)/z$ for $d = 2$.

Remarkably, the scaling exponents in Eq. 3.3 appear to change when the temperatures of the subsystems are varied. As shown in Fig. 3.5(a), when both temperatures are set well above T_c, the temporal evolution of the fluctuations satisfies finite-size scaling with exponents $z = 2$ and $b = 1$. Moreover, the dynamical scaling of the particle density fluctuations in this case

does not depend on the choice of the system size aspect ratio $L_\parallel/L_\perp$, suggesting the absense of the manifest anisotropic scaling, i.e., $\Delta = 0$ for $T_{\text{hot}}, T_{\text{cold}} \gg T_c$. Indeed, these are just the (T)ASEP scaling exponents in two dimensions (neglecting logarithmic corrections at its upper critical dimension $d_c = 2$), as listed in Table. 2.1. This exponent match with the finite-size scaling in our data demonstrates that both subsystems of the two-temperature KLS model with parallel temperature interfaces follow the (T)ASEP dynamical scaling behavior when the temperatures T_{hot} and T_{cold} in either region are chosen much higher than the KLS critical temperature T_c, and consequently the attractive ferromagnetic Ising interactions are largely irrelevant.

In contrast, when we choose the subsystems' temperatures as $T_{\text{hot}} \gg T_c$, but $T_{\text{cold}} = T_c$, the particle density fluctuations display very different finite-size scaling behavior. Indeed, the scaling collapse becomes sensitive to the system size aspect ratio, signaling the presence of strong anisotropic scaling. Once we select the appropriate size aspect ratio $L_\parallel/(aL_\perp)^{1+\Delta} = 1/256$ for the critical subsystem with the KLS critical anisotropy exponent $\Delta = 2$ in two dimensions, we observe convincing data scaling collapse for the particle density fluctuations, as evidenced in Fig. 3.5(b) with exponents $z_\parallel = z/(1+\Delta) = 4/3$ and $b \approx 0.92$. While $z = 4$ is indeed equal to the KLS dynamical critical exponent, the collapse exponent deviates from the value $b = 3/2$ predicted by our scaling ansatz. We attribute this discrepancy to strong finite-size corrections characteristic of the critical KLS model, along with the interference of the distinct boundary dynamics, which is prominent for $T_{\text{hot}} \gg T_c$ and $T_{\text{cold}} = T_c$. (We note that the mean-field value for the KLS model, with upper critical dimension $d_c = 5$ and $\Delta = 1$, is $b = 5/2$.) Still, the at least approximate scaling of the particle density fluctuations with the KLS critical exponents indicates the prominence of critical fluctuations in the two-temperature KLS system for the above range of subsystem temperatures, and that in fact these long-range correlations control the hybrid KLS dynamics at least at the system

sizes and time scales our simulations could access. We believe that the critical KLS scaling becomes established in this situation because the transverse particle current is prominent at the subsystem interfaces for those temperature values, and particles are being screened from the temperature boundaries. This leads to an effective (albeit incomplete) decoupling of the hotter and colder regions, allowing the strong KLS fluctuations to build up in the critical subsystem.

3.3.3   Entropy production rate

To reinforce our argument that critical fluctuations are observable in the hybrid two-temperature KLS system when the subsystem temperatures are set to $T_{\text{hot}} \gg T_c$ and $T_{\text{cold}} = T_c$, we have measured the entropy production rate in both subsystems. The non-negative entropy production rate per volume is defined on the two-dimensional lattice as [93]

$$\sigma(t) = \frac{1}{2L_{\parallel}L_{\perp}} \sum_{\mathcal{C},\mathcal{C}'} \sum_{i,j}^{L_{\parallel},L_{\perp}} [P_{ij}(\mathcal{C},t)W_{ij}(\mathcal{C} \to \mathcal{C}',t) - P_{ij}(\mathcal{C}',t)W_{ij}(\mathcal{C}' \to \mathcal{C},t)]$$
$$\times \ln \frac{P_{ij}(\mathcal{C},t)W_{ij}(\mathcal{C} \to \mathcal{C}',t)}{P_{ij}(\mathcal{C}',t)W_{ij}(\mathcal{C}' \to \mathcal{C},t)} \geq 0 \ , \tag{3.6}$$

where the sum extends over all 2^6 possible nearest-neighbor configurations of any selected site pair chosen for particle-hole exchange. We compute this quantity in our simulations by obtaining the probability $P_{ij}(\mathcal{C},t)$ of each configuration to occur at each lattice site at time t. The logarithm factor in Eq. 3.6 prohibits us from computing the entropy production rate with infinite drive strength, as it sets the hopping rate against the drive to zero. Thus, to obtain the entropy production rate we set the drive strength to a very large, but finite value $E = 100$.

Calculating the entropy production rates for the hotter and cooler subsystems separately, we
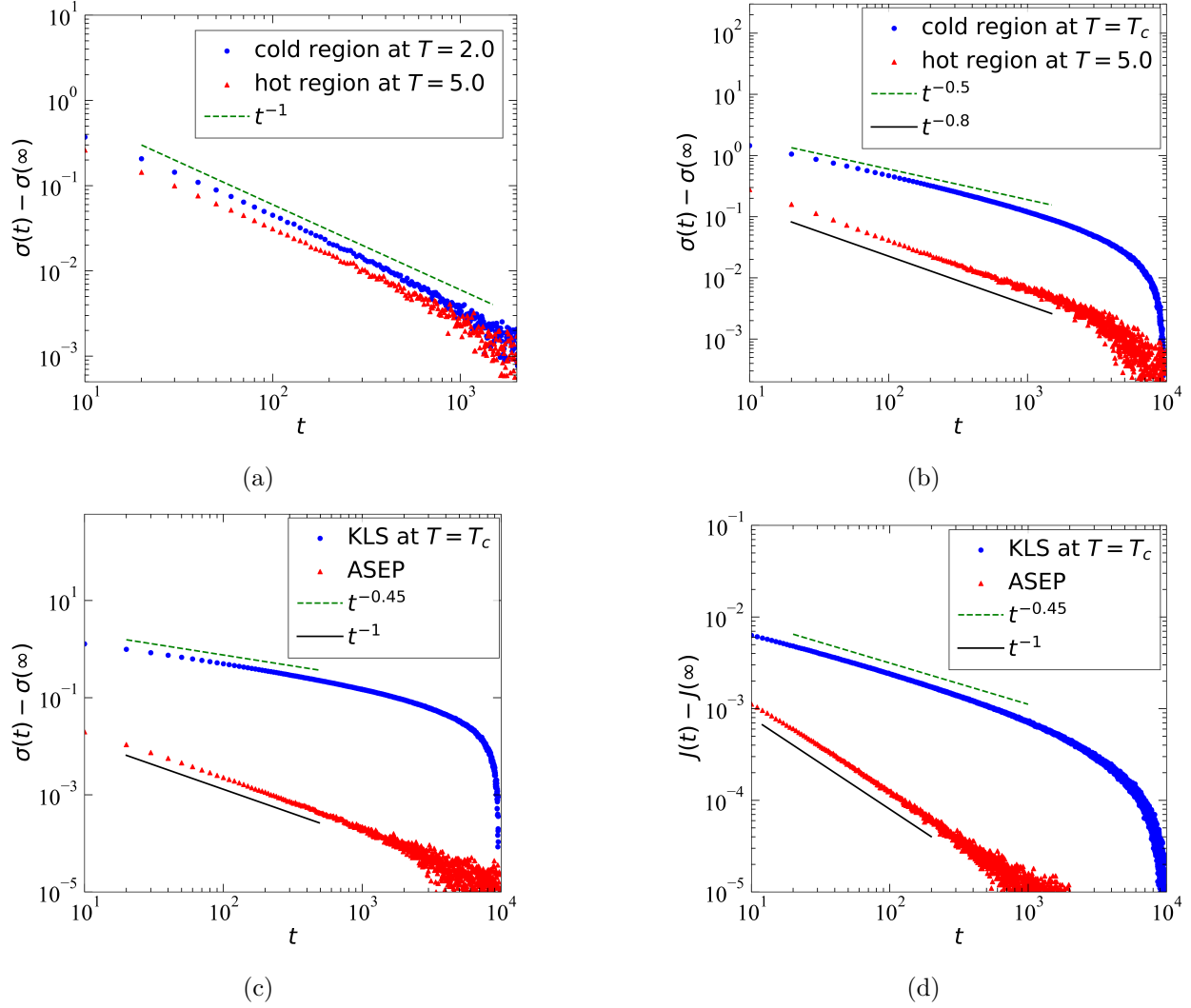
Figure 3.6: (a) The entropy production rate per volume in the two-temperature KLS driven lattice gas with parallel temperature interface in both subsystems for $T_{\text{hot}} = 5.0$ and $T_{\text{cold}} = 2.0$ after the saturation value $\sigma(\infty)$ has been subtracted. (b) The entropy production rate per volume in both temperature regions for $T_{\text{hot}} = 5.0$ and $T_{\text{cold}} = T_c^{250x40} = 0.788$ after the saturation value $\sigma(\infty)$ has been subtracted. (c) The entropy production rate per volume and (d) net particle current in the standard critical KLS model at $T = T_c^{250x40} = 0.788$ and in the ASEP after the saturation values $\sigma(\infty)$ and $J(\infty)$ have been subtracted. The system dimensions are: $L_\parallel = 250$, $L_\perp = 80$ with $1:1$ subsystem ratio for both (a) and (b); $L_\parallel = 250$, $L_\perp = 40$ for the standard KLS model, and $L_\parallel = L_\perp = 250$ for the ASEP in (c), (d). The drive strength is chosen to be $E = 100$. The ASEP hopping rate along the drive is set to $p_\parallel = 0.999$, and in the opposite direction $q_\parallel = 1 - p_\parallel = 0.001$. All data were averaged over $100,000$ independent realizations.

found that they quickly decay to steady-state values after we quench the system from random initial conditions or infinite temperature to $T_{\text{hot}}, T_{\text{cold}}$, subsequently holding the temperatures constant at $T_{\text{hot}}, T_{\text{cold}} \gg T_c$. Since the density correlations in this (T)ASEP temperature regime are very short-ranged, one would indeed expect this fast relaxation from a generic initial configuration to a low-level, external noise-driven stationary entropy production rate. However, if we initiate our simulations with highly correlated "checkerboard" configurations with alternating filled and empty sites, a state that is quite distinct from any generic TASEP configuration [80], then the entropy production rate decays according to a power law $\sim t^{-1}$ in both subsystems for $T_{\text{hot}}, T_{\text{cold}} \gg T_c$, as shown in Fig. 3.6(a). Yet when the temperature in the colder region is maintained exactly at the critical value $T_{\text{cold}} = T_c$, we observe a slower algebraic decay of the entropy production rate with decay exponent ≈ 0.5 in the critical subsystem, and decay exponent ≈ 0.8 in the hotter subsystem, as depicted in Fig. 3.6(b), followed by a finite-size exponential cut-off.

To address the question whether the power-law decay of the entropy production rate in the critical subsystem is dominated by the KLS critical fluctuations, and to better grasp how the hotter subsystem's dynamics affects the non-equilibrium relaxation of the critical subsystem to its steady state, we measured the entropy production in the standard, homogeneous two-dimensional KLS and ASEP models, with biased hopping rates along and against the drive set to $p_\parallel = 0.999$ and $q_\parallel = 1 - p_\parallel = 0.001$, respectively. To access the nontrivial relaxational regime in the ASEP, we prepared the system again in a unique correlated initial state, placing the particles with alternating occupation on the lattice in a checkerboard fashion [80]. As shown in Fig. 3.6(c), the power law for the entropy production rate in the critical subsystem follows very closely the analogous algebraic decay for the standard KLS model at criticality, indicating that critical fluctuations persist in the KLS system, even when it is being coupled to a region with hotter temperature $T_{\text{hot}} > T_c$. Similarly, if both subsystem temperatures

are set well above T_c, the entropy production rate decays with the ASEP exponent, as one would expect in the KLS high-temperature phase.

From our simulations it is evident that these nontrivial power-law decay exponents must fall into the respective critical KLS and TASEP universality classes. The expression for the entropy production rate in Eq. 3.6 clearly suggests that its temporal evolution should be closely tied to the non-equilibrium relaxation of the net particle current following the quench. In the absence of the external drive, the entropy production stems from the change in the system's energy, due to its coupling with its surroundings [94, 95]. Yet for the driven lattice gases under consideration here, $\sigma(t)$ is dominated by the change of the entropy within the system, which in turn equals the drive strength multiplied with the mean current in the system [94]. This connection between the entropy production rate and the average current is confirmed nicely in our simulation data through the match of the corresponding decay exponents. We show in Fig. 3.6(d) that as the mean particle current and the entropy production rate approach their steady state values, the power laws for the average particle current difference $j(t) - j(\infty)$ and for the entropy production rate difference $\sigma(t) - \sigma(\infty)$ are indeed characterized by the same decay exponents, for both the ASEP and KLS models.

Furthermore, the origin of these decay exponents becomes apparent once we relate the entropy production rate with the nearest-neighbor equal-time correlation function. One can see how these two quantities are connected after expanding the exponential factor in the Kawasaki exchange rates in Eq. 2.2 for $E = 0$: From the Ising Hamiltonian 2.1 it is clear that the transition rate difference $W_{ij}(\mathcal{C} \to \mathcal{C}', t) - W_{ij}(\mathcal{C}' \to \mathcal{C}, t)$ will thus become to leading order proportional to the nearest-neighbor equal-time correlation function. This makes sense, since the entropy production rate originates from the temporal changes in the system's energy, which is here characterized by the nearest-neighbor equal-time correlation function in the thermodynamic limit. Indeed, a similar connection between the entropy production

rate and the rate of free energy change has been established previously for non-driven Ising spin systems [95]. Consequently, we posit that the ASEP and KLS entropy production power laws observed in Fig. 3.6(c) are determined by the temporal scaling of the nearest-neighbor equal-time correlation function, i.e., $\sigma(\infty) - \sigma(t) \sim t^{-\zeta}$, where ζ is just the decay exponent from Eq. 3.4.

3.4 Interface hopping rates with broken particle-hole symmetry

To satisfy our curiosity, we have considered another (simpler) choice for the hopping rates across the temperature interfaces that explicitly violates particle-hole symmetry, namely:

$$W(\mathcal{C} \to \mathcal{C}'; T_1 \to T_2) \propto \exp\left[-\left(\frac{H(\mathcal{C}')}{T_2} - \frac{H(\mathcal{C})}{T_1}\right)\right], \tag{3.7}$$

where $H(\mathcal{C})$ and $H(\mathcal{C}')$ are the energy functions from Eq. 2.1, T_1 is the temperature of the subsystem that a *particle* tries to leave, and T_2 is the temperature of the subsystem that this particle attempts to enter.

In the rate prescription Eq. 3.7, the temperature values T_1 and T_2 depend on the initial and the final positions of the particle that tries to cross the temperature boundary. This choice manifestly breaks particle-hole symmetry and, as a result, induces a net flow of particles across the temperature interfaces into the hotter region. This counterintuitive outcome simply stems from the form of the hopping rates across the temperature boundaries Eq. 3.7, which makes it easier for particles to exit the critical subsystem rather than to enter it, leading to a transport bias into the hotter region. As shown in Fig. 3.7, the particle excess in the hotter subsystem exhibits an intriguing power-law growth with an exponent that depends
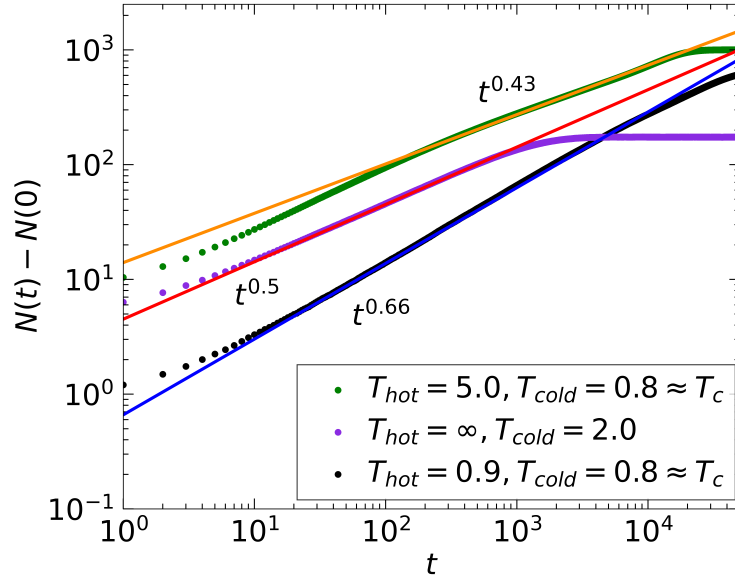
Figure 3.7: Net particle growth in the hot subsystem with time for different subsystem temperatures in the two-temperature KLS model with hopping rates across the temperature boundaries that manifestly break particle-hole (Ising Z_2) symmetry. The system size is $L_\parallel = 128$, $L_\perp = 64$, with $1:1$ subsystem size ratio. The data were averaged over $10,000$ independent realizations.

on both regions' temperatures: We observe slower growth with a smaller exponent value for $T_{\mathrm{cold}} = T_c$ and $T_{\mathrm{hot}} \gg T_c$, indicating that the particle exchange between the subsystems is hindered for these temperatures. When both temperatures are set well above T_c, the motion in the transverse direction is purely diffusive and hence the power-law growth exponent is $1/2$, directly related to the transverse mean-square particle displacement. We cannot offer insights why we measure a $t^{2/3}$ algebraic growth if both $T_{\mathrm{hot}}, T_{\mathrm{cold}} \gg T_c$.

We had initially surmised that this growth exponent might reflect a universal (T)ASEP feature, but had to discard that notion after observing distinct growth exponents for other Z_2 symmetry-breaking forms of the interface hopping rates. In fact, we have found that the growth exponent can take any value in the interval $[0.4 : 0.83]$, depending on the definition of the hopping rates across the temperature boundaries and both regions' temperatures.

(a)   (b)
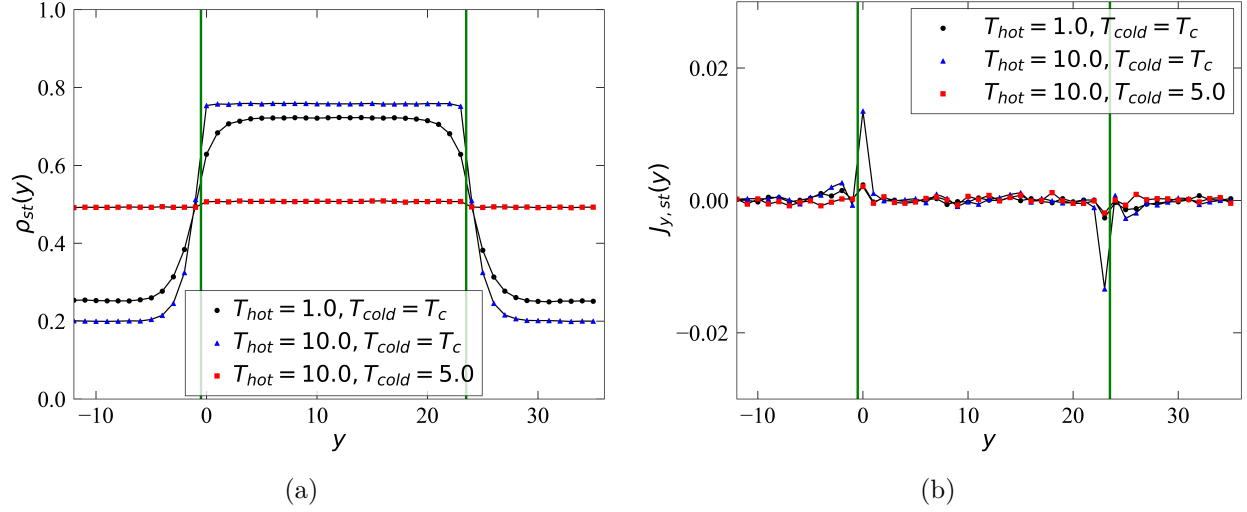
Figure 3.8:   (a) The density and (b) current profiles of the two-temperature KLS driven lattice gas with parallel temperature interfaces for different subsystem temperatures T_{hot} and T_{cold}. The lattice dimensions are $L_\parallel = 54$, $L_\perp = 48$, with subsystem size ratio $1 : 1$; the temperature interface boundaries are indicated by the green lines. The hotter temperature subsystem is located in the center on these plots. The data were averaged over $10,000$ independent realizations.

Once the particle number growth in the hotter subsystem shown in Fig. 3.7 ceases, we presume the two-temperature KLS driven lattice gas to have reached its non-equilibrium steady state. The resulting steady-state density profile demonstrates that the hopping rates across the temperature boundaries that break particle-hole symmetry trigger a phase separation in the particle density; the initially homogeneous system splits into a high-density region in the hot subsystem, and a low-density region in the critical subsystem, with sharp density kinks located at the temperature interfaces. As depicted in Fig. 3.8(a), the height of the density kinks grows as the transverse current at the temperature boundaries increases (Fig. 3.8(b)). We remark that finite-size effects are likely significant in this clogged stationary state, where mutual exclusion at the interfaces ultimately terminates the further dynamical evolution of the system.

Similarly to the particle-hole symmetric case, the density kink height increases with the

(a)

(b)
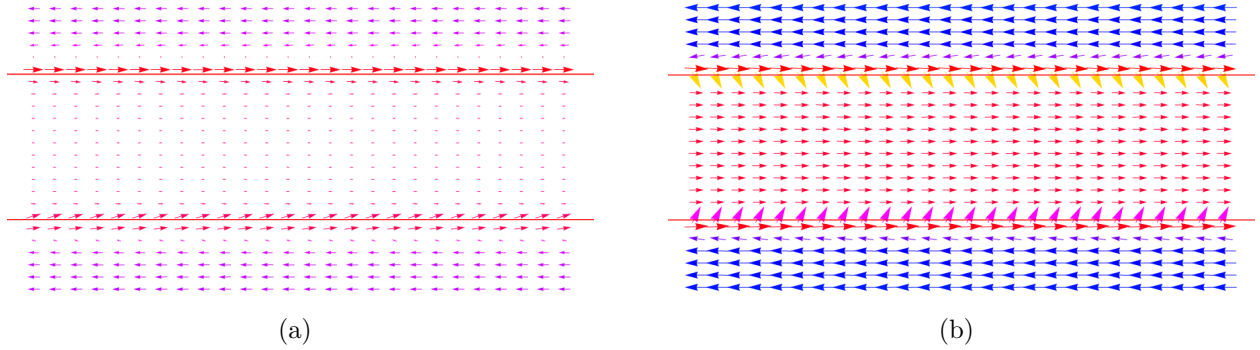
Figure 3.9: The coarse-grained current vector plots for the two-temperature KLS in the steady state after the net current has been subtracted from each lattice point. The subsystem temperatures are set at: (a) $T_{\mathrm{hot}} = 1.0$, $T_{\mathrm{cold}} = T_c^{54 \times 24} = 0.773$; (b) $T_{\mathrm{hot}} = 5.0$, $T_{\mathrm{cold}} = T_c^{54 \times 24} = 0.773$. The system size is $L_{\parallel} = 54$, $L_{\perp} = 48$, with the hot temperature subsystem located in the center of the plots; the red lines indicate the positions of the temperature boundaries. The data were averaged over $28,000$ Monte Carlo steps and over $10,000$ independent realizations.

difference between the mean bulk hopping rate from Eq. 2.2 at T_2 and the average hopping rate across the interface given now by Eq. 3.7. However, in contrast to the symmetric rate choice, a second minor peak is visible in Fig. 3.8(b) right outside of the hotter region, signaling the presence of particle blockages at the interfaces. A signature of ensuing particle clogging at the temperature boundaries can be also seen in the current vector plot in Fig. 3.9, where near the interfaces, just outside of the hotter subsystem, no significant transverse current is discernible, indicating limited particle influx into the hot region. As for particle-hole symmetric hopping rates, boundary effects become amplified when the difference between the mean hopping rates approaches its maximum value, i.e., when the subsystem temperatures are set to their extreme limits $T_{\mathrm{hot}} \to \infty$ and $T_{\mathrm{cold}} = T_c$.

3.5   Conclusion

In this work we have numerically studied a two-temperature KLS driven lattice gas, with the temperature interfaces aligned along the external drive direction. We have demonstrated that it is possible to control the scale-invariant dynamics in the system by changing the temperature(s) locally, i.e., by adjusting the strength of the vortex sheets at the temperature boundaries. In contrast to our previous work, where splitting the lattice into two temperature regions with transverse temperature boundaries induced a density phase separation in the hotter subsystem, here we observe that orienting the interfaces parallel to the drive and net current maintains homogeneity in each subsystem and preserves its scale-invariant dynamics.

Even though the formation of the boundary-induced vortex sheets terminates the subsystems' independent initial aging kinetics, their coupling through particle exchange across the interfaces allows us to observe interesting finite-size scaling for the resulting particle density fluctuations. We have shown that for two distinct temperature regimes, namely for $T_{\text{hot}}, T_{\text{cold}} \gg T_c$ and $T_{\text{hot}} \gg T_c, T_{\text{cold}} = T_c$, these particle density fluctuations scale with the (T)ASEP and critical KLS dynamical scaling exponents, respectively. Moreover, in the latter case we have observed the power-law decay exponent of the entropy production rate in the critical subsystem to be very close to the corresponding value measured for the standard critical KLS model, which in turn is asymptotically governed by the scaling of the density autocorrelation function. Although we have gathered substantial evidence that the dynamics of the critical subsystem is governed by the KLS critical exponents, we cannot completely exclude the possibility that for the latter temperature choice, the system might be arrested in an exceedingly slow crossover regime, that critical fluctuations will eventually terminate, and that the system will ultimately display TASEP scaling behavior.

Chapter 4

Social distancing and epidemic resurgence in agent-based SIR models

The following chapter was adapted with minor modifications, with permission from Scientific Reports, from our publication:

*R. I. Mukhamadiarov, S. Deng, S. R. Serrao, Priyanka, R. Nandi, L. H. Yao, U. C. Täuber, Social distancing and epidemic resurgence in agent-based Susceptible-Infectious-Recovered models, Scientific Reports **11**, 130 (2021);*

My main scientific contribution to this publication are the lattice simulations of COVID-19 spreading that are based on a stochastic SIR model.

4.1 Introduction

The COVID-19 pandemic constitutes a severe global health crisis. Many countries have implemented stringent non-pharmaceutical control measures that involve behavioral change of the public such as social distancing, using face-coverings and mobility reduction enforced by lockdowns in their populations. This has led to remarkably successful deceleration and significant 'flattening of the curve' of the infection outbreaks, albeit at tremendous economic and financial costs [96, 97]. At this point, societies are in dire need of designing a secure

(partial) exit strategy wherein the inevitable recurrence of the infection among the significant non-immune fraction of the population can be thoroughly monitored with sufficient spatial resolution and reliable statistics, provided that dependable, frequent, and widespread virus testing capabilities are accessible and implemented. Until an effective and safe vaccine is widely available, this would ideally allow the localized implementation of rigorous targeted disease control mechanisms that demonstrably protect people's health while the paralyzed branches of the economy are slowly rebooted.

Mathematical analysis and numerical simulations of infection spreading in generic epidemic models are crucial for testing the efficacy of proposed mitigation measures, and the timing and pace of their gradual secure removal. Specifically, the employed mathematical models need to be (i) stochastic in nature in order to adequately account for randomly occurring or enforced disease extinction in small isolated communities, as well as for rare catastrophic infection boosts and (ii) spatially resolved such that they properly capture the significant emerging correlations among the susceptible and immune subpopulations. These distinguishing features are notably complementary to the more detailed and comprehensive computer models utilized by researchers at the University of Washington, Imperial College London, the Virginia Bioinformatics Institute, and others: see, e.g., [98–103].

We report a series of detailed individual-based Monte Carlo computer simulation studies for stochastic variants [47, 48] of the paradigmatic Susceptible-Infectious-Recovered (SIR) model [45, 46] for a community of about 100,000 individuals. To determine the robustness of our results and compare the influence of different contact characteristics, we ran our stochastic model on four distinct spatially structured architectures, namely i) regular two-dimensional square lattices, wherein individuals move slowly and with limited range, i.e., spread diffusively; ii) two-dimensional small-world networks that in addition incorporate substantial long-distance interactions and contaminations; and finally on iii) random as well

as iv) scale-free social contact networks. For each setup, we investigated epidemic outbreaks with model parameters informed by the known COVID-19 data [101, 104]. To allow for a direct comparison, we extracted the corresponding effective infection and recovery rates by fitting the peak height and the half-peak width of the infection growth curves with the associated classical deterministic SIR rate equations that pertain to a well-mixed setting. We designed appropriate implementations of social distancing and contact reduction measures on each architecture by limiting or removing connections between individuals. This approach allowed us to generically assess the efficacy of non-pharmaceutical control measures.

Although each architecture entails varied implementations of social distancing measures, we find that they all robustly reproduce both the resulting reduced outbreak intensity and growth speed. As anticipated, a dramatic resurgence of the epidemic occurs when mobility and contact restrictions are released too early. Yet if stringent and sufficiently long-lasting social distancing measures are imposed, the disease may go extinct in the majority of isolated small population groups. In our spatially extended lattice systems, disease spreading then becomes confined to the perimeters of a few larger outbreak regions, where it can be effectively localized and specifically targeted. For the small-network architecture, it is however imperative that all long-range connections remain curtailed to a very low percentage for the control measures to remain effective. Intriguingly, we observe that an infection outbreak spreading through a static scale-free network effectively randomizes its connectivity for the remaining susceptible nodes, whence the second wave encounters a very different structure.

In the following sections, we briefly describe the methodology and algorithmic implementations as well as pertinent simulation results for each spatial or network structure; additional details are provided in Section 4.3. We conclude with a comparison of our findings and a summary of their implications.

4.2   Results

4.2.1   Square lattices with diffusive spreading

Our first architecture is a regular two-dimensional square lattice with linear extension $L = 448$ subject to periodic boundary conditions (i.e., on a torus). Initially, $N = S(0) + I(0) + R(0) = 100,000$ individuals with fixed density $\rho = N/L^2 \approx 0.5$ are randomly placed on the lattice, with at most one individual allowed on each site. Almost the entire population begins in the susceptible state $S(0)$; we start with only 0.1% infected individuals, $I(0) = 100$, and no recovered (immune) ones, $R(0) = 0$. We note that in stochastic simulations, random fluctuations often lead to the initial infectious population recovering so fast that the epidemic dies out before it can cause an outbreak; therefore we chose to seed the system with 100 randomly placed infected individuals. This initial configuration is moreover motivated by enforced lockdowns and travel restrictions which essentially stops the external influx of new infections. Subsequently, all individuals may move to neighboring empty lattice sites with diffusion rate d (here we set this hopping probability to 1). Upon their encounter, infectious individuals irreversibly change the state of neighboring susceptible ones with set rate r: $S + I \rightarrow I + I$. Any infected individual spontaneously recovers to an immune state with fixed rate a: $I \rightarrow R$. (Details of the simulation algorithm are presented in Sec. 4.3.) For the recovery period, we choose $1/a \cong 6.667$ days (1 day is equivalent to one Monte Carlo step, MCS) informed by known COVID-19 characteristics [104]. To determine the infection rate r, we run simulations for various values, fit the peak height and width of the ensuing epidemic curves with the corresponding SIR rate equations to extract the associated basic reproduction ratio R_0 (as explained in the Sec. 4.3, see Figure 4.7), and finally select that value for r for our individual-based Monte Carlo simulations that reproduces the $R_0 \approx 2.4$ for COVID-19 [101]. We perform 100 independent simulation runs with these reaction rates, from which

we obtain the averaged time tracks for $I(t)$ and $R(t)$, while of course $S(t) = N - I(t) - R(t)$ and $R(t) = a \int_0^t I(t')dt'$.

The standard classical SIR deterministic rate equations assume a well-mixed population and constitute a mean-field type of approximation wherein stochastic fluctuations and spatial as well as temporal correlations are neglected; see, e.g., [24, 51]. Near the peak of the epidemic outbreak, when many individuals are infected, this description is usually adequate, albeit with coarse-grained 'renormalized' rate parameters that effectively incorporate fluctuation effects at short time and small length scales. However, the mean-field rate equations are qualitatively insufficient when the infectious fraction $I(t)/N$ is small, whence both random number fluctuations and the underlying discreteness and associated internal demographic noise become crucial [24, 50, 51]. Already near the epidemic threshold, which constitutes a continuous dynamical phase transition far from thermal equilibrium, c.f. Figure 4.8 in the Sec. 4.3, the dynamics is dominated by strong critical point fluctuations. These are reflected in characteristic initial power laws rather than simple exponential growth of the $I(t)$ and $R(t)$ curves [105], as demonstrated in Figure 4.7 (Sec. 4.3).

Nor can the deterministic rate equations capture stochastic disease extinction events that may occur at random in regions where the infectious concentration has reached small values locally. The rate equations may be understood to pertain to a static and fully connected network; in contrast, the spreading dynamics on a spatial setting continually rewires any infectious links keeping the epidemic active [103, 106]. Consequently, once the epidemic outbreak threshold is exceeded, the SIR rate equations markedly underestimate the time-integrated outbreak extent reflected in the ultimate saturation level $R_\infty = R(t \to \infty)$, as is apparent in the comparison Figure 4.7 (Sec. 4.3).

Once the instantaneous infectious fraction of the population has reached the threshold 10%, $I(t) = 0.1N$, we initiate stringent social distancing that we implement through a strong

repulsive interaction between any occupied lattice sites (with $n_i = 1$), irrespective of their states S, I, or R; and correspondingly an attractive force between filled and empty ($n_i = 0$) sites, namely the repulsive interaction energy $V(n_i) = K \sum_{<i,j>} (2n_i - 1)(2n_j - 1)$ with dimensionless strength $K = 1$, where the sum extends only over nearest-neighbor pairs on the square lattice. The transfer of any individual from an occupied to an adjacent empty site is subsequently determined through the ensuing energy change ΔV by the Metropolis transition probability $w = \min\{1, \exp(-\Delta V)\}$ which replaces the unmitigated hopping rate d. As a result, both the mobility as well as any direct contact between individuals on the lattice are quickly and drastically reduced. With this social distancing mechanism, our system effectively operates like an adaptive network [107], where all types of links, rather than only the $S - I$ links [108], tend to be dynamically suppressed during the lockdown period. For sufficiently small total density $\rho = N/L^2$, most of the individuals eventually become completely isolated from each other. For our $\rho = 0.5$, the disease will continue to spread for a short period, until the repulsive potential has induced sufficient spatial anti-correlations between the susceptible individuals. The social-distancing interaction is sustained for a time duration T, and then switched off again.

Figure 4.1 depicts two sets of Monte Carlo simulation snapshots, each beginning at the moment when social distancing is switched on. The second column shows the configurations when the repulsive interaction V is turned off again after respectively $T = 2/a$ (top), and $T = 10/a$ (bottom), while the last two sets of snapshots illustrate the subsequent resurgence of the outbreak. With increasing mitigation duration T, the likelihood for the disease to locally go extinct in isolated population clusters grows markedly. As seen in the bottom row, the prevalence and spreading of the infection thus becomes confined to the perimeters of a mere few remaining centers. Hence we observe drastically improved mitigation effects for extended T: As shown in Figure 4.2, the resurgence peak in the $I(t)$ curve assumes markedly
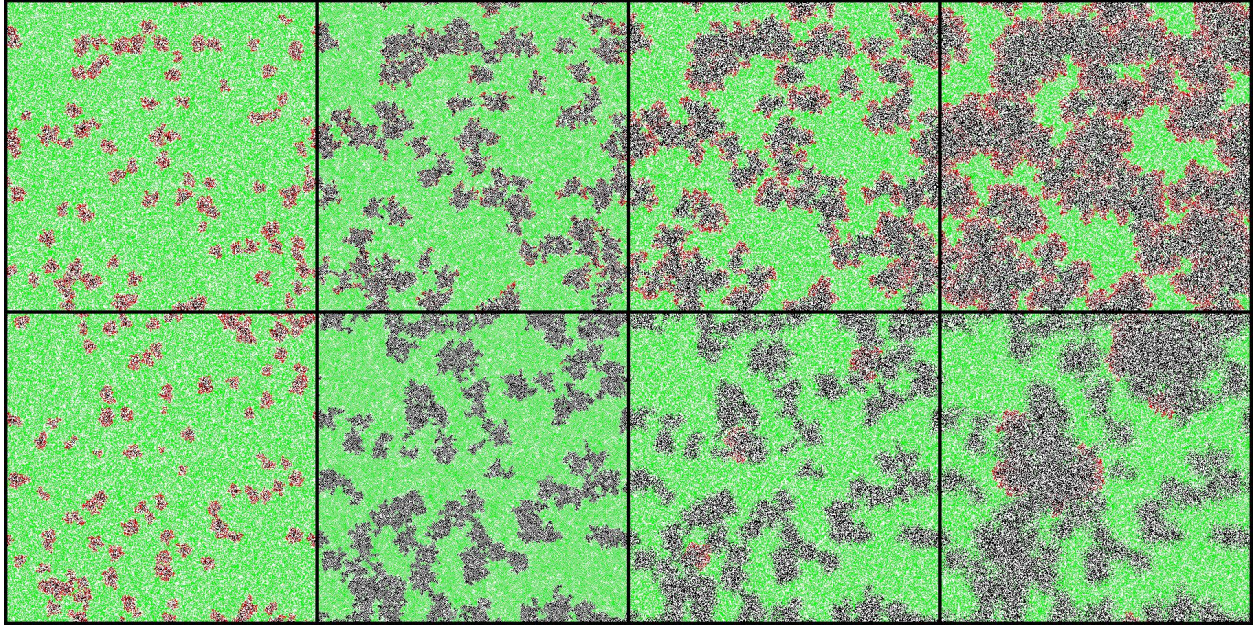
Figure 4.1: Stochastic SIR model simulation snapshots on a square lattice (with periodic boundary conditions). 'Social distancing' is turned on when the number of infective individuals reaches $I(t) = 0.1N$, and subsequently maintained for a duration $T = 22MCS = 2/a$ in the top, and $T = 110MCS = 10/a$ in the bottom row. The green color marker is used for susceptible individuals, while red indicates infected and black recovered (immune or deceased) individuals. The first snapshots (leftmost column) capture the instance when mitigation is implemented. The second column marks the time when social distancing is turned off after additional time T has elapsed. The third and fourth columns show the ensuing spread of the disease. With extended social distancing duration T (bottom row), the infection becomes more likely to be driven to extinction in confined contact regions. Hence the number of active outbreak centers decreases drastically, which could facilitate disease control through effective testing and tracking.

lower values and is reached after much longer times. In fact, the time $\tau(T)$ for the infection outbreak to reach its second maximum increases exponentially with the social-distancing duration, as evidenced in the inset of Figure 4.2 (see also Figure 4.5 below). We emphasize that localized disease extinction and spatial confinement of the prevailing disease clusters represent correlation effects that cannot be captured in the SIR mean-field rate equation description.
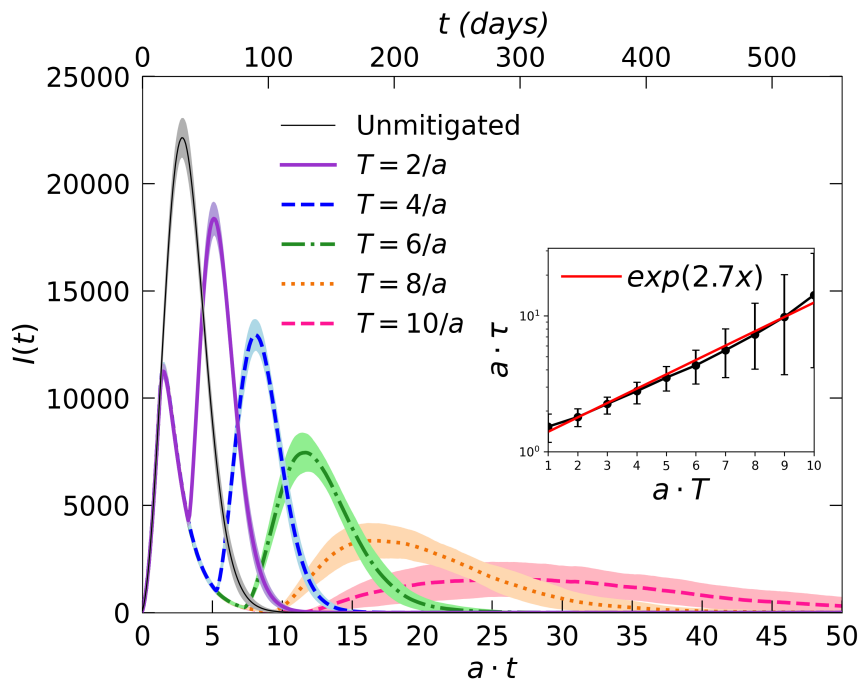
Figure 4.2: Infection curves $I(t)$ for the stochastic SIR model on a square lattice. The graphs compare the outbreak data obtained without any mitigation (grey) and with social distancing measures implemented for different durations T, as indicated. In all cases, social distancing is turned on once $I(t)$ reaches the set threshold of 10% of the total population N. The resurgent outbreak is drastically reduced in both its intensity and growth rate as social distancing is maintained for longer time periods T. (The data for each curve were averaged over 100 independent realizations; the shading indicates statistical error estimates.) Inset: time τ to reach the second peak following the end of the mitigation; the data indicate an exponential increase of τ with T.

4.2.2   Two-dimensional small-world networks

In modern human societies, individuals as well as communities feature long-distance connections that represent "express" routes for infectious disease spreading in addition to short-range links with their immediate neighbors. To represent this situation, we extend our regular lattice with diffusive propagation to a two-dimensional Newman-Watts small-world network [26], which was previously applied to the study of plant disease proliferation [109]. Diffusive propagation is the manifestation of the natural movement of the individuals over

the spatial extent of the lattice. In contrast to the Watts-Strogatz model [110], in which the small-world property is generated through rewiring bonds of a one-dimensional chain of sites, a Newman-Watts small-world network may be constructed as follows: For each nearest-neighbor bond, a long-distance link (or 'short-cut') is added with probability ϕ between randomly chosen pairs of vertices. As illustrated in Figure 4.9 (Sec. 4.3), the resulting network features $2\phi L^2$ long-distance links, with mean coordination number $\langle k \rangle = 4(1 + \phi)$.

Again, each vertex may be in either of the states S, I, R, or empty, and each individual can hop to another unoccupied site along any (nearest-neighbor or long-distance) link with a total diffusion rate d. While network graphs have been widely employed before to represent human social interactions, we emphasize that our approach substantially differs in that we simulate a fully stochastic set of SIR reactions on dynamically changing networks that have an underlying static small-network structure. A typical snapshot of the SIR model on this small-world architecture is shown in Figure 4.9 (Sec. 4.3). The unmitigated simulation parameters are: $L = 1,000$, $N = 100,000$, $I(0) = 100$, $d = 1$, and $\phi = 0.6$. The presence of long-range links increases the mean connectivity, rendering the population more mixed, which in turn significantly facilitates epidemic outbreaks (see Figure 4.10 in Sec. 4.3). We remark that for the SIR dynamics, the Newman-Watts small-world network effectively interpolates between a regular two-dimensional lattice and a scale-free network dominated by massively connected hubs; moreover, as the hopping probability $d \to 0$, the small-world network is effectively rendered static.

In the two-dimensional small-world network, we may introduce social-distancing measures through two distinct means: i) We can globally diminish mobility by adopting a reduced overall diffusion rate $d' < 1$; and/or ii) we can drastically reduce the probability of utilizing a long-distance connection to $d_\phi \ll 1$. We have found that the latter mitigation strategy of curtailing the infection short-cuts into distant regions has a far superior effect. Therefore, in
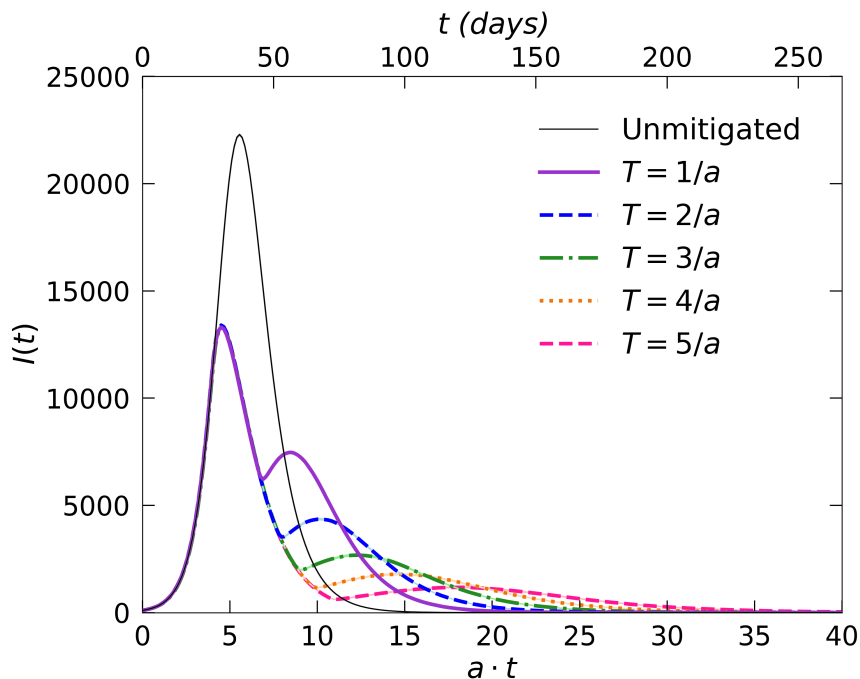
Figure 4.3: Infection curves $I(t)$ from stochastic SIR model simulations on a two-dimensional Newman-Watts small-world network. The graphs compare outbreak data without mitigation (grey) and for varying social-distancing intervention duration T (as indicated), during which the probability of moving through long-distance connections was drastically reduced to $d_\phi = 0.05$. (The data for each curve were averaged over 100 independent realizations.)

Figure 4.3 we display the resulting data for such a scenario where we set $d_\phi = 0.05$, yet kept the diffusion rate unaltered at d=1; as before, this control was triggered once $I(t) = 0.1N$ had been reached in the course of the epidemic. The resurgence peak height and growth rate become even more stringently reduced with extended mitigation duration than for (distinct) social distancing measures implemented on the regular lattice.

4.2.3   Random and scale-free contact networks

Finally, we run the stochastic SIR dynamics on two different static structures, namely i) randomly connected and ii) scale-free contact networks. Each network link may be in either the S, I, or R configurations, which are subject to the SIR reaction rules, but we do not
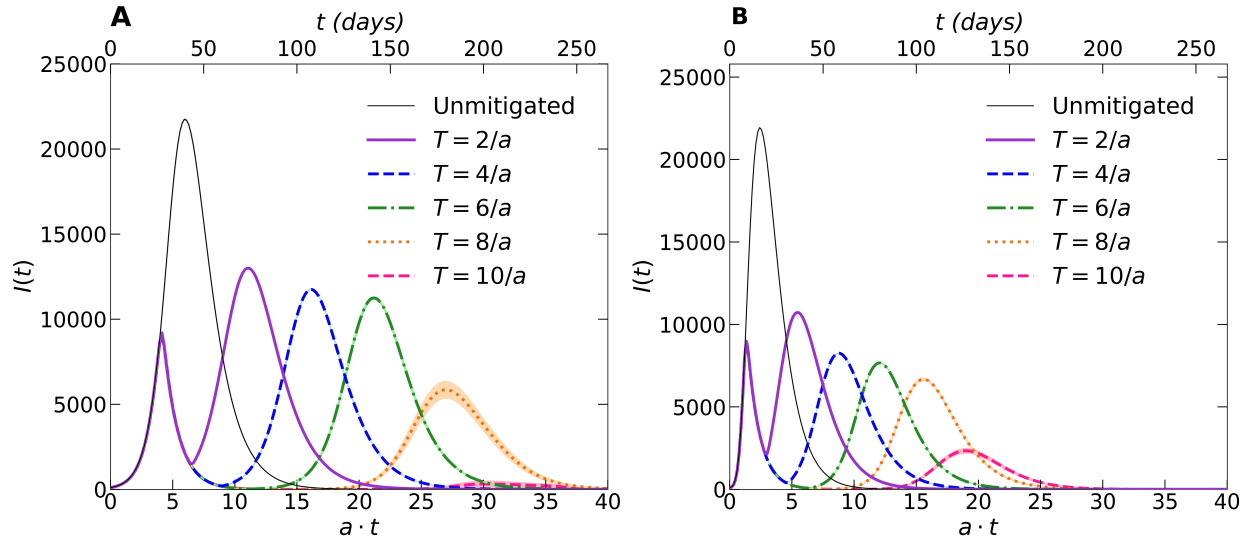
Figure 4.4: Infection outbreak curves $I(t)$ from stochastic SIR model simulations. (A) On a randomly connected network; (B) on a scale-free network with varying social-distancing intervention duration T. (The data for each curve were averaged over 100 independent realizations.)

allow movement among the network vertices. For the random network, we uniformly distribute 1,000,000 edges among $N = 100,000$ nodes; this yields a Poisson distribution for the connectivity with preset mean (equal to the variance) $\langle k \rangle = (\Delta k)^2 = 20$. For the scale-free network, we employ the Barabasi-Albert graph construction [111], where each new node is added successively with $k = 4$ edges, to yield a total of 799,980 edges. The connectivity properties in these quite distinct architectures are vastly different, since the scale-free networks feature prominent 'hubs' through which many other nodes are linked. In the epidemic context, these hubs represent super-spreader centers through which a large fraction of the population may become infected [48, 112].

To implement the stochastic SIR dynamics on either contact network, we employ the efficient rejection-free Gillespie dynamical Monte Carlo algorithm: Each reaction occurs successively, but the corresponding time duration between subsequent events is computed from the associated probability function [113] (for details, see Section 4.3). The random social network

(a)   (b)
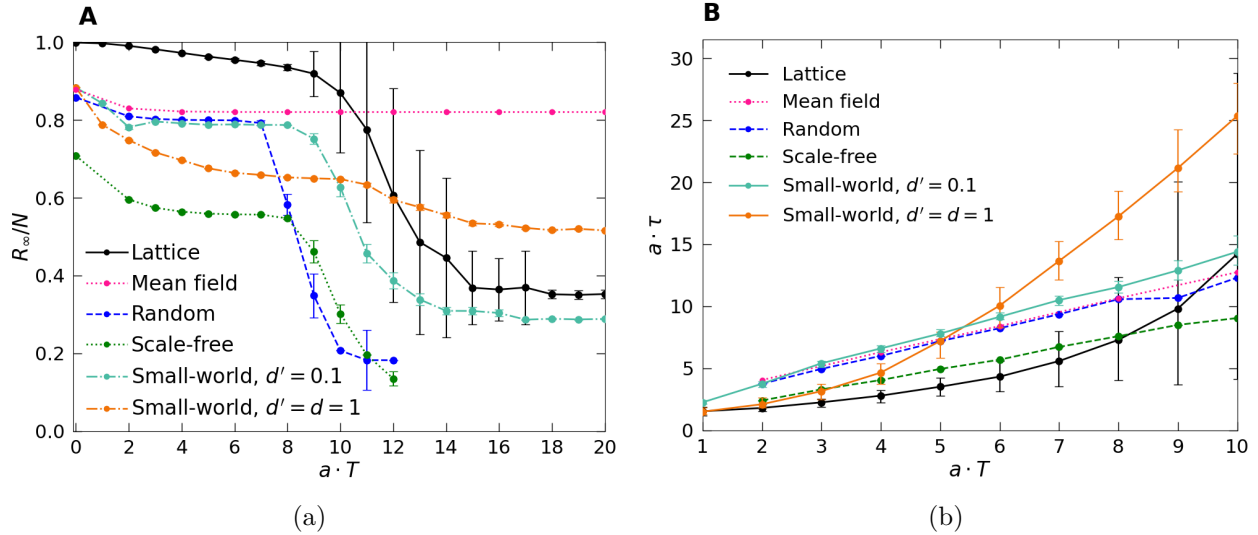
Figure 4.5: Comparison of epidemic control measures through social distancing mitigation as functions of their duration T on the various architectures. (A) Recovered saturation fraction R_∞/N; (B) time τ after release of the control measures until the infection resurgence peak is reached.

may be considered an emulation of the well-connected mean-field model. Indeed, we obtain excellent agreement for the temporal evolution of the SIR dynamics in these two systems with $a = 0.15$ MCS (for the scale-free network, a small adjustment to an effective mean-field recovery rate $a \approx 0.18$ MCS is required). A variety of measures can be taken to effectively control the epidemic spread on a network [107, 108]. We implement a 'complete lockdown' mitigation strategy: Once the threshold $I(t) = 0.1N$ has been reached, we immediately cut all links for a subsequent duration T; during that time interval, only spontaneous recovery $I \to R$ can occur.

In Figure 4.4, we discern a markedly stronger impact of this lockdown on the intensity of the epidemic resurgence in both these static contact network architectures, see also Figure 4.5(a) above. On the other hand, the mitigation duration influences the second infection wave less strongly, with the time until its peak has been reached growing only linearly with T: $\tau(T) \sim T$, as is visible in Figure 4.5(b). There is however a sharp descent in resurgent peak
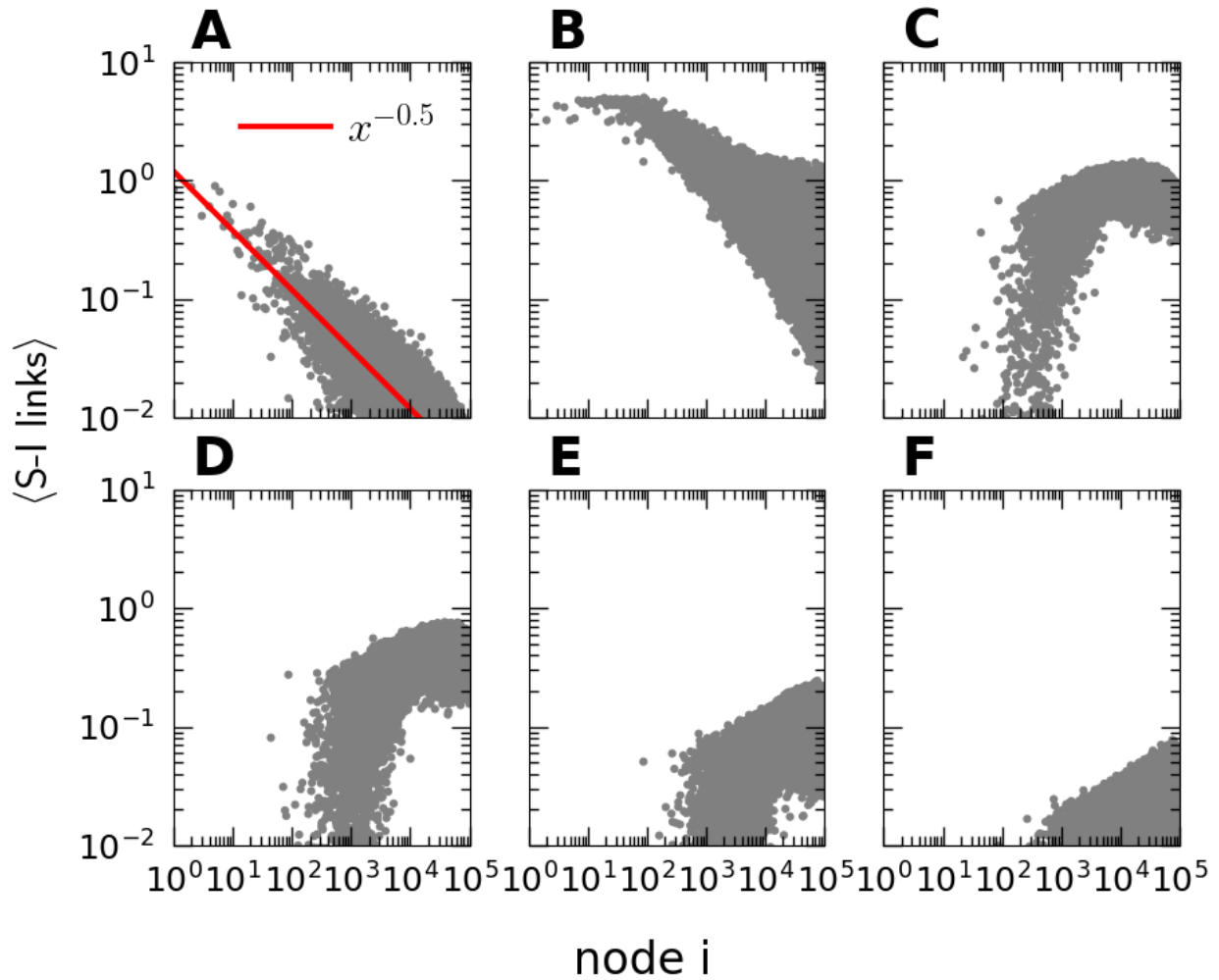
Figure 4.6: Distribution of the mean number of susceptible-infectious (SI) connections for the nodes in scale-free contact networks. (A) Network configuration before and (B-F) while the epidemic surge is spreading through the system. (A) at $t = 0$; (B) after 5 days; (C) after 10 days; (D) after 20 days, when the epidemic has reached its (unmitigated) peak; (E) after 30 days; (F) after 40 days, when only about 100 infectious individuals are left. (The data for each curve were averaged over 10,000 independent simulation runs.)

height beyond an apparent threshold $T > 7/a$ for the random network, and $T > 8/a$ for the scale-free network. For both the two-dimensional regular lattice and small-world structure, a similar sudden drop in the total number of infected individuals (Figure 4.5(b)) requires a considerably longer mitigation duration: In these dynamical networks, the repopulation of nodes with infective individuals facilitates disease spreading, thereby diminishing control efficacy.

We remark that if a drastically reduced diffusivity $d' \ll 1$ is implemented, the small-world results closely resemble those for a randomly connected contact network (Figure 4.5(a)).

Moreover, we have observed an unexpected and drastic effective structural change in the scale-free network topology as a consequence of the epidemic outbreak infecting its susceptible nodes. Naturally, the highly connected hubs are quickly affected, and through transitioning to the recovered state, become neutralized in further spreading the disease. As shown in Figure 4.6, as the infection sweeps through the network (in the absence of any lockdown mitigation), the distribution of the remaining active susceptible-infectious (SI) links remarkably changes from the initial scale-free power law with exponent -1/2 to a more uniform, almost randomized network structure. The disease resurgence wave thus encounters a very different network topology than the original outbreak.

4.3   Supplementary Materials

4.3.1   Square lattices with diffusive spreading

On our regular square lattice with L^2 sites set on a two-dimensional torus, we implement the stochastic Susceptible-Infectious-Recovered (SIR) epidemic model with the following individual-based Monte Carlo algorithm:

1. Randomly distribute N individuals on the lattice, subject to the restriction that each site may only contain at most one individual, and with period boundary conditions. Some small fraction of the individuals will initially be infectious, while the remainder of the population will be susceptible to the infection.

2. Perform random sequential updates L^2 times in one Monte Carlo step (MCS) by picking a lattice site at random, and then performing the following actions:

   a If the selected site contains a susceptible S or a recovered individual R, a hopping direction is picked randomly. If the adjacent lattice site in the hopping direction is empty, then the chosen individual is moved to that neighboring site with hopping probability d that is related to a macroscopic diffusion rate.

   b If the chosen lattice site contains an infectious individual I, it will first try to infect each susceptible nearest neighbor S with a prescribed infection probability r. If this attempt is successful, the involved susceptible neighbor S immediately changes its state to infected I. After the originally selected infected individual has repeated its infection attempts with all neighboring susceptibles S, it may reach the immune state R with recovery probability a. Finally, this particular individual, whether still infectious or recovered, tries to hop in a randomly picked direction with probability d, provided the chosen adjacent lattice site is empty.

3. Repeat the procedures in item 2 for a preselected total number of Monte Carlo steps.

To determine the effective (coarse-grained) basic epidemic reproduction ratio R_0, we fit the infection curves to straightforward numerical integrations of the deterministic SIR rate equations $dS(t)/dt = -rS(t)I(t)/N$, $dI(t)/dt = rS(t)I(t)/N - aI(t)$, $dR(t)/dt = aI(t)$, and adjust the lattice simulation infection probability $r \approx 1.0$ and to a lesser extent, the recovery probability a to finally match the targeted COVID-19 value $R_0 \approx 2.4$. We note that this
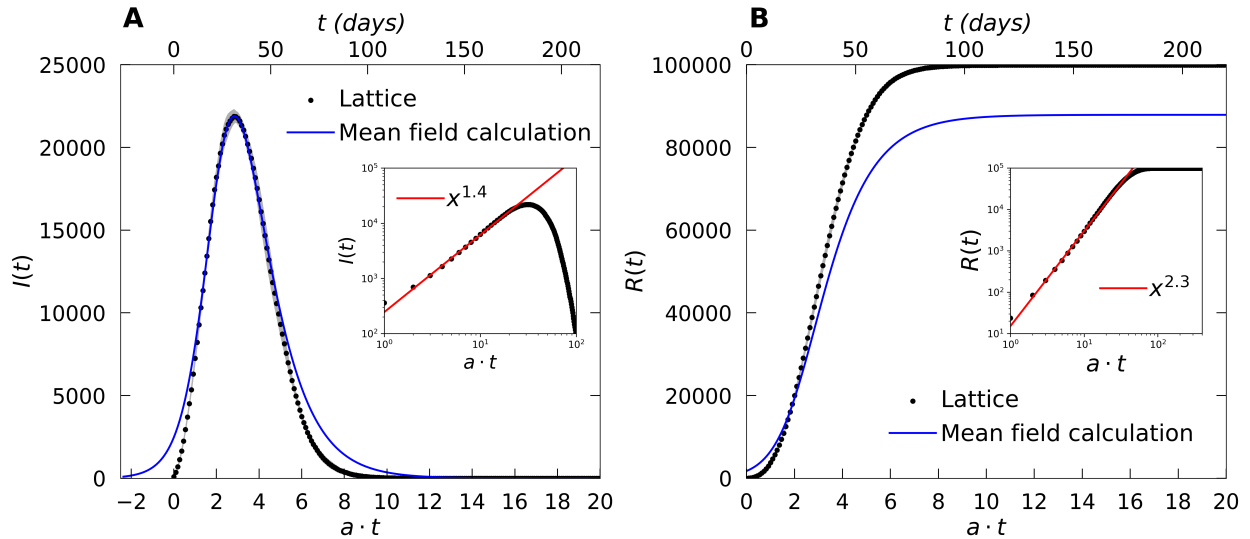
Figure 4.7: Fit of infection curves from lattice simulations to the numerically integrated curves from the mean-field SIR rate equations. (A) Infectious population $I(t)$; (B) recovered number of individuals $R(t)$. The insets illustrate the power law initial growth $I(t) \sim t^{1.4 \pm 0.1}$ and $R(t) \sim t^{2.3 \pm 0.1}$ for the lattice simulation data (averaged over 100 independent realizations).

slightly 'renormalized' value for a is subsequently utilized to set the time axis scale in the figures. On the mean-field level, initially $R_0 = (r/a)S(0)/N$, since all nodes are mutually connected. In spatial settings, $S(0)/N$ is to be replaced with the mean connectivity (i.e., the coordination number for a regular lattice) to susceptible individuals. The lattice simulation data is fitted with the mean-field result by matching two parameters: the maximum value and the half-peak width of the infectious population curve $I(t)$, see Figure 4.7. The lattice simulation curve digresses from the mean-field curves at low $I(t)$ values, far away from the peak region. In the lattice simulations, the initial rise of the infectious population curve exhibits power-law growths $I(t) \sim t^{1.4 \pm 0.1}$ and $R(t) \sim t^{2.3 \pm 0.1}$ in clear contrast with the simple exponential rise of the mean-field SIR curve as obtained from integrating the mean-field rate equations. We note that these are the standard critical exponents θ and $1 + \theta$ for the temporal growth of an active seed cluster near a continuous non-equilibrium phase transition to an absorbing extinction state [24].
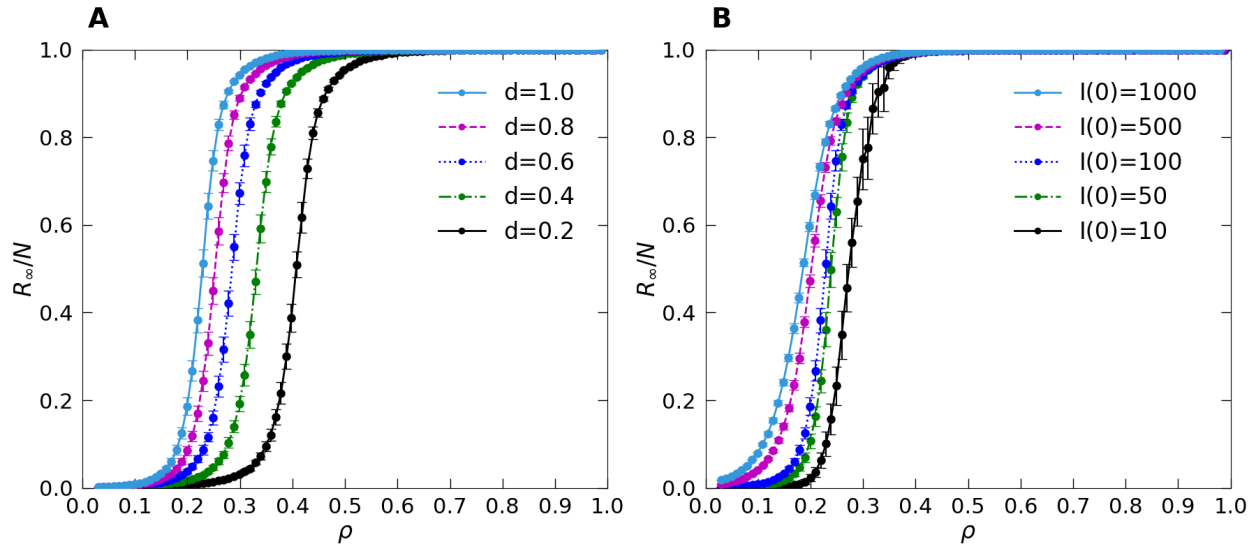
Figure 4.8: Variation of the total fraction of recovered individuals R_∞/N with the lattice simulation parameters in stochastic SIR model simulations on a square lattice on the total density ρ. (A) Data for different sets of nearest-neighbor hopping rates d; (B) for varying numbers of initially infected individuals $I(0)$. The graphs demonstrate the presence of a percolation-like epidemic threshold. (Each data point was averaged over 100 independent simulation runs.)

Figure 4.8 shows the dependence of the asymptotic number of recovered individuals R_∞ on the density ρ for various sets of hopping rates d and initial infectious population values $I(0)$. These data indicate the existence of a well-defined epidemic threshold, i.e., a percolation-like sharp transition from a state when only a tiny fraction of individuals is infected, to the epidemic state wherein the infection spreads over the entire population [45]. As one would expect, this critical point depends only on the ratio a/d of the recovery and hopping rates. Varying the lattice simulation parameters just shifts the location of the epidemic threshold. Once the model parameters are set in the epidemic spreading regime, the system's qualitative behavior is thus generic and robust, and only weakly depends on precise parameter settings.
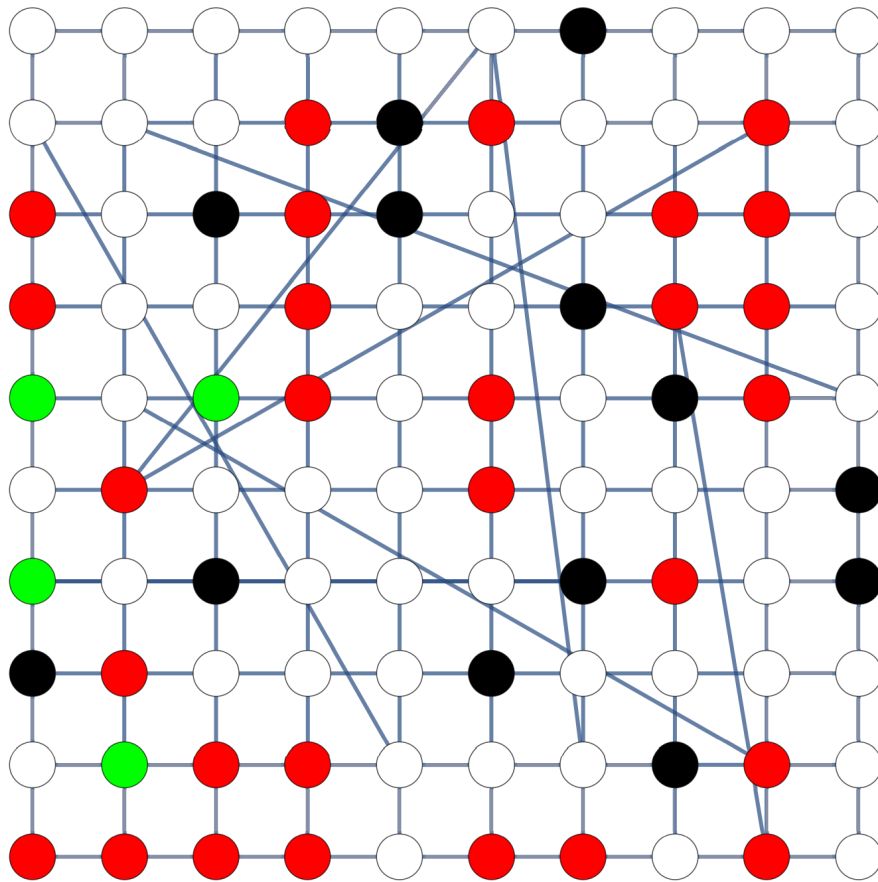
Figure 4.9: Schematic construction of a two-dimensional Newman-Watts small-world network. It is obtained from a regular square lattice through adding long-distance connections; shown is an SIR model configuration snapshot with empty (white), susceptible (green), infectious (red), and recovered (black) states.

4.3.2   Two-dimensional small-world networks

For our two-dimensional small-world network, whose construction is schematically depicted in Figure 4.9, we employ a similar Monte Carlo algorithm as described above; the essential difference is that individuals may now move to adjacent nearest-neighbor as well as to distant lattice sites along the pre-set 'short-cut' links. Figure 4.10 demonstrates (for fixed diffusivity $d = 1$) that as function of the fraction ϕ of long-distance links in a two-dimensional small-world network, the epidemic threshold resides quite close to zero: The presence of a mere few 'short-cuts' in the lattice already implies a substantial population mixing. The inset, where the ϕ axis is scaled logarithmically, indicates that sizeable outbreaks begin for $\phi \geq 0.05$. Figure 4.10 similarly shows the outbreak dependence on the diffusion rate d (here for $\phi = 0.6$), with the threshold for epidemic spreading observed at $d \approx 0.3$. Evidently, prevention of disease outbreaks in this architecture requires that both mobility and the presence of far-ranging connections be stringently curtailed.

4.3.3   Random and scale-free contact networks

For both the randomly connected and scale-free contact networks, we employ the Gillespie or dynamical Monte Carlo algorithm, which allows for efficient numerical simulations of Markovian stochastic processes. It consists of these subsequent steps:

1. Initially, few nodes are assigned to be infected I, while all other nodes are set in the susceptible state S. Each susceptible node S is characterized by a certain number of active links that are connected to infected nodes I.

2. We then determine the rate at which each infected node I will recover, and at which each susceptible node S with a non-zero number of active links becomes infected. From
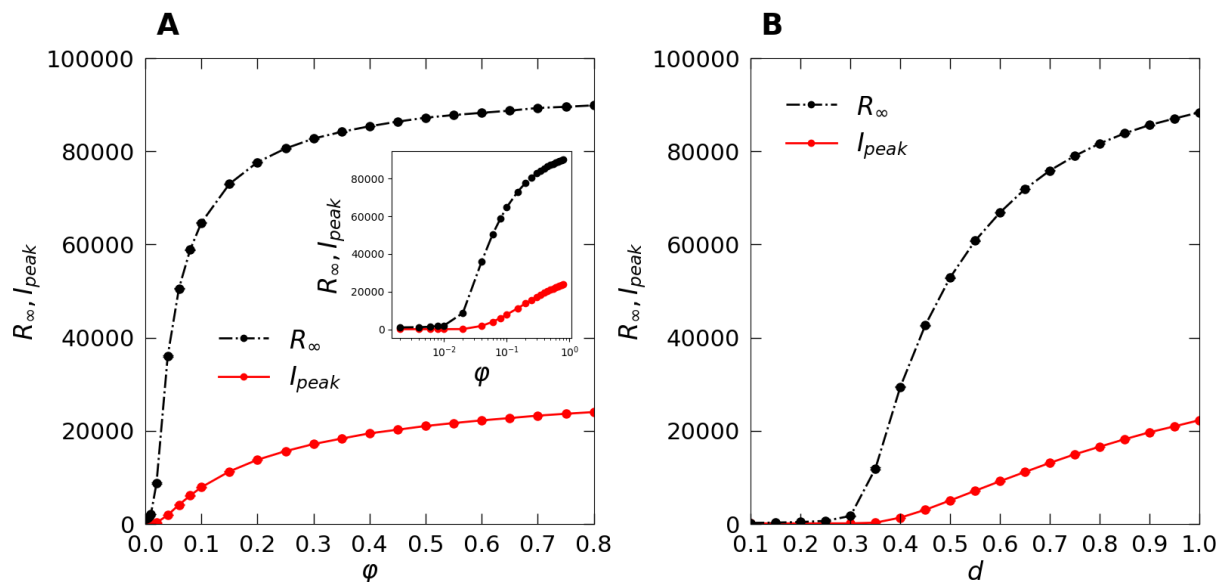
Figure 4.10: Epidemic peak value and total recovered fraction R_∞ and peak intensity I_{peak}. (A) As functions of the fraction ϕ of long-distance links with fixed $d = 1$ (inset: same data, with the ϕ axis on a logarithmic scale); (B) as functions of the diffusivity d with fixed $\phi = 0.6$ for the SIR model implemented on a two-dimensional Newman-Watts small-world network. (Each data point was averaged over 100 independent realizations.)

these we infer the total event rate r_{tot}.

3. Based on this total rate r_{tot}, we select the waiting time until the next event occurs from an exponential distribution with mean r_{tot}.

4. We then select any permissible event with a probability proportional to its rate, update the status of each node, and repeat these processes for the desired total number of iterations.

4.4   Conclusion and Discussion

In this study, we implemented social distancing control measures for simple stochastic SIR epidemic models on regular square lattices with diffusive spreading, two-dimensional

Newman-Watts small-world networks that include highly infective long-distance connections, and static contact networks, either with random connectivity or scale-free topology. In these distinct architectures, all disease spreading mitigation measures, be that through reduced mobility and/or curtailed connectivity, must of course be implemented at an early outbreak stage, but also maintained for a sufficient duration to be effective. In Figure 4.5, we compare salient features of the inevitable epidemic resurgence subsequent to the elimination of social distancing restrictions, namely the asymptotic fraction R_∞/N of recovered individuals, i.e., the integrated number of infected individuals; and the time $\tau(T)$ that elapses between the release and the peak of the second infection wave, both as function of the mitigation duration T. We find that the latter grows exponentially with T on both dynamical lattice architectures, but only linearly on the static networks (Figure 4.5(b)). Furthermore, as one would expect, the mean-field rate equations pertaining to a fully connected system describe the randomly connected network very well.

In stark contrast to the mean-field results (indicated by the purple lines in Figure 4.5), the data for the lattice and network architectures reveal marked correlation effects that emerge at sufficiently long mitigation durations T. For $T > 8/a$ in the static networks, and $T > 12/a$ in the lattice structures, the count of remaining infectious individuals I becomes quite low; importantly, these are also concentrated in the vicinity of a few persisting infection centers. This leads to a steep drop in R_∞/N, the total fraction of ever infected individuals, by a factor of about 4 in the static network, and 3 in the dynamic lattice architectures. Thus, in these instances, follow-up disease control measures driven by high-fidelity testing and efficient contact tracking should be capable of effectively eradicating the few isolated disease resurgence centers. However, to reach these favorable configurations for the implementation of localized and targeted epidemic control, it is imperative to maintain the original social-distancing restrictions for at least a factor of three (better four) longer than it would have

taken the unmitigated outbreak to reach its peak ($T \approx 3/a...6/a$ in our simulations) – for COVID-19 that would correspond to about two months. As is evident from our results for two-dimensional small-world networks that perhaps best represent human interactions, it is also absolutely crucial to severely limit all far-ranging links between groups to less than 5% of the overall connections, during the disease outbreak.

Following this work, we have further looked at the effects of introducing the incubation period to the modeling of the epidemics spread [114]. Our simulations of an extended Susceptible-Exposed-Infectious-Recovered (SEIR) compartmental model have shown that the incubation period sets a delay to the infection onset and induces a broadening of the infection curves in comparison to the SIR model.

Chapter 5

Conclusions

In this thesis we have explored the possibility of controlling the dynamics of certain lattice-based non-equilibrium systems through variations of the systems' control parameters.

In Chapter 2, we have studied the two-temperature two-dimensional Katz-Lebowitz-Spohn driven lattice gas, where the geometry of the lattice was arranged such that the temperature boundaries are oriented perpendicular to the external particle drive that is responsible for a completely biased diffusion. We ran simulations on this system, maintaining the hotter temperature region at $T > T_c$ and the cooler temperature region exactly at T_c, where T_c is the KLS critical temperature for the second-order phase transition. We calculated the two-time autocorrelation function in the hotter and colder regions of the lattice, and compared the values of the aging scaling exponents with the TASEP and critical KLS aging exponents to learn more about the type of collective behavior in this spatially inhomogeneous hybrid system.

We found that the original collective behavior that governs the dynamics of the KLS model at $T > T_c$ or at T_c is destroyed in both subsystems when they start to notice the effect of the coupling. As we have shown in the Section 2.3, in the hotter region with temperature $T > T_c$, the system evolves as if there are no attractive interactions between the particles, and experiences particle blockage in front of the temperature boundary from the hotter region held at $T > T_c$ to the critical region held at T_c. This accumulation of particles at the temperature boundary is induced by the extended particle clusters in the critical

91

region. Remarkably, we observe the density profiles ($\rho(x)$ vs x plots) in both high-and low-temperature subsystems to be similar to the density profiles found for the well-characterized (T)ASEP models with open boundary conditions, namely in the coexistence and maximal-current phases, which are respectively governed by hyperbolic and trigonometric tangent functions. Yet if the lower temperature is set to T_c, we detect marked corrections to the hyperbolic and trigonometric tangent-like density profiles due to fluctuations, e.g., we observe the algebraic power-law decay of the density near the interfaces into the cooler region with the critical KLS exponent.

In Chapter 3, we have explored the other choice of the geometry for the two-temperature two-dimensional Katz-Lebowitz-Spohn driven lattice gas, where the temperature boundaries are oriented parallel to the drive. We have demonstrated for the symmetry-preserving particle hopping rates across the temperature interfaces that in a certain range of temperatures the two subsystems can become effectively decoupled. In that situation, the original collective dynamics in the hotter and critical subsystems seems to be preserved and governed by the (T)ASEP and critical KLS scaling exponents, respectively. On the other hand, the particle density fluctuations scale according to the (T)ASEP when both temperatures are set well above the critical temperature.

After measuring the particle current in the system for the particle-hole symmetric hopping rates at the interfaces, we found that the particle current difference across them generates a current vector flow diagram akin to an infinite flat vortex sheet. The "strength" of the vortex sheet is controlled by the subsystems' temperatures. If the colder subsystem is maintained at the KLS critical temperature $T_{cold} = T_c$, while the hotter subsystem's temperature is set much higher at $T_{hot} \gg T_c$, the particle currents at the interface greatly inhibit any particle exchange between the two temperature regions. The ensuing effective subsystem separation allows strong fluctuations to persist in the critical region, resulting in the scaling of the

particle density fluctuations with the KLS critical exponents. However, if both temperatures are set well above the critical temperature, the particle density fluctuations scale with scaling exponents that belong to the (T)ASEP universality class. We have also measured the rate of the entropy production in both subsystems; it displays intriguing algebraic decay in the critical region, while it reaches quickly a small but non-zero value in the hotter region.

We plan to explore the possibility of controlling the critical KLS scaling behavior in various two-temperature hybrid KLS models in greater detail in future studies. In particular, we are interested in varying the subsystems' lateral aspect ratio, perpendicular to the external drive, and intend to investigate to what extent one could shrink either of the temperature regions while preserving their scale-invariant dynamics.

After considering both the transverse and the parallel alignment variants for the interfaces in the two-temperature KLS driven lattice gas, it is natural to ask which of these systems' distinct physical behaviors will prevail in an intermediate case, when the temperature boundaries are tilted relative to the external drive, but not orthogonal to it. For such "diagonal" temperature interfaces, we expect to observe similar density phase separation as for the case of fully transverse subsystem boundaries; yet, in addition, we would also anticipate seeing vortex current sheets located right at the temperature interfaces. A detailed study is required to answer questions such as whether the phase separation interface would be localized at the center of the hot subsystem, and whether this generalized diagonal two-temperature KLS variant still possesses dynamical scaling properties when the cooler subsystem is held at the critical temperature.

In Chapter 4, we have investigated the effectiveness of non-pharmaceutical control measures against the COVID-19 pandemic by simulating its spreading with the stochastic SIR model on various spatial architectures. In our effort to control the spread of the disease, we found that the intensity and spatial extent of the epidemic second wave can be substantially di-

minished if the restrictions are delayed sufficiently (for a duration of at least thrice the time until the peak of the unmitigated outbreak). Remarkably, we find that the time $\tau(T)$ that elapses between the release of restrictions and the peak of the second infection wave grows exponentially with T on both dynamical lattice architectures, but only linearly on the static networks. Furthermore, as one would expect, both the mean-field rate equations (pertaining to a fully connected system) and the randomly connected network produce very similar predictions.

Requiring stringent non-pharmaceutical measures from a community, such as a complete lockdown, may not be necessary if an effective contact tracing and isolation strategy is adopted at the early stages of the infection spread. In order to develop such a strategy, we are currently employing individual-based Monte Carlo computer simulations of a stochastic Susceptible-Exposed-Infectious-Recovered (SEIR) model variant on a two-dimensional Newman–Watts small-world network to investigate the control of epidemic outbreaks through periodic testing and isolation of infectious individuals, and subsequent quarantine of their immediate contacts. Using disease parameters informed by the COVID-19 pandemic, we investigate the effects of various crucial mitigation features on the epidemic spreading: fraction of the infectious population that is identifiable through the tests; testing frequency; time delay between testing and isolation of positively tested individuals; and the further time delay until quarantining their contacts as well as the quarantine duration. We thus hope to determine the required ranges for these intervention parameters to yield effective control of the disease through both considerably delaying the epidemic peak and massively reducing the total number of sustained infections.

Bibliography

1. Schnakenberg, J. Network theory of microscopic and macroscopic behavior of master equation systems. *Rev. Mod. Phys.* **48,** 571–585 (1976).

2. Zia, R. K. P. & Schmittmann, B. A possible classification of nonequilibrium steady states. *Journal of Physics A: Mathematical and General* **39,** L407–L413 (2006).

3. Zia, R. K. P. & Schmittmann, B. Probability currents as principal characteristics in the statistical mechanics of non-equilibrium steady states. *Journal of Statistical Mechanics: Theory and Experiment* **2007,** P07012–P07012 (2007).

4. Chandrasekhar, S. Stochastic Problems in Physics and Astronomy. *Rev. Mod. Phys.* **15,** 1–89 (1943).

5. McQuarrie, D. A. Stochastic approach to chemical kinetics. *Journal of Applied Probability* **4,** 413–478 (1967).

6. Van Kampen, N. *Stochastic Processes in Physics and Chemistry* (Elsevier Science, 2011).

7. Krapivsky, P., Redner, S. & Ben-Naim, E. *A Kinetic View of Statistical Physics* (Cambridge University Press, 2010).

8. Glauber, R. J. Time-Dependent Statistics of the Ising Model. *Journal of Mathematical Physics* **4,** 294–307 (1963).

9. Derrida, B., Domany, E. & Mukamel, D. An Exact Solution of a One-Dimensional Asymmetric Exclusion Model with Open Boundaries. *J. Stat. Phys.* **69,** 667–687 (1992).

10. Derrida, B., Evans, M. R., Hakim, V. & Pasquier, V. Exact solution of a 1D asymmetric exclusion model using a matrix formulation. *J. Phys. A: Math. Gen.* **26,** 1493 (1993).

11. Barkai, E. Fractional Fokker-Planck equation, solution, and application. *Phys. Rev. E* **63,** 046118 (2001).

12. Reif, F. *Fundamentals of Statistical and Thermal Physics* (McGraw-Hill, 1965).

13. Hohenberg, P. C. & Halperin, B. I. Theory of dynamic critical phenomena. *Rev. Mod. Phys.* **49,** 435–479 (1977).

14. Kardar, M. *Statistical Physics of Fields* (Cambridge University Press, 2007).

15. Landau, L. D. On the theory of phase transitions. *Zh. Eksp. Teor. Fiz.* **7,** 19–32 (1937).

16. Kawasaki, K. Simple derivations of generalized linear and nonlinear Langevin equations. *Journal of Physics A: Mathematical, Nuclear and General* **6,** 1289–1295 (1973).

17. Yang, Y., McDermott, D., Reichhardt, C. J. O. & Reichhardt, C. Dynamic phases, clustering, and chain formation for driven disk systems in the presence of quenched disorder. *Phys. Rev. E* **95,** 042902 (2017).

18. Zinn-Justin, J. *Quantum Field Theory and Critical Phenomena* (Clarendon Press, 2002).

19. Feigenbaum, M. J. Universal behavior in nonlinear systems. *Physica D: Nonlinear Phenomena* **7,** 16–39 (1983).

20. Patashinskii, A. Z., Pokrovskii, V. L. & Shepherd, P. J. *Fluctuation theory of phase transitions : covering second-order phase transitions, scale and conformal invariance, algebras of fluctuating quantities, degenerate systems, critical dynamics, epsilon expansions, renormalization group, and applications / by A. Z. Patashinskii and V. L. Pokrovskii ; translated and edited by P. J. Shepherd* (Pergamon Press Oxford ; New York, 1979).

21. Grinstein, G. Generic scale invariance in classical nonequilibrium systems (invited). *J. Appl. Phys.* **69,** 5441 (1991).

22. Lemons, D. S. & Gythiel, A. Paul Langevin's 1908 paper "On the Theory of Brownian Motion" ["Sur la théorie du mouvement brownien," C. R. Acad. Sci. (Paris) 146, 530–533 (1908)]. *American Journal of Physics* **65,** 1079–1081 (1997).

23. Chaikin, P. M. & Lubensky, T. C. *Principles of Condensed Matter Physics* (Cambridge University Press, 1995).

24. Täuber, U. C. *Critical Dynamics: A Field Theory Approach to Equilibrium and Non-Equilibrium Scaling Behavior* (Cambridge University Press, 2014).

25. Landau, D. P. & Binder, K. *A Guide to Monte Carlo Simulations in Statistical Physics* 4th ed. (Cambridge University Press, 2014).

26. Newman, M., Barkema, G. & Barkema, I. *Monte Carlo Methods in Statistical Physics* (Clarendon Press, 1999).

27. Marro, J. & Dickman, R. *Nonequilibrium Phase Transitions in Lattice Models* (Cambridge University Press, 1999).

28. Ódor, G. *Universality in Nonequilibrium Lattice Systems* (World Scientific, 2008).

29. Henkel, M., Hinrichsen, H. & Lübeck, S. *Non-Equilibrium Phase Transitions: Volume 1: Absorbing Phase Transitions* (Springer Netherlands, 2008).

30. Péter, H., Libál, A., Reichhardt, C. & Reichhardt, C. J. O. Crossover from Jamming to Clogging Behaviours in Heterogeneous Environments. *Scientific Reports* **8** (2018).

31. Bae, M.-H. *et al.* Ballistic to diffusive crossover of heat flow in graphene ribbons. *Nature communications* **4,** 1734 (2013).

32.   Azizi, A. & Pleimling, M. Critical phenomena in the presence of symmetric absorbing states: A microscopic spin model with tunable parameters. *Phys. Rev. E* **102,** 022112 (2020).

33.   Mukhamadiarov, R. I., Priyanka & Täuber, U. C. Transverse temperature interfaces in Katz-Lebowitz-Spohn driven lattice gas. *Phys. Rev. E* **100,** 062122 (2019).

34.   Mukhamadiarov, R. I. & Täuber, U. C. Parallel temperature interfaces in the Katz–Lebowitz–Spohn driven lattice gas. *Journal of Statistical Mechanics: Theory and Experiment* **2020,** 113207 (2020).

35.   Spitzer, F. Interaction of Markov processes. *Adv. Math.* **5,** 246–290 (1970).

36.   Liggett, T. M. *Interacting Particle Systems* (Springer-Verlag Berlin Heidelberg, 1985).

37.   Chou, T., Mallick, K. & Zia, R. K. P. Non-equilibrium statistical mechanics: from a paradigmatic model to biological transport. *Reports on Progress in Physics* **74,** 116601 (2011).

38.   Schütz, G. & Domany, E. Phase Transitions in an Exactly Soluble One-Dimensional Exclusion Process. *J. Stat. Phys.* **72,** 277–296 (1993).

39.   Derrida, B. An exactly soluble non-equilibrium system: The asymmetric simple exclusion process. *Phys. Rep.* **301,** 65 (1998).

40.   Katz, S., Lebowitz, J. L. & Spohn, H. Phase transitions in stationary nonequilibrium states of model lattice systems. *Phys. Rev. B* **28,** 1655–1658 (1983).

41.   Katz, S., Lebowitz, J. L. & Spohn, H. Nonequilibrium steady states of stochastic lattice gas models of fast ionic conductors. *J. Stat. Phys.* **34,** 497–537 (1984).

42.   Schmittmann, B. & Zia, R. K. P. *Statistical Mechanics of Driven Diffusive Systems* (eds Domb, C. & Lebowitz, J. L.) (Academic Press, 1995).

43. Daquila, G. L. & Täuber, U. C. Nonequilibrium Relaxation and Critical Aging for Driven Ising Lattice Gases. *Phys. Rev. Lett.* **108,** 110602 (2012).

44. Mukhamadiarov, R. I. *et al.* Social distancing and epidemic resurgence in agent-based susceptible-infectious-recovered models. *Scientific Reports* **11,** 130 (2021).

45. Kermack, W. O., McKendrick, A. G. & Walker, G. T. A contribution to the mathematical theory of epidemics. *Proceedings of the Royal Society of London. Series A, Containing Papers of a Mathematical and Physical Character* **115,** 700–721 (1927).

46. Murray, J. *Mathematical Biology* (Springer Berlin Heidelberg, 2013).

47. Liccardo, A. & Fierro, A. A Lattice Model for Influenza Spreading. *PLOS ONE* **8,** 1–11 (2013).

48. Keeling, M. J. & Eames, K. T. Networks and epidemic models. *Journal of The Royal Society Interface* **2,** 295–307 (2005).

49. Hinrichsen, H. Non-equilibrium critical phenomena and phase transitions into absorbing states. *Advances in Physics* **49,** 815–958 (2000).

50. Eubank, S. *et al.* Commentary on Ferguson, et al., "Impact of Non-pharmaceutical Interventions (NPIs) to Reduce COVID-19 Mortality and Healthcare Demand". *Bulletin of Mathematical Biology* **82,** 52 (2020).

51. Lindenberg, K., Metzler, R. & Oshanin, G. *Chemical Kinetics: Beyond The Textbook* (World Scientific Publishing Company, 2019).

52. Schütz, G. in *Phase Transitions and Critical Phenomena Vol. 19* (eds Domb, C. & Lebowitz, J. L.) 1–251 (Academic Press, London, 2001).

53. Schmittmann, B. & Zia, R. K. P. Driven diffusive systems. An introduction and recent developments. *Phys. Rep.* **301,** 45–64 (1998).

54. Hohenberg, P. C. & Cross, M. C. Pattern formation outside of equilibrium. *Rev. Mod. Phys.* **65,** 851–1112 (1993).

55. Täuber, U. C. Phase transitions and scaling in systems far from equilibrium. *Annu. Rev. Condens. Matter Phys.* **8,** 185–210 (2017).

56. Johansson, K. Shape Fluctuations and Random Matrices. *Commun. Math. Phys.* **209,** 437–476 (2000).

57. Stinchcombe, R. Stochastic non-equilibrium systems. *Adv. Phys.* **50,** 431–496 (2001).

58. Schmittmann, B. & Zia, R. K. P. On singularities in the disordered phase of a driven diffusive system. *Z. Phys. B* **97,** 327–332 (1995).

59. Borchers, N., Pleimling, M. & Zia, R. K. P. Nonequilibrium statistical mechanics of a two-temperature Ising ring with conserved dynamics. *Phys. Rev. E* **90,** 062113 (2014).

60. Li, L. & Pleimling, M. Formation of nonequilibrium modulated phases under local energy input. *EPL* **98,** 30004 (2012).

61. Præstgaard, E. L., Schmittmann, B. & Zia, R. K. P. A lattice gas coupled to two thermal reservoirs: Monte Carlo and field theoretic studies. *Eur. Phys. J. B* **18,** 675–695 (2000).

62. Dickman, R. Phase coexistence far from equilibrium. *New J. Phys.* **18,** 043034 (2016).

63. Achahbar, A. & Marro, J. Phase Transitions in a Driven Lattice Gas in Two Planes. *J. Stat. Phys.* **78,** 1493 (1995).

64. Hill, C. C., Schmittmann, B. & Zia, R. K. P. Phase Transitions in Driven Bilayer Systems: A Monte Carlo Study. *Phys. Rev. Lett.* **77,** 514–517 (1996).

65. Aertsens, M. & Naudts, J. Field-induced percolation in a polarized lattice gas. *J. Stat. Phys.* **62,** 609 (1990).

66. Korniss, G., Schmittmann, B. & Zia, R. K. P. Nonequilibrium Phase Transitions in a Simple Three-State Lattice Gas. *J. Stat. Phys.* **86,** 721 (1996).

67. Derrida, B. & Evans, M. R. Exact correlation function in an asymmetric exclusion model with open boundaries. *J. Phys. (Paris) I* **3,** 311–322 (2 1993).

68. Meakin, P., Ramanlal, P., Sander, L. M. & Ball, R. C. Ballistic deposition on surfaces. *Phys. Rev. A* **34,** 5091 (1986).

69. Krug, J. Boundary-induced phase transitions in driven diffusive systems. *Phys. Rev. Lett.* **67,** 1882–1885 (1991).

70. Blythe, R. A. & Evans, M. R. Nonequilibrium steady states of matrix-product form: a solver's guide. *J. Phys. A: Math. Theor.* **40,** R333–R441 (2007).

71. Stinchcombe, R. B. & de Queiroz, S. L. A. Smoothly varying hopping rates in driven flow with exclusion. *Phys. Rev. E* **83,** 061113 (2011).

72. Janowsky, S. A. & Lebowitz, J. L. Exact Results for the Asymmetric Simple Exclusion Process with a Blockage. *J. Stat. Phys.* **77,** 35 (1994).

73. Costin, O., Lebowitz, J. L., Speer, E. R. & Troiani, A. The blockage problem. *Academia Sinica* **8,** 49–72 (2013).

74. Leung, K. & Cardy, J. L. Field theory of critical behavior in a driven diffusive system. *J. Stat. Phys.* **44,** 497–537 (1986).

75. Janssen, H. K. & Schmittmann, B. Field theory of critical behaviour in driven diffusive systems. *Z. Phys. B* **64,** 503 (1986).

76. Amit, D. *Field Theory, the Renormalization Group, and Critical Phenomena* (World Scientific, Singapore, 1984).

77. Kardar, M., Parisi, G. & Zhang, Y. Dynamic Scaling of Growing Interfaces. *Phys. Rev. Lett.* **56,** 889 (1986).

78. Kriecherbauer, T. & Krug, J. A pedestrian's view on interacting particle systems, KPZ universality and random matrices. *J. Phys. A: Math. Theor.* **43,** 403001 (2010).

79. Henkel, M. & Pleimling, M. *Non-Equilibrium Phase Transitions, Volume 2: Ageing and Dynamical Scaling Far From Equilibrium* (Springer, Heidelberg, 2010).

80. Daquila, G. L. & Täuber, U. C. Slow relaxation and aging kinetics for the driven lattice gas. *Phys. Rev. E* **83,** 051107 (2011).

81. Janssen, H. K., Schaub, B. & Schmittmann, B. New universal short-time scaling behaviour of critical relaxation processes. *Z. Phys. B* **73,** 503–514 (1989).

82. Popkov, V. & Schütz, G. Steady-state selection in driven diffusive systems with open boundaries. *Europhys. Lett.* **48,** 257–263 (1999).

83. Janssen, H. K. & Schmittmann, B. Field Theory of Long Time Behaviour in Driven Diffusive Systems. *Z. Phys. B* **63,** 517–520 (1986).

84. Caracciolo, S., Gambassi, A., Hakim, V., Gubinelli, M. & Pelissetto, A. Finite-Size Scaling in the Driven Lattice Gas. *J. Stat. Phys.* **115,** 281–322 (2004).

85. Bassler, K. E. & Schmittmann, B. Renormalization-group study of a hybrid driven diffusive system. *Phys. Rev. E* **49,** 3614–3618 (1994).

86. Del Campo, A. & Sengupta, K. Controlling quantum critical dynamics of isolated systems. *Eur. Phys. J. Spec. Top.* **224,** 189–203 (2015).

87. Karaman, S. & Frazzoli, E. *High-speed flight in an ergodic forest* in *2012 IEEE International Conference on Robotics and Automation* (2012), 2899–2906.

88. Priyanka, Täuber, U. C. & Pleimling, M. Feedback control of surface roughness in a one-dimensional Kardar-Parisi-Zhang growth process. *Phys. Rev. E* **101,** 022101 (2020).

89. Colangeli, M., Giardinà, C., Giberti, C. & Vernia, C. Nonequilibrium two-dimensional Ising model with stationary uphill diffusion. *Phys. Rev. E* **97,** 030103 (2018).

90. Sadhu, T., Shapira, Z. & Mukamel, D. Interface Phase Transition Induced by a Driven Line in Two Dimensions. *Phys. Rev. Lett.* **109,** 130601 (2012).

91. Endres, R. G. Entropy production selects nonequilibrium states in multistable systems. *Scientific Reports* **7,** 14437 (2017).

92. *Vortex Methods* (eds Anderson, C. R. & Greengard, C.) (Springer-Verlag Berlin Heidelberg, 1987).

93. Jiang, D. Q., Qian, M. & Qian, M. P. *Mathematical Theory of Nonequilibrium Steady States* (Springer-Verlag Berlin Heidelberg, 2004).

94. Spohn, H. *Large Scale Dynamics of Interacting Particles* (Springer-Verlag Berlin Heidelberg, 1991).

95. Caballero, F. & Cates, M. E. Stealth Entropy Production in Active Field Theories near Ising Critical Points. *Phys. Rev. Lett.* **124,** 240604 (2020).

96. Brauner, J. M. *et al.* Inferring the effectiveness of government interventions against COVID-19. *Science* (2020).

97. Flaxman, S. *et al.* Estimating the effects of non-pharmaceutical interventions on COVID-19 in Europe. *Nature* **584,** 257–261 (2020).

98. Ferguson, N. M. *et al.* Strategies for mitigating an influenza pandemic. *Nature* **442,** 448–452 (2006).

99. Halloran, M. E. *et al.* Modeling targeted layered containment of an influenza pandemic in the United States. *Proceedings of the National Academy of Sciences* **105,** 4639–4644 (2008).

100. Murray, C. J. Forecasting COVID-19 impact on hospital bed-days, ICU-days, ventilator-days and deaths by US state in the next 4 months. *medRxiv* (2020).

101. Ferguson, N. *et al.* Report 9: Impact of non-pharmaceutical interventions (NPIs) to reduce COVID-19 mortality and healthcare demand (2020).

102. Adiga, A. *et al.* Evaluating the impact of international airline suspensions on the early global spread of COVID-19. *medRxiv* (2020).

103. Brockmann, D. & Helbing, D. The Hidden Geometry of Complex, Network-Driven Contagion Phenomena. *Science* **342,** 1337–1342 (2013).

104. He, X. *et al.* Temporal dynamics in viral shedding and transmissibility of COVID-19. *Nature Medicine* **26,** 672–675 (2020).

105. Wu, K., Darcet, D., Wang, Q. & Sornette, D. Generalized logistic growth modeling of the COVID-19 outbreak: comparing the dynamics in the 29 provinces in China and in the rest of the world. *Nonlinear Dynamics* **101,** 1561–1581 (2020).

106. Maharaj, S. & Kleczkowski, A. Controlling epidemic spread by social distancing: Do it well or not at all. *BMC Public Health* **12,** 679 (2012).

107. Gross, T. & Sayama, H. *Adaptive Networks: Theory, Models and Applications* (Springer Berlin Heidelberg, 2009).

108. Hindes, J., Schwartz, I. B. & Shaw, L. B. Enhancement of large fluctuations to extinction in adaptive networks. *Phys. Rev. E* **97,** 012308 (2018).

109. Newman, M. E. J., Jensen, I. & Ziff, R. M. Percolation and epidemics in a two-dimensional small world. *Phys. Rev. E* **65,** 021904 (2002).

110. Watts, D. J. & Strogatz, S. H. Collective dynamics of 'small-world' networks. *Nature* **393,** 440–442 (1998).

111. Albert, R. & Barabási, A.-L. Topology of Evolving Networks: Local Events and Universality. *Phys. Rev. Lett.* **85,** 5234–5237 (2000).

112. Easley, D. & Kleinberg, J. *Networks, Crowds, and Markets: Reasoning about a Highly Connected World* (Cambridge University Press, 2010).

113. Vestergaard, C. L. & Génois, M. Temporal Gillespie Algorithm: Fast Simulation of Contagion Processes on Time-Varying Networks. *PLOS Computational Biology* **11,** 1–28 (2015).

114. Serrao, S. R. *et al.* Requirements for the containment of COVID-19 disease outbreaks through periodic testing, isolation, and quarantine. *medRxiv* (2020).